Virtual Planar Motion Mechanism Testing of 8:1 Spheroids

Eddie H Ball

Thesis submitted to the faculty of the Virginia Polytechnic Institute and State University
in partial fulfillment of the requirements for the degree of

Master of Science
In
Aerospace and Ocean Engineering

Wayne Neu, Chair
Daniel Stilwell
Craig Woosley

May 4, 2015
Blacksburg Virginia

Keywords: CFD, STARCCM+, Planar Motion Mechanism (PMM), Flow Topology,
Linear Damping Model, Quadratic Damping Model, Cross Flow Separation

Virtual Planar Motion Mechanism Testing of 8:1 Spheroids

Eddie H Ball

ABSTRACT

PMM testing is a method used to identify the added mass and damping coefficients used in the equations of motion of a vehicle by attempting to decouple the forces on a body due to velocity and acceleration as a result of creating "hydrodynamically pure" velocities and accelerations. This makes it possible to use quasi-steady state models with terms independent of both velocity and acceleration. This paper explores the ability of simple damping models (solely a function of velocity) with added mass terms (solely a function of acceleration) to simulate the heave force of an 8:1 ellipsoid undergoing PMM testing. In order to help explain the complexity of the flow during PMM tests, a flow analysis of the 8:1 spheroid is provided, which discusses the flow topology of spheroids at steady angle of attack, validity of quasi-steady models, and some other basic flow features seen in PMM testing.

In this paper, a simple proportionality relationship between a linear and quadratic damping model is revealed. It is also shown that variations in the heave force response during PMM tests are most heavily influenced by viscous effects, especially cross flow separation. Finally, it is shown where these models break down, owing to the increasing nonlinearity of the flow induced by the harsher motions of large amplitude and/or large frequency tests.

Acknowledgements

I have to thank my advisor and committee chair, Dr. Neu, for his continuous insight in my thesis work. I cannot thank him enough for the constant liveliness he brought to many of our discussions.

I also would like to thank my family for their support. While they could not provide the type of help my advisor could, they were an endless source of moral support.

Finally I would like to thank the Naval Oceanographic Office for funding through the Trawl-Resistant Self-Mooring AUV program.

Table of Contents

List of Figures

List of Tables

Notation

Quick notes on notation:

- Non-bold quantities, such as V, represent scalar quantities. Bold quantities, such as **V**, represent vector quantities or matrices.
- Subscripts either represent the frame of reference, or represent the index in summation notation (Appendix B).

$C_f = \frac{\tau_w}{1/2\rho u_0^2}$	Coefficient of friction
$\mathbf{F}$	Force vector applied to rigid body
$\boldsymbol{f}_b$	Specific body force vector
f	Frequency of oscillation
$\mathbf{h}$	Body angular momentum vector
I	Turbulence intensity
K	Torque on body about $\widehat{\boldsymbol{b}}_1$ axis
k	Turbulent kinetic energy
$\mathbf{L}$	Torque vector applied to rigid body
$\boldsymbol{L}$	Characteristic length of body
M	Torque on body about $\widehat{\boldsymbol{b}}_2$ axis
m	Body's mass
N	Torque on body about $\widehat{\boldsymbol{b}}_2$ axis
N	Number of periods
p	Body angular velocity about $\widehat{\boldsymbol{b}}_1$ axis
p	Pressure
$\mathbf{p}$	Body momentum vector
q	Body angular velocity about $\widehat{\boldsymbol{b}}_2$ axis
$\mathbf{R}$	Rotation matrix
$\mathbf{r}$	Body position vector
$\mathbf{r}^{cm}$	Vector from inertial origin O to rigid body's center of mass cm
$\boldsymbol{r}$	Fluid position vector
r	Body angular velocity about $\widehat{\boldsymbol{b}}_3$ axis
S_{ij}	Average fluid stain rate
s_{ij}	Fluid strain rate
T_{ts}	Time shift between prescribed acceleration and force response
T	Period of oscillation
u	Body velocity along $\widehat{\boldsymbol{b}}_1$ axis
u	Streamwise fluid velocity
u_0	Inlet speed or equivalently nominal body speed
$u_* = \sqrt{\tau_w/\rho}$	Friction velocity
V	Volume

$\boldsymbol{V}$	Fluid velocity vector field w.r.t. inertial coordinates
$\boldsymbol{V}_0$	Free stream velocity vector
$\boldsymbol{V}_g$	Grid velocity
$\mathbf{v}$	Body linear velocity vector
v	Body velocity along $\widehat{\boldsymbol{b}}_2$ axis
v	Transverse fluid velocity
w	Body velocity along $\widehat{\boldsymbol{b}}_3$ axis
w	Spanwise fluid velocity
$\mathbf{X}$	Body's position
X	Force on body along $\widehat{\boldsymbol{b}}_1$ axis
x	Streamwise coordinate
Y	Force on body along $\widehat{\boldsymbol{b}}_2$ axis
y	Transverse coordinate
$y^+ = y_n u_*/\nu$	Y plus value.
y_n	Normal distance from surface or normal distance of n^{th} prism layer
Z	Force on body along $\widehat{\boldsymbol{b}}_3$ axis
z	Spanwise coordinate

Greek	
α	Maximum PMM angle of attack
δ	Boundary layer height
k	Turbulent kinetic energy
ℓ_{turb}	Turbulent mixing length
$\boldsymbol{\eta}$	Body's linear and angular velocity vector
ρ	Fluid density
θ	Second Euler angle
ς	Position in arbitrary degree of freedom
$\boldsymbol{\tau}$	deviatoric stress tensor
$\tau_{R,ij}$	Specific Reynolds stress tensor
τ_w	Shear stress at wall
φ_i	Sub functions of the velocity potential (are potentials themselves)
ϕ	Third Euler angle or the velocity potential
ψ	First Euler angle
μ	Dynamic viscosity
ν	Kinematic viscosity
$\boldsymbol{\omega}$	Body's angular velocity vector
ω_T	Specific turbulent dissipation

1. Introduction

1.1 Motivation

Models able to capture all the physics for most real systems are infeasible. Thankfully, only the relevant physics need to be modeled in order to derive useful models, able to predict real world system dynamics. The relevant physics are highly dependent on the system being considered. Dimensional analysis is a method that can be used to help determine which parameters in a system are relevant. For a basic discussion of the fundamentals of dimensional analysis, see [1]. The relevant parameters can then be used to create models. These models, while simplifications of the full system dynamics, are still often very complex.

The kinematic and dynamics of an autonomous underwater vehicle (AUV) are generally described by a coupled set of nonlinear partial differential equations (PDE's) which do not have analytic solutions. The equations of motion (EOM) of the vehicle used in this paper are derived from potential flow with an assumed damping matrix added. The damping matrix was assumed to take one of three forms: a linear model, a quadratic model, or a combined linear quadratic model. These damping models are major simplifications. They combine all shear and pressure forces on the body created by a very complex flow into simple polynomials of the state of the body. Through the use of computational fluid dynamic (CFD) simulations, it is demonstrated at what conditions severe nonlinearities occur in Planar Motion Mechanism (PMM) tests and which model (not considering the combined linear/quadratic model) is best able to account for these nonlinearities. With this analysis recommendations on how to perform PMM tests are given for the linear model, which is shown to be a better damping model than the quadratic model. The flow topology of spheroids at large angle of attack are also discussed to shed light on the finer details of the flow during severe maneuvers. These results are used to help theorize how cross flow separation drives the nonlinearity of the heave force responses of spheroids undergoing PMM tests. Finally, the validity of quasi-steady state models is briefly discussed.

1.2 Literature Review

PMM tests, described in §1.9, began in the late 1950's with the David Taylor Model Basin (DTMB) PMM system to determine various hydrodynamic coefficients (added mass and damping) used to populate models for vehicles [2]. Before PMM tests, straight line towing tanks were used to determine linear hydrodynamic coefficients. However separate facilities, such as rotating arm facilities, were needed to determine rotary hydrodynamic coefficients. PMM facilities succeeded in allowing experimentalists to determine both linear and rotary hydrodynamic coefficients in one test and one degree of freedom (DOF).

As pointed out by Bishop in [3], there is little doubt to the practicality of PMM testing in determining the correct hydrodynamic coefficients. However Bishop brings up important theoretical distinctions separating the hydrodynamic coefficients into three

types: true derivatives, slow motion derivatives, and oscillatory coefficients[1]. The point he made was that there is currently no known method for calculating the true hydrodynamic derivatives because it is unclear how to start from steady state and impart a perturbation in only one variable (i.e. a heave velocity perturbation with no heave displacement and acceleration). Slow motion derivatives are considered best estimates to the hydrodynamic coefficients as higher order terms in a Taylor series expansion are assumed to drop out. Oscillatory coefficients become slow motion derivatives as the frequency becomes small and the motions "slow", however Bishop points out that it is not clear that slow motion derivatives approach the true derivatives as the frequency approaches zero. This paper will show how Bishop is correct in that frequency has a large impact on the calculated coefficients. It will also show how the amplitude of the motion also effects the calculated coefficients owing both to how the fluid differs in its evolution and how the motion can no longer be considered slow even at very small frequencies.

Virtual PMM tests, described in §1.10, perform PMM tests in a CFD (i.e. virtual) environment. They have been performed starting around 2006, when the first published papers performing URANS[2] simulations for a ship were released [4]. From there virtual PMM tests were extended to AUV's in [5]. Coe and Neu strengthened this field of work by performing verification analysis on spheroids undergoing heave perturbations in STAR-CCM+ [6]. Coe and Neu also explored the amplitude effects of PMM tests in [7], exposing how nonlinearities grow with increasing amplitude. This paper continues this line of research by exploring the effects of varying both the frequency and the amplitude on the response of the system and evaluating how this effects a given model's performance.

The description of flow topology, described in Appendix H, necessary to describe flows over a spheroid was formalized in the 1980's by scholars such as Tobak and Peak [8], Chapman [9], and Wang [10]. Here the authors describe a fundamental type of separation seen on spheroids at incidence; cross flow separation. Detailed real flow visualization studies were done on 1:2 and 1:4 spheroids in [11].

1.3 Thesis Organization

Section 1, *Introduction*, provides a semi-in-depth review of topics relevant to this paper including state space modeling of AUV's, a derivation of the EOM's for an arbitrary vehicle, PMM testing, and basic concepts of CFD.

Section 2, *Simulation Setup*, details the simulation setup including the domain and its boundary conditions including the body (an 8:1 spheroid), initial conditions, and spatial and temporal order convergence studies.

Section 3, *Flow Analysis of 8:1 Spheroid*, where a steady analysis is performed at various angles of attack to describe how the skin friction portrait over the body changes with angle of attack. This is done to help the reader understand what the fluid is doing while sweeping through angles of attack during a planar motion mechanism (PMM) test. Validity of quasi-steady models are also discussed.

[1] Oscillatory coefficients are called coefficients instead of derivatives because they are assumed to depend on the frequency of the motion.

[2] See §1.12 for explanation of URANS.

Section 4, *PMM Model Results and Discussion*, discusses how the 3 damping models performed for a range of PMM tests through both qualitative and quantitative type analysis. Also provides advice for carrying out PMM tests.

Section 5, *Future Research*, gives some ideas of what is needed to validate the results in this paper, and other areas of research this paper could lead towards.

Section 6, *Concluding Remarks*, summarizes the results presented with some final thoughts.

1.4 Kinematics and Dynamics of Rigid Bodies[3]

In this section we describe the kinematics and dynamics of a rigid body. Here we consider $\mathcal{F}_i$ to be an inertial reference frame[4] and $\mathcal{F}_b$ to be a body reference frame attached to the body where the origin is taken to be the center of mass, cm, as shown in Figure 1-1.

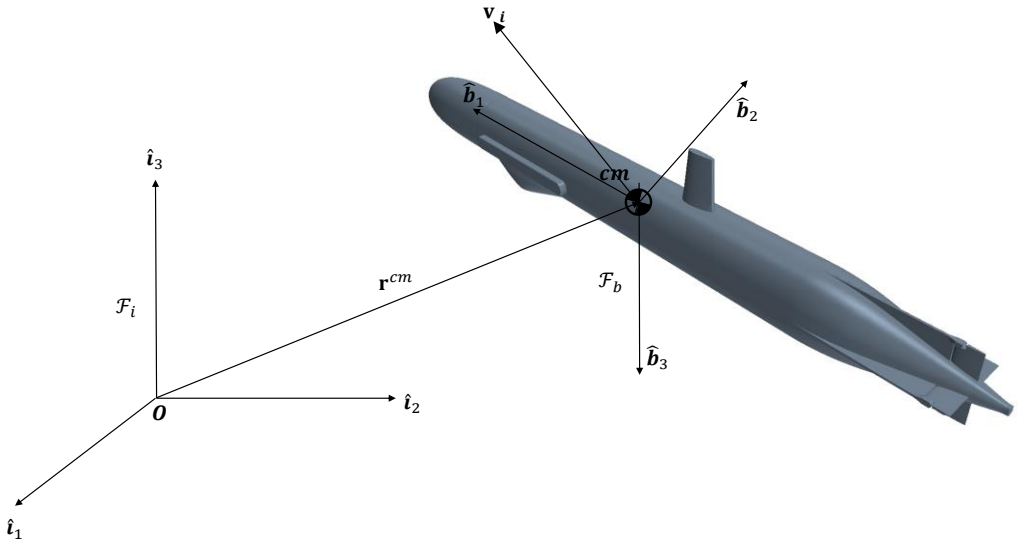

Figure 1-1: Figure showing the relationship between reference frames $\boldsymbol{\mathcal{F}_i}$ and $\boldsymbol{\mathcal{F}_b}$.

Rigid body dynamics are generally modeled using the Newton-Euler equations given by Equations (1.1) and (1.2), which describe the translational and rotational dynamics of a rigid body:

(Newton's Eqn.)
$$\mathbf{F}_i^{cm} = {}^{i}\frac{d}{dt}(\mathbf{p}_i) \tag{1.1}$$

[3] Rigid body: A body which has finite dimensions and is non-deformable (i.e. distance between any two points in and on the body remains constant).

[4] Inertial reference frame: A frame whose origin is fixed (i.e. not accelerating with respect to another inertial origin) and has 3 mutually orthonormal vectors which remain fixed with respect to inertial space.

(Euler's Eqn.)
$$\mathbf{L}_i = {}^{i}\frac{d}{dt}(\mathbf{h}_i^{cm}) \tag{1.2}$$

Here the left superscript on the derivative indicates that the derivative is taken with respect to the inertial reference frame, the right subscript i on vectors indicates the vector is expressed in the inertial reference frame. The superscript cm on **F** indicates that it is the total force acting on the body going through the center of mass, and the superscript cm on **h** indicates that it is the angular momentum about cm. **L** is the total moment applied to the body, and t is time. Here the linear momentum $\mathbf{p}_i$ and angular moment $\mathbf{h}_i$ can be expressed in the inertial reference frame as

$$\mathbf{p}_i = m\mathbf{v}_i^{cm} \tag{1.3}$$

$$\mathbf{h}_i^{cm} = \mathbf{I}_i^{cm}\boldsymbol{\omega}_i^{b/i} \tag{1.4}$$

where $\mathbf{v}_i$ is the velocity of the center of mass of the body, $\boldsymbol{\omega}_i^{b/i}$ is the angular velocity of $\mathcal{F}_b$ (i.e. the rigid body) when viewed from $\mathcal{F}_i$[5] and expressed in $\mathcal{F}_i$, $\mathbf{I}_i^{cm}$ is the 3×3 moment of inertia tensor of the body about the center of mass expressed in $\mathcal{F}_i$. The Newton-Euler equations hold for systems of particles, but can be extended to continuous rigid bodies (the type under consideration) as the number of particles representing the body approaches infinity in a suitable manner. The laws given by (1.1) and (1.2) are only valid in an inertial reference frame, but can be extended to systems expressed in any reference frame, such as the non-inertial reference frame $\mathcal{F}_b$, using the Transport Theorem to be discussed shortly.

Using the Euler rotations, such as the one shown in Figure 1-2, one can transform vectors and tensors expressed in $\mathcal{F}_i$ to vectors and tensors expressed in $\mathcal{F}_b$.

[5] This implies that $\boldsymbol{\omega}_i^{b/i} = -\boldsymbol{\omega}_i^{i/b}$ where $\boldsymbol{\omega}_i^{i/b}$ is the angular velocity of $\mathcal{F}_i$ when viewed from $\mathcal{F}_b$ and expressed in $\mathcal{F}_i$.

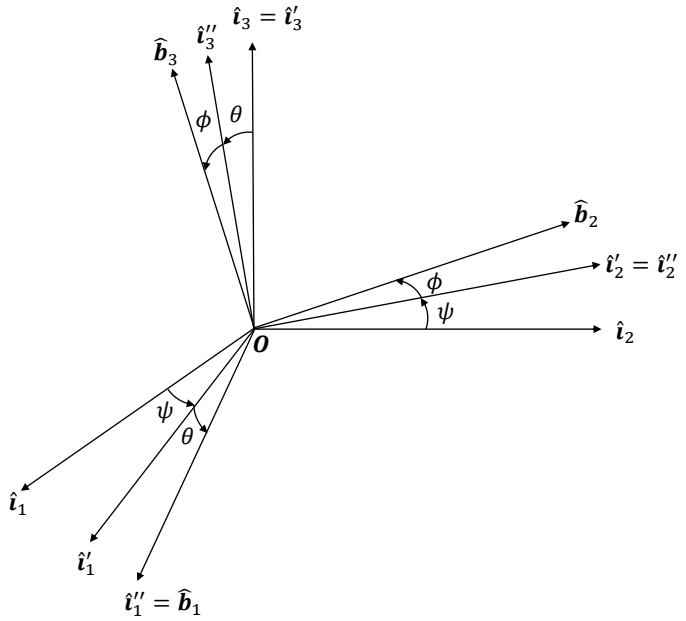

Figure 1-2: Diagram showing 3-2-1 Euler rotation.

Here we use a 3-2-1 rotation that first rotates the $\mathcal{F}_i$ frame about the $\hat{\boldsymbol{\imath}}_3$ axis by an angle ψ, then rotates the new $\mathcal{F}'$ frame about the $\hat{\boldsymbol{\imath}}'_2$ axes by the angle θ, and finally rotates this new $\mathcal{F}''$ frame about the $\hat{\boldsymbol{\imath}}''_1$ axis by an angle ϕ to 'align' the $\mathcal{F}_i$ frame with the body axes $\{\hat{\boldsymbol{b}}_1, \hat{\boldsymbol{b}}_2, \hat{\boldsymbol{b}}_3\}$ of $\mathcal{F}_b$. Here the angles $\{\phi, \theta, \psi\}$ are called the Euler angles. This rotation from one frame to another can be represented by the linear transform $\mathbf{R}^{bi}$ such that

$$\left[\hat{\boldsymbol{b}}_1, \hat{\boldsymbol{b}}_2, \hat{\boldsymbol{b}}_3\right] = \mathbf{R}^{bi}[\hat{\boldsymbol{\imath}}_1, \hat{\boldsymbol{\imath}}_2, \hat{\boldsymbol{\imath}}_3]$$

where the body frame unit vectors $\hat{\boldsymbol{b}}_i$ are given with respect to the inertial frame. From this, the following change of vector basis is defined,

$$\mathbf{a}_b = \mathbf{R}^{bi}\mathbf{a}_i \tag{1.5}$$

where $\mathbf{R}^{bi}$ is a rotation matrix from $\mathcal{F}_i$ to $\mathcal{F}_b$, $\mathbf{a}_i$ is an arbitrary vector expressed in $\mathcal{F}_i$ and $\mathbf{a}_b$ is the same vector but now expressed in $\mathcal{F}_b$. A 3-2-1 rotation matrix takes the form

$$\mathbf{R}^{bi} = \begin{bmatrix} c\psi c\theta & s\psi c\theta & -s\theta \\ c\psi s\theta s\phi - s\psi c\phi & c\psi c\phi + s\psi s\theta s\phi & \mathrm{c}\,\theta\, s\phi \\ s\psi s\phi + c\psi s\theta c\phi & s\psi s\theta c\phi - c\psi s\phi & c\theta c\phi \end{bmatrix} \tag{1.6}$$

where c and s are the cosine and sine functions respectively. Using the rotation matrix, the change of basis operation is defined for matrices as

$$\mathbf{N}_b = \mathbf{R}^{bi}\mathbf{N}_i\mathbf{R}^{ib} \tag{1.7}$$

which takes an arbitrary tensor $\mathbf{N}_i$ expressed in $\mathcal{F}_i$ and transforms it to a tensor $\mathbf{N}_b$ expressed in $\mathcal{F}_b$.

The Euler angles can be related to the body angular velocity by

$$\boldsymbol{\omega}_b^{b/i} = \boldsymbol{L}^{bi}\dot{\boldsymbol{\Theta}} \tag{1.8}$$

where $\dot{\boldsymbol{\Theta}} = \left[\dot{\phi}, \dot{\theta}, \dot{\psi}\right]^T$ and for a 3-2-1 rotation $\boldsymbol{L}^{bi}$ is given by

$$\boldsymbol{L}^{bi} = \begin{bmatrix} 1 & 0 & -\sin\theta \\ 0 & \cos\phi & \cos\theta\sin\phi \\ 0 & -\sin\phi & \cos\theta\cos\phi \end{bmatrix} \tag{1.9}$$

It is clear from (1.9) that when the Euler angles are small,

$$\boldsymbol{\omega}_b^{b/i} \cong \dot{\boldsymbol{\Theta}} \tag{1.10}$$

In order to use the Newton-Euler equations with vectors and tensors expressed in $\mathcal{F}_b$, a rotating reference frame, differential operations must remain with respect to an initially fixed frame such that the total change in the vector over time is taken into consideration. This is where the Transport Theorem is used. The Transport Theorem is used to differentiate a vector $\mathbf{a}_b$ expressed in $\mathcal{F}_b$ with respect to the inertial reference frame:

$$^{i}\frac{d}{dt}\mathbf{a}_{\mathrm{b}} = {}^{b}\frac{\partial}{\partial t}\mathbf{a}_{\mathrm{b}} + \boldsymbol{\omega}_b^{b/i} \times \mathbf{a}_b \tag{1.11}$$

where $^{i}\frac{d}{dt}\mathbf{a}_{\mathrm{b}}$ is the rate of change of $\mathbf{a}_{\mathrm{b}}$ as viewed from the inertial reference frame $\mathcal{F}_i$, $^{b}\frac{\partial}{\partial t}\mathbf{a}_{\mathrm{b}}$ is the rate of change of $\mathbf{a}_{\mathrm{b}}$ as view from the rotating reference frame $\mathcal{F}_b$, and "×" is the cross product of two vectors defined in Appendix A. Using this relation, the Newton-Euler equations can be equivalently cast as

$$\mathbf{F}_b = {}^{i}\frac{d}{dt}(\mathbf{p}_b) = \mathrm{m}\left(\dot{\mathbf{v}}_b^{cm} + \boldsymbol{\omega}_b^{b/i} \times \mathbf{v}_i^{cm}\right) \tag{1.12}$$

$$\mathbf{L}_b = {}^{i}\frac{d}{dt}(\mathbf{h}_b^{cm}) = \mathbf{I}_i^{cm}\dot{\boldsymbol{\omega}}_b^{b/i} + \boldsymbol{\omega}_b^{b/i} \times \left(\mathbf{I}_i^{cm}\boldsymbol{\omega}_b^{b/i}\right) \tag{1.13}$$

In summary, there are 12 nonlinear ordinary differential equations (ODE's), which together describe the body's kinematics and dynamics. They are:

Kinematics

$$\dot{\boldsymbol{r}}_i^{cm} = \mathbf{R}^{ib}\mathbf{v}_b^{cm}$$

$$\dot{\boldsymbol{\Theta}} = \boldsymbol{L}^{ib}\boldsymbol{\omega}_b^{b/i}$$

Dynamics

$$\mathbf{F}_b = \mathrm{m}\left(\dot{\mathbf{v}}_b^{cm} + \boldsymbol{\omega}_b^{b/i} \times \mathbf{v}_i^{cm}\right)$$

$$\mathbf{L}_b = \mathbf{I}_i^{cm}\dot{\boldsymbol{\omega}}_b^{b/i} + \boldsymbol{\omega}_b^{b/i} \times \left(\mathbf{I}_i^{cm}\boldsymbol{\omega}_b^{b/i}\right)$$

With knowledge of the initial conditions, applied force, $\mathbf{F}_b$, and moment, $\mathbf{L}_b$, these equations can theoretically be used to solve for the motion of the body.

1.5 State Space Modeling

State space modeling is a general method for describing the dynamics of a system as a set of first order ordinary differential equations generally written as

$$\frac{d}{dt}\mathbf{x}(t) = \dot{\mathbf{x}}(t) = \boldsymbol{f}(\mathbf{x}, \mathbf{u}, t) \tag{1.14}$$

where $\mathbf{x}(t)$ is an $n \times 1$ vector representing the state of the system at time t and $\mathbf{u}(t)$ is an $m \times 1$ vector of piecewise continuous inputs into the system. These equations are generally nonlinear, making them hard to find a closed form solution. Fortunately, many systems can be linearized about their nominal trajectory $\tilde{\mathbf{x}}(t)$ satisfying (1.14) such that the systems perturbations about its nominal trajectory can be represented as a set of linear ordinary differential equations of the form

$$\delta\dot{\mathbf{x}}(t) = \boldsymbol{A}(t)\delta\mathbf{x}(t) + \boldsymbol{B}(t)\delta\mathbf{u}(t) \tag{1.15}$$

where

$$\boldsymbol{A}(t) = \frac{\partial \boldsymbol{f}(\mathbf{x}, \mathbf{u}, t)}{\partial \mathbf{x}} \tag{1.16}$$

and

$$\boldsymbol{B}(t) = \frac{\partial \boldsymbol{f}(\mathbf{x}, \mathbf{u}, t)}{\partial \mathbf{u}} \tag{1.17}$$

Here $\boldsymbol{A}(t)$ is an $n \times n$ Jacobian matrix of piecewise continuous functions describing the systems dynamics corresponding to the perturbed state $\delta\mathbf{x}(t)$ and $\boldsymbol{B}(t)$ is the $n \times m$ Jacobian matrix of piecewise continuous functions corresponding to the perturbed input $\delta\mathbf{u}(t)$. The system dynamics then become $\mathbf{x}(t) \cong \tilde{\mathbf{x}}(t) + \delta\mathbf{x}(t)$, where $\delta\mathbf{x}(t)$ must remain 'small'[6] for the linearized equations to remain valid. Linearizing the systems dynamics is advantageous because analysis of the system's stability and observability characteristics is simple to perform for linear systems. Also, as will be shown, a linear model of the fluid dynamics for a body undergoing a PMM test can often times be adequate.

1.6 Equations of Motion of AUV's in an Ideal Fluid

The added mass of an AUV, often referred to as apparent mass or virtual mass, are the forces on the AUV due to its motion through an ideal fluid. These forces can be described as coming from the energy required to accelerate the fluid around an accelerating body. In this section, refer to Figure 1-3 for visual representation of the vector's meaning. Italicized variables generally refer to fluid variables while non-italicized variables generally refer to rigid body variables. In the following derivation, we consider a body immersed in an infinite fluid[7] initially at rest to be set in motion by an impulse wrench[8] such that the body is then traveling at a velocity $\mathbf{v} = [\mathrm{u}, \mathrm{v}, \mathrm{w}]^T$ where $\{\mathrm{u}, \mathrm{v}, \mathrm{w}\}$ are the linear velocities of the body parallel to $\hat{\boldsymbol{b}}_1$, $\hat{\boldsymbol{b}}_2$, and $\hat{\boldsymbol{b}}_3$ respectively, with angular velocity of $\boldsymbol{\omega} = [\mathrm{p}, \mathrm{q}, \mathrm{r}]^T$ where $\{\mathrm{p}, \mathrm{q}, \mathrm{r}\}$ are the angular velocities of the body about $\hat{\boldsymbol{b}}_1$, $\hat{\boldsymbol{b}}_2$, and $\hat{\boldsymbol{b}}_3$ respectively. Here the linear and angular velocities of the body are functions of time only, and the motion of the fluid is due entirely to the body's motion. Under these conditions and using results from section 3.77 in [12], the motion of the fluid is determinate.

[6] How 'small' $\delta\mathbf{x}(t)$ is defines how close the AUV remains to the nominal trajectory, and what is small enough depends on the nonlinear equations the linear equations are linearized from, and how well these equations represent the real physics of the system.

[7] An infinite fluid is a fluid which extends to infinity in all directions from the bodies surface

[8] An impulse wrench is a force moment couple $(\mathbf{F}, \mathbf{L})$ applied to the body for an infinitesimal amount of time.

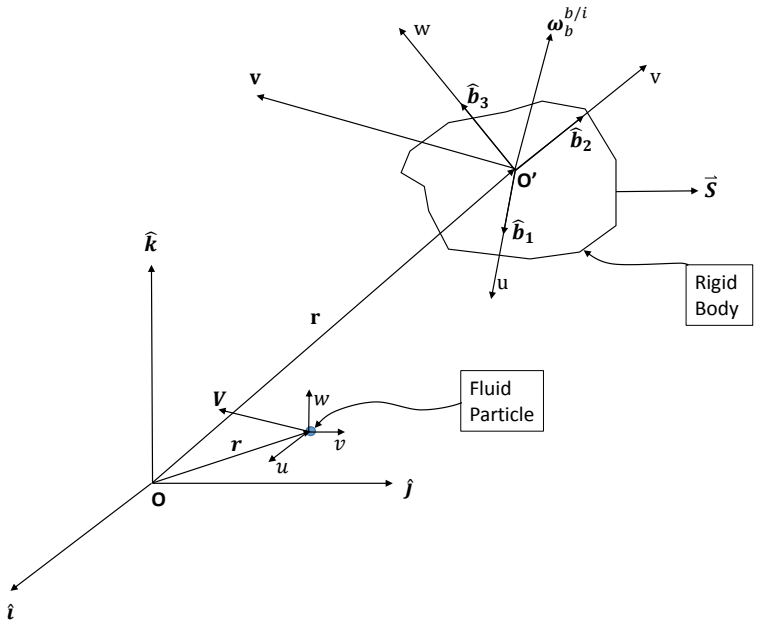

Figure 1-3: Diagram for added mass derivation

1.6.1 Ideal fluid

An ideal fluid is a fluid which is assumed to be inviscid and incompressible. The first condition implies that $\boldsymbol{\tau}' = \mathbf{0}$ where $\boldsymbol{\tau}'$ is the stress tensor caused by a fluids viscosity. This means that there are no viscous shear stresses acting on the fluid particles. The second condition implies the divergence of the velocity field is zero, or alternatively

$$\nabla \cdot \boldsymbol{V}_i = 0 \tag{1.18}$$

where $\boldsymbol{V}_i = \boldsymbol{V}_i(\boldsymbol{r}_i, t)$ is the velocity vector field of the fluid expressed in $\mathcal{F}_i$ and $\boldsymbol{r}_i$ is the position of the fluid particle expressed in $\mathcal{F}_i$. Subscript i will henceforth be dropped and all vectors are expressed in $\mathcal{F}_i$ unless otherwise noted.

1.6.2 Equations of Motion of an Ideal Fluid

The following are the differential equations of motion which govern the flow of an ideal fluid. The first is known as the continuity equation and takes the form of Equation (1.18). The second, known as Euler's equation, is a statement of the conservation of momentum of an ideal fluid and is shown in vector form below

$$\rho\left(\frac{\partial \boldsymbol{V}}{\partial t} + \boldsymbol{V} \cdot \nabla\, \boldsymbol{V}\right) = -\nabla p + \boldsymbol{F} \tag{1.19}$$

where $\boldsymbol{F}$ is a body force, ρ is the density of the fluid, and $p = p(\mathbf{r})$ is the pressure field at the point defined by the position vector $\boldsymbol{r}$.

1.6.3 Velocity Potential

The velocity potential $\phi(\boldsymbol{r}, t)$ is a single scalar function of position $\boldsymbol{r}$ and time t where the dependence on time enters through the bodies velocity $\boldsymbol{V}(t)$. A velocity potential exists when the flow is irrotational, where an irrotational flow satisfies $\nabla \times \boldsymbol{V} = \boldsymbol{0}$. According to Helmholtz's third theorem, an ideal fluid initially at rest will remain irrotational if all forces acting on it are irrotational. This means the fluid brought into motion by the body will remain acyclic[9]. With this final assumption, the equations of motion (1.18) and (1.19) can be reduced to solving a single equation called Laplace's equation, given as

$$\nabla^2 \phi = 0 \tag{1.20}$$

1.6.4 Boundary Conditions

There are two boundary conditions (BC's) which need to be enforced to solve Equation (1.20). The first is the boundary condition of an infinite distance from the body. Here we will assume that the fluid is otherwise undisturbed. In this sense, we will require $\boldsymbol{V}$ to be zero at infinity for all time. The second condition will require that the velocity of the fluid be equal to the velocity of the surface of the body (i.e. no flow through the surface). This can be stated mathematically as

$$\boldsymbol{V}_s \cdot \boldsymbol{n} = \boldsymbol{V} \cdot \boldsymbol{n} \text{ on S} \tag{1.21}$$

where S is the surface of the body, $\boldsymbol{V}_s$ is the velocity of the surface of the body and $\boldsymbol{n}$ is a unit vector normal to the surface of the body. We represent the surface of the fluid by the function

$$F(\boldsymbol{r}, t) = 0 \tag{1.22}$$

given with respect to the inertial coordinate system from which $\boldsymbol{n}$ can be defined as

$$\boldsymbol{n} = \pm \frac{grad\ F}{|grad\ F|} \tag{1.23}$$

where $\boldsymbol{n}$ is chosen as an outward unit normal vector.

[9] Acyclic motion is irrotational motion in a simply connected region such that the circulation is zero everywhere, where a simply connected region is one for which any two points in the domain are reconcilable (i.e. can be made to coincide through continuous variation of the path connecting the two points such that the path never leaves the region).

1.6.5 Added Mass via Kirchhoff's Equations

The following rough derivation of the added mass matrix will follow Lamb's derivation from [13] closely. This derivation is performed in a set of body fixed coordinates, $\{\hat{\boldsymbol{b}}\} = \{\hat{\boldsymbol{b}}_1, \hat{\boldsymbol{b}}_2, \hat{\boldsymbol{b}}_3\}$, and therefore the preceding equations must be transformed to $\mathcal{F}_b$. For the proof of how the preceding equations are affected by this change, see [14] pg 281. All of the proceeding variables will now be expressed in the $\mathcal{F}_b$ frame unless stated otherwise.

The system of equations we are trying to solve for the velocity potential are shown again below (now in the $\mathcal{F}_b$frame):

$$\nabla^2\phi = 0 \tag{1.24}$$

$$\boldsymbol{V}_s \cdot \boldsymbol{n} = \boldsymbol{V} \cdot \boldsymbol{n} \text{ on S} \tag{1.25}$$

$$\boldsymbol{V}\ at\ \infty = 0 \tag{1.26}$$

Because the velocity potential is the solution of the linear differential equation (1.24), and because its dependence on time enters only through the motion of the body, one may expand the velocity potential as

$$\phi = \mathrm{u}\varphi_1 + \mathrm{v}\varphi_2 + \mathrm{w}\varphi_3 + \mathrm{p}\varphi_4 + \mathrm{q}\varphi_5 + \mathrm{r}\varphi_6 \tag{1.27}$$

where φ_i is a function of position $\boldsymbol{r}$ only. It should be noted that the dimensions of φ_i for $i = 1 - 6$ are not dimensionally homogeneous, but the sum of the products of each term are. Because ϕ is given by linear differential equation (1.24), by the principle of superposition of linear differential equations, φ_i must independently satisfy (1.24) for $i = 1 - 6$. This means φ_i's may be solved for independently of one another, and then combined to form the velocity potential.

The boundary conditions satisfying (1.25) become

$$\begin{aligned} \frac{\partial\varphi_1}{\partial n} &= l, \quad \frac{\partial\varphi_4}{\partial n} = ny - mz \\ \frac{\partial\varphi_2}{\partial n} &= m, \quad \frac{\partial\varphi_5}{\partial n} = lz - nx \\ \frac{\partial\varphi_3}{\partial n} &= n, \quad \frac{\partial\varphi_6}{\partial n} = mx - ly \end{aligned} \tag{1.28}$$

where l, m, n denote the direction cosines normal to the surface of the body. Note that $\frac{\partial(\cdot)}{\partial n}$ directly means the change in "$\cdot$" in the direction of n, where n in this sense is the normal

direction at any point on the body's' surface. Refer to Appendix D for further explanation of how the boundary conditions given by (1.28) were derived.

The kinetic energy of a fluid is given by

$$T_L = \frac{1}{2}\iint_S \rho\phi \frac{\partial \phi}{\partial n} dS = \frac{\rho}{2}\iint_S \phi \, (grad \, \phi \cdot \boldsymbol{n}) \, dS \tag{1.29}$$

where

$$grad \, \phi \cdot \boldsymbol{n} = l(\mathrm{u} + \mathrm{q}z - \mathrm{r}y) + m(\mathrm{v} + \mathrm{r}x - \mathrm{p}z) + n(\mathrm{w} + \mathrm{p}y - \mathrm{q}x) \tag{1.30}$$

as is proven in [14] pg 301. Substituting (1.27) and (1.30) into (1.29) gives

$$\begin{aligned} T_L = \frac{1}{2}\iint_S [&(\mathrm{u}\varphi_1 + \mathrm{v}\varphi_2 + \mathrm{w}\varphi_3 + \mathrm{p}\varphi_4 + \mathrm{q}\varphi_5 + \mathrm{r}\varphi_6) \\ &(l(\mathrm{u} + \mathrm{q}z - \mathrm{r}y) + m(\mathrm{v} + \mathrm{r}x - \mathrm{p}z) + n(\mathrm{w} + \mathrm{p}y \\ &- \mathrm{q}x))]dS \end{aligned} \tag{1.31}$$

which, after multiplying everything out and noting $\{\mathrm{u}, \mathrm{v}, \mathrm{w}, \mathrm{p}, \mathrm{q}, \mathrm{r}\}$ are solely functions of time and can therefore can be taken out of the integral, can be written in the form

$$\begin{aligned} 2T_L = &\mathrm{X}_{\dot{\mathrm{u}}}\mathrm{u}^2 + \mathrm{Y}_{\dot{\mathrm{v}}}\mathrm{v}^2 + \mathrm{Z}_{\dot{\mathrm{w}}}\mathrm{w}^2 + 2\mathrm{Y}_{\dot{\mathrm{w}}}\mathrm{vw} + 2\mathrm{X}_{\dot{\mathrm{w}}}\mathrm{wu} + 2\mathrm{X}_{\dot{\mathrm{v}}}\mathrm{uv} \\ &+\mathrm{K}_{\dot{\mathrm{p}}}\mathrm{p}^2 + \mathrm{M}_{\dot{\mathrm{q}}}\mathrm{q}^2 + \mathrm{N}_{\dot{\mathrm{r}}}\mathrm{r}^2 + 2\mathrm{M}_{\dot{\mathrm{r}}}\mathrm{qr} + 2\mathrm{K}_{\dot{\mathrm{r}}}\mathrm{rp} + 2\mathrm{K}_{\dot{\mathrm{q}}}\mathrm{pq} \\ &+2\mathrm{p}\left(\mathrm{X}_{\dot{\mathrm{p}}}\mathrm{u} + \mathrm{Y}_{\dot{\mathrm{p}}}\mathrm{v} + \mathrm{Z}_{\dot{\mathrm{p}}}\mathrm{w}\right) \\ &+2\mathrm{q}\left(\mathrm{X}_{\dot{\mathrm{q}}}\mathrm{u} + \mathrm{Y}_{\dot{\mathrm{q}}}\mathrm{v} + \mathrm{Z}_{\dot{\mathrm{q}}}\mathrm{w}\right) \\ &+2\mathrm{r}(\mathrm{X}_{\dot{\mathrm{r}}}\mathrm{u} + \mathrm{Y}_{\dot{\mathrm{r}}}\mathrm{v} + \mathrm{Z}_{\dot{\mathrm{r}}}\mathrm{w}) \end{aligned} \tag{1.32}$$

where the coefficients $\mathrm{X}_{\dot{\mathrm{u}}}$, $\mathrm{X}_{\dot{\mathrm{v}}}$, $\mathrm{X}_{\dot{\mathrm{w}}}$, $\mathrm{X}_{\dot{\mathrm{p}}}$, $\mathrm{X}_{\dot{\mathrm{q}}}$, $\mathrm{X}_{\dot{\mathrm{r}}}$, $\mathrm{Y}_{\dot{\mathrm{v}}}$, $\mathrm{Y}_{\dot{\mathrm{w}}}$, $\mathrm{Y}_{\dot{\mathrm{p}}}$, $\mathrm{Y}_{\dot{\mathrm{q}}}$, $\mathrm{Y}_{\dot{\mathrm{r}}}$, $\mathrm{Z}_{\dot{\mathrm{w}}}$, $\mathrm{Z}_{\dot{\mathrm{p}}}$, $\mathrm{Z}_{\dot{\mathrm{q}}}$, $\mathrm{Z}_{\dot{\mathrm{r}}}$, $\mathrm{K}_{\dot{\mathrm{p}}}$, $\mathrm{K}_{\dot{\mathrm{q}}}$, $\mathrm{K}_{\dot{\mathrm{r}}}$, $\mathrm{M}_{\dot{\mathrm{q}}}$, $\mathrm{M}_{\dot{\mathrm{r}}}$, and $\mathrm{N}_{\dot{\mathrm{r}}}$ are the added mass coefficients given explicitly in Appendix E.

The kinetic energy of the body is given by

$$T_S = \frac{1}{2}\iiint_{\mathrm{V}} \sigma \mathbf{v}_\tau^2 \, d\tau \tag{1.33}$$

where $\mathbf{v}_\tau$ is the velocity of each differential element $d\tau$ in the body, σ is the density of the body, and V is the volume of the body. The total kinetic energy of the system is then given as

$$T = T_S + T_L \tag{1.34}$$

With knowledge of the total kinetic energy of the system, Kirchhoff's equations of motion (relating the energy of the system to the bodies states), derived in Appendix C, can be given as

$$^{i}\frac{d}{dt}\left(\frac{\partial T}{\partial \mathbf{v}}\right) = {}^{b}\frac{\partial}{\partial t}\left(\frac{\partial T}{\partial \mathbf{v}}\right) + \boldsymbol{\omega} \times \frac{\partial T}{\partial \mathbf{v}} = \mathbf{F} \tag{1.35}$$

$$^{i}\frac{d}{dt}\left(\frac{\partial T}{\partial \boldsymbol{\omega}}\right) = {}^{b}\frac{\partial}{\partial t}\left(\frac{\partial T}{\partial \boldsymbol{\omega}}\right) + \boldsymbol{\omega} \times \frac{\partial T}{\partial \boldsymbol{\omega}} + \mathbf{v} \times \frac{\partial T}{\partial \mathbf{v}} = \mathbf{L} \tag{1.36}$$

where

$$\frac{\partial T}{\partial \boldsymbol{\omega}} = \frac{\partial T}{\partial \mathrm{p}}\widehat{\boldsymbol{b}}_1 + \frac{\partial T}{\partial \mathrm{q}}\widehat{\boldsymbol{b}}_2 + \frac{\partial T}{\partial \mathrm{r}}\widehat{\boldsymbol{b}}_3 \tag{1.37}$$

and

$$\frac{\partial T}{\partial \mathbf{v}} = \frac{\partial T}{\partial \mathrm{u}}\widehat{\boldsymbol{b}}_1 + \frac{\partial T}{\partial \mathrm{v}}\widehat{\boldsymbol{b}}_2 + \frac{\partial T}{\partial \mathrm{w}}\widehat{\boldsymbol{b}}_3 \tag{1.38}$$

and (**F,L**) are a force moment couple applied to the body, and $\boldsymbol{\omega}$ is the angular velocity of $\mathcal{F}_b$, can be used to derive the final form of the equations of motion of the vehicle. Again, the superscript on the top left of the derivative denotes with which frame the derivative is taken with respect to. Kirchhoff's equations, given by (1.35) and (1.36), can be expanded to be of the following form

$$
\begin{aligned}
{}^{i}\frac{d}{dt}\left(\frac{\partial T}{\partial \mathrm{u}}\right) &= \mathrm{r}\frac{\partial T}{\partial \mathrm{v}} - q\frac{\partial T}{\partial \mathrm{w}} + \mathrm{X} \\
{}^{i}\frac{d}{dt}\left(\frac{\partial T}{\partial \mathrm{v}}\right) &= \mathrm{p}\frac{\partial T}{\partial w} - \mathrm{r}\frac{\partial T}{\partial \mathrm{u}} + \mathrm{Y} \\
{}^{i}\frac{d}{dt}\left(\frac{\partial T}{\partial \mathrm{w}}\right) &= \mathrm{q}\frac{\partial T}{\partial \mathrm{u}} - \mathrm{p}\frac{\partial T}{\partial \mathrm{v}} + \mathrm{Z} \\
{}^{i}\frac{d}{dt}\left(\frac{\partial T}{\partial \mathrm{p}}\right) &= \mathrm{w}\frac{\partial T}{\partial \mathrm{v}} - \mathrm{v}\frac{\partial T}{\partial \mathrm{w}} + \mathrm{r}\frac{\partial T}{\partial \mathrm{q}} - \mathrm{q}\frac{\partial T}{\partial \mathrm{r}} + \mathrm{L} \\
{}^{i}\frac{d}{dt}\left(\frac{\partial T}{\partial \mathrm{q}}\right) &= \mathrm{u}\frac{\partial T}{\partial \mathrm{w}} - \mathrm{v}\frac{\partial T}{\partial \mathrm{u}} + \mathrm{p}\frac{\partial T}{\partial \mathrm{r}} - \mathrm{r}\frac{\partial T}{\partial \mathrm{p}} + \mathrm{M} \\
{}^{i}\frac{d}{dt}\left(\frac{\partial T}{\partial \mathrm{r}}\right) &= \mathrm{v}\frac{\partial T}{\partial \mathrm{u}} - \mathrm{u}\frac{\partial T}{\partial \mathrm{v}} + \mathrm{q}\frac{\partial T}{\partial \mathrm{p}} - \mathrm{p}\frac{\partial T}{\partial \mathrm{q}} + \mathrm{N}
\end{aligned}
\tag{1.39}
$$

where X, Y, Z are the linear force components of **F** along the $\hat{\boldsymbol{b}}_1$, $\hat{\boldsymbol{b}}_2$, and $\hat{\boldsymbol{b}}_3$ axes respectively, L, M, N are the moment components of **L** along the $\hat{\boldsymbol{b}}_1$, $\hat{\boldsymbol{b}}_2$, and $\hat{\boldsymbol{b}}_3$ axes respectively, and T is the total kinetic energy of the system as given by (1.34). The added mass forces and moments exerted by the fluid can be computed using Equation (1.32) by substituting $T = T_L$ into equation (1.39). This results in the following EOM's which essentially describe the dynamics of a massless body:

$$
\begin{aligned}
\mathrm{X_L} = {} & \mathrm{X_{\dot{u}}}\dot{\mathrm{u}} + \mathrm{X_{\dot{w}}}(\dot{\mathrm{w}} + \mathrm{uq}) + \mathrm{X_{\dot{q}}}\dot{\mathrm{q}} + \mathrm{Z_{\dot{w}}}\mathrm{wq} + \mathrm{Z_{\dot{q}}}\mathrm{q}^2 \\
& + \mathrm{X_{\dot{v}}}\dot{\mathrm{v}} + \mathrm{X_{\dot{p}}}\dot{\mathrm{p}} + \mathrm{X_{\dot{r}}}\dot{\mathrm{r}} - \mathrm{Y_{\dot{v}}}\mathrm{vr} - \mathrm{Y_{\dot{p}}}\mathrm{rp} - \mathrm{Y_{\dot{r}}}\mathrm{r}^2 \\
& - \mathrm{X_{\dot{v}}}\mathrm{ur} - \mathrm{Y_{\dot{w}}}\mathrm{wr} \\
& + \mathrm{Y_{\dot{w}}}\mathrm{vq} + \mathrm{Z_{\dot{p}}}\mathrm{pq} - \left(\mathrm{Y_{\dot{q}}} - \mathrm{Z_{\dot{r}}}\right)\mathrm{qr}
\end{aligned}
\tag{1.40}
$$

$$
\begin{aligned}
\mathrm{Y_L} = {} & \mathrm{X_{\dot{v}}}\dot{\mathrm{u}} + \mathrm{Y_{\dot{w}}}\dot{\mathrm{w}} + \mathrm{Y_{\dot{q}}}\dot{\mathrm{q}} \\
& + \mathrm{Y_{\dot{v}}}\dot{\mathrm{v}} + \mathrm{Y_{\dot{p}}}\dot{\mathrm{p}} + \mathrm{Y_{\dot{r}}}\dot{\mathrm{r}} + \mathrm{X_{\dot{v}}}\mathrm{vr} - \mathrm{Y_{\dot{w}}}\mathrm{vp} + \mathrm{X_{\dot{r}}}\mathrm{r}^2 + \left(\mathrm{X_{\dot{p}}} - \mathrm{Z_{\dot{r}}}\right)\mathrm{rp} - \mathrm{Z_{\dot{p}}}\mathrm{p}^2 \\
& - \mathrm{X_{\dot{w}}}(\mathrm{up} - \mathrm{wr}) + \mathrm{X_{\dot{u}}}\mathrm{ur} - \mathrm{Z_{\dot{w}}}\mathrm{wp} \\
& - \mathrm{Z_{\dot{q}}}\mathrm{pq} + \mathrm{X_{\dot{q}}}\mathrm{qr}
\end{aligned}
\tag{1.41}
$$

$$
\begin{aligned}
\mathrm{Z_L} = {} & \mathrm{X_{\dot{w}}}(\dot{\mathrm{u}} - \mathrm{wq}) + \mathrm{Z_{\dot{w}}}\dot{\mathrm{w}} + \mathrm{Z_{\dot{q}}}\dot{\mathrm{q}} - \mathrm{X_{\dot{u}}}\mathrm{uq} - \mathrm{X_{\dot{q}}}\mathrm{q}^2 \\
& + \mathrm{Y_{\dot{w}}}\dot{\mathrm{v}} + \mathrm{Z_{\dot{p}}}\dot{\mathrm{p}} + \mathrm{Z_{\dot{r}}}\dot{\mathrm{r}} + \mathrm{Y_{\dot{v}}}\mathrm{vp} + \mathrm{Y_{\dot{r}}}\mathrm{rp} + \mathrm{Y_{\dot{p}}}\mathrm{p}^2 \\
& + \mathrm{X_{\dot{v}}}\mathrm{up} + \mathrm{Y_{\dot{w}}}\mathrm{wp} \\
& - \mathrm{X_{\dot{v}}}\mathrm{vq} - \left(\mathrm{X_{\dot{p}}} - \mathrm{Y_{\dot{q}}}\right)\mathrm{pq} - \mathrm{X_{\dot{r}}}\mathrm{qr}
\end{aligned}
\tag{1.42}
$$

$$\begin{aligned}
K_L = {} & X_{\dot{p}}\dot{u} + Z_{\dot{p}}\dot{w} + K_{\dot{q}}\dot{q} - X_{\dot{v}}wu + X_{\dot{r}}uq - Y_{\dot{w}}w^2 - \left(Y_{\dot{p}} - Z_{\dot{r}}\right)wq + M_{\dot{r}}q^2 \\
& + Y_{\dot{p}}\dot{v} + K_{\dot{p}}\dot{p} + K_{\dot{r}}\dot{r} + Y_{\dot{w}}v^2 - \left(Y_{\dot{q}} - Z_{\dot{r}}\right)vr + Z_{\dot{p}}vp - M_{\dot{r}}r^2 - K_{\dot{q}}rp \\
& + X_{\dot{w}}uv - (Y_{\dot{v}} - Z_{\dot{w}})vw - \left(Y_{\dot{r}} + Z_{\dot{q}}\right)wr - Y_{\dot{p}}wp - X_{\dot{q}}ur \\
& + \left(Y_{\dot{r}} + Z_{\dot{q}}\right)vq + K_{\dot{r}}pq - \left(M_{\dot{q}} - N_{\dot{r}}\right)qr
\end{aligned} \tag{1.43}$$

$$\begin{aligned}
M_L = {} & X_{\dot{q}}(\dot{u} + wq) + Z_{\dot{q}}(\dot{w} - uq) + M_{\dot{q}}\dot{q} - X_{\dot{w}}(u^2 - w^2) - (Z_{\dot{w}} - X_{\dot{u}})wu \\
& + Y_{\dot{q}}\dot{v} + K_{\dot{q}}\dot{p} + M_{\dot{r}}\dot{r} + Y_{\dot{p}}vr - Y_{\dot{r}}vp - K_{\dot{r}}\left(p^2 - r^2\right) + \left(K_{\dot{p}} - N_{\dot{r}}\right)rp \\
& - Y_{\dot{w}}uv + X_{\dot{v}}vw - \left(X_{\dot{r}} + Z_{\dot{p}}\right)(up - wr) + \left(X_{\dot{p}} - Z_{\dot{r}}\right)(wp + ur) \\
& - M_{\dot{r}}pq + K_{\dot{q}}qr
\end{aligned} \tag{1.44}$$

$$\begin{aligned}
N_L = {} & X_{\dot{r}}\dot{u} + Z_{\dot{r}}\dot{w} + M_{\dot{r}}\dot{q} + X_{\dot{v}}u^2 + Y_{\dot{w}}wu - \left(X_{\dot{p}} - Y_{\dot{q}}\right)uq - Z_{\dot{p}}wq - K_{\dot{q}}q^2 \\
& + Y_{\dot{r}}\dot{v} + K_{\dot{r}}\dot{p} + N_{\dot{r}}\dot{r} - X_{\dot{v}}v^2 - X_{\dot{r}}vr - \left(X_{\dot{p}} - Y_{\dot{q}}\right)vp + M_{\dot{r}}rp + K_{\dot{q}}p^2 \\
& - (X_{\dot{u}} - Y_{\dot{v}})uv - X_{\dot{w}}vw + \left(X_{\dot{q}} + Y_{\dot{p}}\right)up + Y_{\dot{r}}ur + Z_{\dot{q}}wp \\
& - \left(X_{\dot{q}} + Y_{\dot{p}}\right)vq - \left(K_{\dot{p}} - M_{\dot{q}}\right)pq - K_{\dot{r}}qr
\end{aligned} \tag{1.45}$$

Using notation popularized by Fossen [15], Equations (1.40)-(1.45) can be cast in state space form as

$$-\mathbf{M}_A\dot{\boldsymbol{\eta}} + \mathbf{C}_A\left(\boldsymbol{\omega}^{b/i}\right)\boldsymbol{\eta} = \begin{bmatrix}\mathbf{F} \\ \mathbf{L}\end{bmatrix} \tag{1.46}$$

where $\boldsymbol{M}_A$ and $\boldsymbol{C}_A(\boldsymbol{\eta})$ are defined in Appendix F and $\boldsymbol{\eta}$ is the state vector of the body given as

$$\boldsymbol{\eta} = \begin{bmatrix}\mathbf{v} \\ \boldsymbol{\omega}^{b/i}\end{bmatrix} = \begin{bmatrix} u \\ v \\ w \\ p \\ q \\ r \end{bmatrix} \tag{1.47}$$

Note the minus sign appears in front of the added mass matrix because of the way it was defined in Appendix F.

1.7 State Space Modeling of AUV's

Application of the equations of motion derived for ideal fluids to real fluids can be useful in gaining insight into the forces one may expect on a body performing slow motions. Here we consider slow motions as defined in [3] to be motions such that $\varsigma/\dot{\varsigma}$,

$\dot{\varsigma}/\ddot{\varsigma}$, $\ddot{\varsigma}/\dddot{\varsigma}$, …, where ς is a perturbation to the underwater vehicles nominal motion, are much less than u_0/L.

For real fluids, however, viscous effects must be taken into account because they make up a significant portion of the forces on the body. At the time of writing this thesis, no general model (linear or nonlinear) able to accurately account for a body going through general motions has been prescribed and agreed upon. However, restricting the body to slow motions as defined above allows for one to assume the flow to behave in a fairly linear fashion in response to the vehicle's motion. Once the motions can no longer be assumed to be slow, the nonlinearities cannot be assumed to be negligible.

In state space form, the full equations of motion used to model the dynamics of a rigid body in a viscous fluid are given as

$$\mathbf{M}\dot{\boldsymbol{\eta}} + \mathbf{C}(\boldsymbol{\eta})\boldsymbol{\eta} + \mathbf{D}(\boldsymbol{\eta})\boldsymbol{\eta} = \begin{bmatrix}\mathbf{F}\\ \mathbf{L}\end{bmatrix} \tag{1.48}$$

where $\mathbf{F}$ and $\mathbf{L}$ are other applied forces and torques respectively on the body other than those caused by the fluid, $\mathbf{M} = \mathbf{M}_{\mathrm{RB}} - \mathbf{M}_{\mathrm{A}}$ is an inertial matrix, $\mathbf{C}(\boldsymbol{\eta})$ is a Coriolis matrix due to the rotating coordinate system, and $\mathbf{D}$ is the damping matrix. For more details on matrices $\mathbf{M}$, $\mathbf{C}(\boldsymbol{\eta})$, and $\mathbf{D}$ see Appendix F. Note here that $\mathbf{M}_A$ is not necessarily symmetric as it would be in an ideal flow but will be assumed to be symmetric such that matrix $\mathbf{M}$ is also symmetric. Because the body fixed frame is fixed, $\mathbf{M}$ is a constant matrix. Matrices $\mathbf{C}$ and $\mathbf{D}$, however, are not in general constant, as they depend on time through the body's state $\boldsymbol{\eta}$. This makes (1.48) nonlinear in the state $\boldsymbol{\eta}$. Note that forces due to gravity such as the body's weight and buoyancy were not included in the model because they are assumed constant and can easily be added to equation (1.48).

An important assumption one implicitly makes when using this state space model is that the forces on the body are solely a function of the body's current state. This assumption is often referred to as the assumption of 'quasi-steady' flow, and it can be interpreted as meaning that the current state of the body (position, velocity, acceleration) defines the current state of the flow field. In this sense, the fluid is assumed to have no memory (i.e. the state of the fluid does not depend on previous states of the body). An attempt was made by Bishop and Parkinson [3] to account for memory effects using Volterra series; however, the utility of this model in deriving control laws remains to be seen.

Assuming both port/starboard symmetry of the body and symmetry of the added mass matrix, the mass matrix $\mathbf{M}$ is reduced to just 14 coefficients. This is because the added mass matrix becomes sparse (as can be shown using equations for the added mass coefficients given in Appendix F) such that

$$\mathbf{M}_A = \begin{bmatrix} X_{\dot{u}} & 0 & X_{\dot{w}} & 0 & X_{\dot{q}} & 0 \\ 0 & Y_{\dot{v}} & 0 & Y_{\dot{p}} & 0 & Y_{\dot{r}} \\ X_{\dot{w}} & 0 & Z_{\dot{w}} & 0 & Z_{\dot{q}} & 0 \\ 0 & Y_{\dot{p}} & 0 & K_{\dot{p}} & 0 & K_{\dot{r}} \\ X_{\dot{q}} & 0 & Z_{\dot{q}} & 0 & M_{\dot{q}} & 0 \\ 0 & Y_{\dot{r}} & 0 & K_{\dot{r}} & 0 & N_{\dot{r}} \end{bmatrix} \tag{1.49}$$

Writing (1.48) in the form of (1.14)

$$\dot{\boldsymbol{\eta}} = \mathbf{M}^{-1}\left(-\mathbf{C}(\boldsymbol{\eta})\boldsymbol{\eta} - \mathbf{D}(\boldsymbol{\eta})\boldsymbol{\eta} + \begin{bmatrix}\mathbf{F}\\ \mathbf{L}\end{bmatrix}\right) \tag{1.50}$$

where $\mathbf{M}^{-1}$ is the inverse of $\mathbf{M}$ such that $\mathbf{M}^{-1}\mathbf{M} = \boldsymbol{I}$ and exists because $\mathbf{M}$ is positive definite. Linearization of equation (1.50) about a nominal trajectory $\boldsymbol{\eta_0}$ satisfying (1.50) with zero angular velocity such that $p_0=q_0=r_0=0$ (which makes $\mathbf{C}=\mathbf{0}$) gives

$$\delta\dot{\boldsymbol{\eta}} = \mathbf{M}^{-1}\left(-\left.\frac{\partial \mathbf{D}(\boldsymbol{\eta})}{\partial \boldsymbol{\eta}}\right|_{\boldsymbol{\eta_0}} \delta\boldsymbol{\eta} + \begin{bmatrix}\delta\mathbf{F}\\ \delta\mathbf{L}\end{bmatrix}\right) \tag{1.51}$$

where δ in front of the variable represents a 'small' perturbation in that variable, $\left.\frac{\partial \mathbf{D}}{\partial \boldsymbol{\eta}}\right|_{\boldsymbol{\eta_0}}$ is the Jacobian of the damping matrix $\mathbf{D}$ with respect to the state $\boldsymbol{\eta}$ evaluated at $\boldsymbol{\eta_0}$, and

$$\boldsymbol{\eta} = \boldsymbol{\eta_0} + \delta\boldsymbol{\eta} \tag{1.52}$$

Note these linearized equations have the same form as (1.15) with the following equivalencies:

$$\boldsymbol{A} = -\mathbf{M}^{-1}\left.\frac{\partial \mathbf{D}(\boldsymbol{\eta})}{\partial \boldsymbol{\eta}}\right|_{\boldsymbol{\eta_0}} = const. \tag{1.53}$$

$$\boldsymbol{B} = \mathbf{M}^{-1} = const. \tag{1.54}$$

$$\mathbf{x}(t) = \boldsymbol{\eta}(t) \tag{1.55}$$

$$\mathbf{u}(t) = \begin{bmatrix}\delta\mathbf{F}(t)\\ \delta\mathbf{L}(t)\end{bmatrix} \tag{1.56}$$

The linearized equations of motion can then be rewritten to be of a similar form to (1.48) as

$$\mathbf{M}\delta\dot{\boldsymbol{\eta}} + \left.\frac{\partial \mathbf{D}(\boldsymbol{\eta})}{\partial \boldsymbol{\eta}}\right|_{\boldsymbol{\eta}_0} \delta\boldsymbol{\eta} = \begin{bmatrix}\delta\mathbf{F} \\ \delta\mathbf{L}\end{bmatrix} \tag{1.57}$$

With this model, the assumption is now that the perturbed states, $\delta\boldsymbol{\eta}$, remain small (i.e. slow motion).

1.8 Damping Matrix

The damping matrix $\mathbf{D}$ can take on many forms. In this study, a linear model, a quadratic model, and a combined linear/quadratic model were considered. In all of these models, it is assumed that this matrix accounts for both the viscous drag on the body and the pressure drag due to incomplete pressure recovery on the aft portion of the body caused by flow separation. Note that use of the quadratic and combined linear/quadratic models for the damping matrix in the linearized EOM removes the linearity of the equations of motion.

1.8.1 Linear Damping

The equations of motion for the linear damping model take the form

$$\mathbf{M}\delta\dot{\boldsymbol{\eta}} + \mathbf{D}_l\delta\boldsymbol{\eta} = \begin{bmatrix}\delta\mathbf{F} \\ \delta\mathbf{L}\end{bmatrix} \tag{1.58}$$

where the linear damping matrix

$$\mathbf{D}_l = \mathrm{diag}\left(\mathrm{D_u}, \mathrm{D_v}, \mathrm{D_w}, \mathrm{D_p}, \mathrm{D_q}, \mathrm{D_r}\right) = const. \tag{1.59}$$

and

$$\mathrm{diag}(\alpha_1, \alpha_2, \cdots, \alpha_n,) = \begin{bmatrix}\alpha_1 & 0 & \cdots & 0 \\ 0 & \alpha_2 & \ddots & \vdots \\ \vdots & \ddots & \ddots & 0 \\ 0 & \cdots & 0 & \alpha_n\end{bmatrix} \tag{1.60}$$

such that drag is directly proportional to the body's respective component of velocity. An advantage to this model is that it can be directly related to the linearized EOM given by (1.57), whereas the quadratic and combined linear/quadratic damping forms of the damping matrix cannot.

1.8.2 Quadratic and Combined Linear/Quadratic Damping

The equations of motion used with the quadratic and combined linear/quadratic model take the form

$$\mathbf{M}\delta\dot{\boldsymbol{\eta}} + \mathbf{D}(\delta\boldsymbol{\eta})\delta\boldsymbol{\eta} = \begin{bmatrix}\delta\mathbf{F}\\ \delta\mathbf{L}\end{bmatrix} \tag{1.61}$$

where the damping matrix is now a function of the perturbed state $\delta\boldsymbol{\eta}$. Here the quadratic form of the damping matrix is given as

$$\begin{aligned}&\mathbf{D}(\boldsymbol{\eta}) = \mathbf{D}_q(\boldsymbol{\eta})\\ &= \mathrm{diag}\left(\mathrm{D_{u|u|}}|\mathrm{u}|, \mathrm{D_{v|v|}}|\mathrm{v}|, \mathrm{D_{w|w|}}|\mathrm{w}|, \mathrm{D_{p|p|}}|\mathrm{p}|, \mathrm{D_{q|q|}}|\mathrm{q}|, \mathrm{D_{r|r|}}|\mathrm{r}|\right)\end{aligned} \tag{1.62}$$

such that drag is proportional to the square of the body's respective component of velocity. The use of the absolute values is to force positive velocities to produce negative drag forces. Combining the two models gives the combined linear/quadratic model:

$$\mathbf{D}(\boldsymbol{\eta}) = \mathbf{D}_c(\boldsymbol{\eta}) = \mathbf{D}_l + \mathbf{D}_q(\boldsymbol{\eta}) \tag{1.63}$$

1.9 PMM Testing

Planar motion mechanism (PMM) testing is a type of captive model testing performed to determine coefficients used in state-space models of bodies moving in a fluid. In this work we consider virtual PMM testing of underwater bodies via CFD simulations rather than using physical models. This virtual testing is applicable to all types of bodies and is explained further in §1.10.

In a PMM test, a model is towed at its nominal operating speed, and oscillated sinusoidally according to

$$\varsigma = -a_0 \cos(\omega t) \tag{1.64}$$

$$\dot{\varsigma} = a_0 \omega \sin(\omega t) \tag{1.65}$$

$$\ddot{\varsigma} = a_0 \omega^2 \cos(\omega t) \tag{1.66}$$

where a_0 is the amplitude of the oscillation, $\omega = 2\pi f$ is the angular frequency of the oscillation, and f is the frequency of oscillation. Such oscillations create velocities and

accelerations in a single degree of freedom (DOF). All PMM tests in this paper were of a spheroidal body in heave, as shown in Figure 1-4.

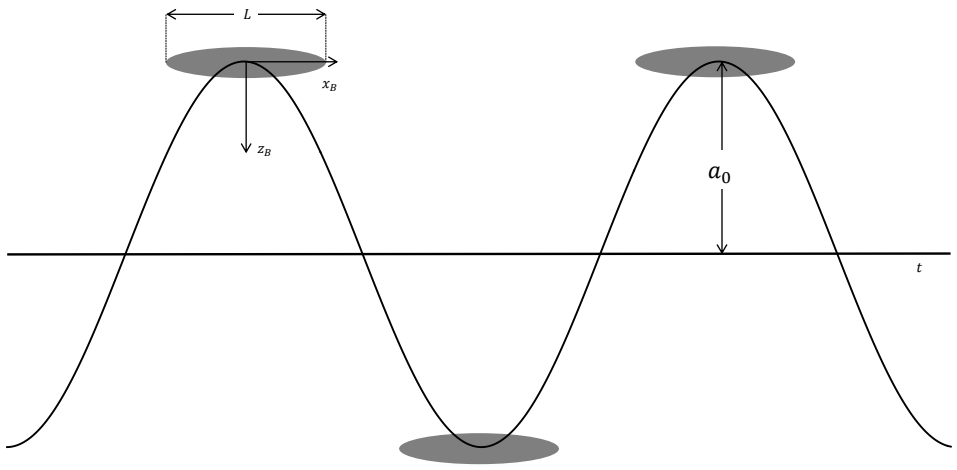

Figure 1-4: Example heave PMM test of spheroid tested virtually in this paper.

It is often advantageous to nondimensionalize equations (1.64)-(1.66) using the characteristic length, L, and velocity, u_0, of the vehicle such that

$$\varsigma' = -a_0' \cos(\omega' t') \tag{1.67}$$

$$\dot{\varsigma}' = a_0' \omega' \sin(\omega' t') \tag{1.68}$$

$$\ddot{\varsigma}' = a_0' \, \omega'^2 \cos(\omega' t') \tag{1.69}$$

where $\omega' = \frac{\omega L}{u_0} = 2\pi f'$, $a_0' = \frac{a_0}{L}$, and $t' = \frac{t u_0}{L}$.

Forces on the model are measured as a function of time and control derivatives for that degree of freedom can be determined by fitting a predetermined curve appropriate to the model through the force time history data. Forces, added mass coefficients, and damping coefficients are nondimensionalized such that

$$\mathrm{F}' = \frac{\mathrm{F}}{1/2 \rho u_0^2 L^2} \tag{1.70}$$

$$F'_{\ddot{\varsigma}'} = \frac{F_{\ddot{\varsigma}}}{1/2\rho L^3} \tag{1.71}$$

$$F'_{\dot{\varsigma}'} = \frac{F_{\dot{\varsigma}}}{1/2\rho u_0 L^2} \tag{1.72}$$

where F is the force in the ς DOF.

For PMM testing in sway and heave, it is also useful to define the angle of attack that the oncoming flow sweeps through with respect to the body's longitudinal axis

$$\alpha = \tan^{-1}\frac{max(\dot{\varsigma})}{u_0} \tag{1.73}$$

where $max(\dot{\varsigma})$ is the largest value of the perturbed velocity in the sway or heave direction[10]. This measure gives an idea of the severity of the flow separation that the body will undergo during the test.

The advantage of PMM testing over other methods for physically obtaining the coefficients such as straight line towing and rotary arms is that a PMM system can impart "hydrodynamically pure" linear and angular velocities and accelerations. This allows for the explicit calculation of the coefficients needed in the state-space model [2].

1.10 Virtual PMM Testing

There are three clear advantages virtual PMM testing offers over real PMM testing. Firstly, many immeasurable features in a real PMM test become readily available in a simulation. For example, the discretized pressure field throughout the entire domain can be extracted from a simulation. Secondly, while computation time is not free, it is often times much cheaper than the equivalent real test in the physical world. Finally, virtual PMM tests are not limited by the size of the body being tested due to facility constraints. A PMM test of a 1000 meter ship can be implemented as easily as a 100 meter ship ignoring possible changes in discretization requirements.

A major drawback of virtual PMM testing is that it is virtual. Virtual PMM testing does not perfectly replicate what a real model and its environment would do performing the same test. Many new errors and uncertainties are introduced, which an analyst must be aware of. These errors are best described by the following equation as was done in [16];

$$E_{sim} = E_1 + E_2 + E_3 + E_4 \tag{1.74}$$

where

$$E_1 = y_{sim} - y_{Pcomputer} \tag{1.75}$$

[10] Defining the angle of attack in this way only makes sense in the heave and sway directions.

$$E_2 = y_{Pcomputer} - y_{model}$$
$$E_3 = y_{model} - y_{exp}$$
$$E_4 = y_{exp} - y_{nature}$$

Here, y_{sim} is the computed value in the simulation, $y_{Pcomputer}$ is the value which would be computed on a perfect computer able to compute with zero round-off error, zero discretization error, and zero iterative error, y_{model} represents the exact solution to the model, y_{exp} is the value obtained from experimentation, and y_{nature} is the actual value in nature. y_{nature} is the value which both virtual PMM tests and real PMM tests attempt to measure. However, this value is never known with 100 percent certainty due to difficulties such as measurement error. Here we see that virtual PMM tests admit three new sources of error real experiments do not have: E_1, E_2, and E_3.

Despite the introduction of these error terms, PMM simulations can still account for all major aspects of the flow that would have large effects on the forces acting on the body. Often times these errors can be quantified with some certainty, giving a CFD analyst performing virtual PMM tests error bounds on the obtained solutions. Thus, virtual PMM testing can provide an accurate method of obtaining these coefficients at a greatly reduced cost when compared to similar real experiments. Virtual PMM testing in STAR-CCM+ was implemented through the use of a moving reference frame. The moving reference frame translates the entire grid through space at the applied translational and angular velocity[11]. To account for this motion, appropriate grid fluxes are added to the appropriate equations of motion corresponding to the grid's motion with respect to the lab reference frame (see (1.95)). The motion of the moving reference frame is then specified to be the perturbed motion of the body $\delta\boldsymbol{\eta}$ such that $\boldsymbol{V}_g = \delta\boldsymbol{\eta}$. More specifically, one degree of freedom of the body's velocity is specified to be perturbed by Equation (1.65). The body's velocity is then given by

$$\boldsymbol{\eta} = \boldsymbol{\eta}_0 + \delta\boldsymbol{\eta} \tag{1.76}$$

where $\boldsymbol{\eta}_0$ is specified to be the inlet velocity. All results discussed in this paper are for a body PMM tested in the heave direction such that $\boldsymbol{\eta} = [u_0, 0, \dot{\varsigma}, 0, 0, 0]^T$.

PMM tests were run for three periods. This was found to be a sufficient amount of time to allow initial transients caused by the initial conditions to damp out adequately. Parameter identification was then run for the final oscillation period so as to not contaminate the analysis with initial transients of the first two periods.

1.11 Parameter Identification

Parameter identification is the step in PMM testing where the unknown coefficients in the assumed form of the equations of motion are determined. In our state space representation, these unknown coefficients are the added mass and damping coefficients which populate the added mass and damping matrices respectively. These

[11] There are no angular velocities in the heave PMM tests discussed in this paper.

coefficients are represent oscillatory coefficients. Two simple methods referred to here as the optimization technique and Fourier decomposition are considered for determining these coefficients given the resultant force time history of a PMM test.

1.11.1 Optimization Technique

The most robust and probably the simplest to implement method of the two considered for performing parameter identification for a variety of forms of the equations of motion is numerical optimization where the objective function for PMM testing in the ς DOF can be cast as:

$$\int_{t_0}^{t_0+T} \left| \mathrm{F}_{\ddot{\varsigma}} \ddot{\varsigma} + \mathrm{F}_{\dot{\varsigma}}(\dot{\varsigma}) \dot{\varsigma} - \delta \mathrm{F} \right| dt \tag{1.77}$$

where $\mathrm{F}_{\ddot{\varsigma}}$ is the added mass coefficient and $\mathrm{F}_{\dot{\varsigma}}$ is the damping coefficient. The optimization problem is then cast as

$$\min_{\mathrm{F}_{\ddot{\varsigma}}, \mathrm{F}_{\dot{\varsigma}}} \quad \int_{t_0}^{t_0+T} \left| \mathrm{F}_{\ddot{\varsigma}} \ddot{\varsigma} + \mathrm{F}_{\dot{\varsigma}}(\dot{\varsigma}) \dot{\varsigma} - \delta \mathrm{F} \right| dt \tag{1.78}$$

where the minimization occurs over the unknown added mass and damping coefficients. Here it was assumed that the 6 states decouple giving 6 sets of independent equations. It is also assumed that the force time history is "quasi-steady," meaning that the current force only depends on the current state of the body. It means the force is assumed to not depend on what it did in the past (i.e. system has no memory). The validity of this assumption will be briefly discussed in sections 3 and 5. The final form of these objective functions depends on the form of the EOM's being considered (i.e. EOM with linear, quadratic or combined damping matrices). Real time force time histories are discontinuous, and the equivalent problem with discrete sampling in time is

$$\min_{\mathrm{F}_{\ddot{\varsigma}}, \mathrm{F}_{\dot{\varsigma}}} \sum_{i}^{N} \left| \mathrm{F}_{\ddot{\varsigma}} \ddot{\varsigma}_i + \mathrm{F}_{\dot{\varsigma}}(\dot{\varsigma}_i) \dot{\varsigma}_i - \delta \mathrm{F}_i \right| \tag{1.79}$$

where N is the number of samples in the time history data. In non-dimensional form, (1.79) becomes

$$\min_{\mathrm{F}'_{\ddot{\varsigma}'}, \mathrm{F}'_{\dot{\varsigma}'}} \sum_{i}^{N} \left| \mathrm{F}'_{\ddot{\varsigma}'} \ddot{\varsigma}'_i + \mathrm{F}'_{\dot{\varsigma}'}(\dot{\varsigma}'_i) \dot{\varsigma}'_i - \delta F'_i \right| \tag{1.80}$$

The advantage to this sort of optimization is that, at least for the drag models being considered, the problem is equivalent to solving a linear (in the parameters) regression problem. There are many optimization methods capable of solving this problem which are often easily implemented. For example, equation (1.80) can be put into the form $\boldsymbol{Ax} = \boldsymbol{b}$. This system is generally overconstrained, meaning $\boldsymbol{A}$ is full (column) rank. The unique minimum norm solution, $\boldsymbol{x}^*$, can be solved for using the pseudo-inverse of $\boldsymbol{A}$ given as

$$\boldsymbol{A}^{\dagger} = (\boldsymbol{A}^T\boldsymbol{A})^{-1}\boldsymbol{A}^T \tag{1.81}$$

such that

$$\boldsymbol{x}^* = (\boldsymbol{A}^T\boldsymbol{A})^{-1}\boldsymbol{A}^T\boldsymbol{b} \tag{1.82}$$

For the systems being considered, $\boldsymbol{A}^T\boldsymbol{A}$ will be either a 2×2 or a 3×3 non-singular matrix, which is easily inverted.

1.11.2 Fourier Decomposition

Fourier decomposition is a method that can be used to determine added mass and damping coefficients for the linear drag model where the six states are again assumed to decouple such that the EOM in each DOF becomes

$$\delta \mathrm{F} = \mathrm{F}_{\ddot{\varsigma}}\ddot{\varsigma} + \mathrm{F}_{\dot{\varsigma}}\dot{\varsigma} \tag{1.83}$$

Assuming PMM testing with oscillations of the form given by Equations (1.64)-(1.66), the EOM become

$$\begin{aligned} \delta \mathrm{F} &= a_0\omega^2 \mathrm{F}_{\ddot{\varsigma}} \cos(\omega t) + a_0\omega \mathrm{F}_{\dot{\varsigma}} \sin(\omega t) \\ &= \mathrm{F}_{\mathrm{in}} \cos(\omega t) + \mathrm{F}_{\mathrm{out}} \sin(\omega t) \end{aligned} \tag{1.84}$$

where

$$\mathrm{F}_{\mathrm{in}} = a_0\omega^2 \mathrm{F}_{\ddot{\varsigma}} \tag{1.85}$$

is the amplitude of the force F in the ς DOF in phase with the acceleration and position of the body and

$$\mathrm{F}_{\mathrm{out}} = a_0\omega \mathrm{F}_{\dot{\varsigma}} \tag{1.86}$$

is the amplitude of the force out of phase with the acceleration (and in phase with the velocity). Fourier decomposition of the force time history

$$\delta \mathrm{F} = \sum_{n=0}^{\infty} a_n \cos\frac{2\pi n t}{T} + \sum_{n=1}^{\infty} b_n \sin\frac{2\pi n t}{T} \tag{1.87}$$

where T is the characteristic period of the motion ($T = 2\pi/\omega$), breaks general periodic functions into a combination of sines and cosines at different frequencies and amplitudes. It is clear that a_0 represents the mean or DC component of the force, which is assumed to be zero[12]. With a little more work, one can show that for $n > 1$, $\{a_n, b_n\}$=0 and that

$$\mathrm{F_{in}} = \frac{1}{\mathrm{n}T}\int_{t_0}^{t_0+\mathrm{n}T} \mathrm{F}\cos\omega t\, dt \tag{1.88}$$

$$\mathrm{F_{out}} = \frac{1}{\mathrm{n}T}\int_{t_0}^{t_0+\mathrm{n}T} \mathrm{F}\sin\omega t\, dt \tag{1.89}$$

where F is the sampled signal and n is the number of periods sampled. The added mass and damping coefficients are then given simply as

$$\mathrm{F}_{\ddot{\varsigma}} = \frac{\mathrm{F_{in}}}{a_0\omega^2} \tag{1.90}$$

$$\mathrm{F}_{\dot{\varsigma}} = \frac{\mathrm{F_{out}}}{a_0\omega} \tag{1.91}$$

Expressing the force as (1.84) leads to an easy way to express how the viscous forces relate to the added mass forces through the phase shift between the motion of the body and the force applied to it. Through simple trigonometric relations, it can be shown that the phase shift Φ between the in and out of phase force components is given by

$$\Phi = \tan^{-1}\frac{\mathrm{F_{out}}}{\mathrm{F_{in}}} = \tan^{-1}\frac{\mathrm{F}_{\dot{\varsigma}}}{\mathrm{F}_{\ddot{\varsigma}}\omega} \tag{1.92}$$

If the phase shift is given in radians, the prescribed acceleration of the body leads the force response by T_{ts} seconds, where the time shift T_{ts} is given as

$$\mathrm{T}_{ts} = \frac{\Phi}{2\pi}T \tag{1.93}$$

[12] The DC component of F (if present) can be removed by subtracting out the average of F over the time interval nT.

Increasing time shifts are caused by an increasing influence of the damping coefficient relative to the added mass coefficient.

1.12 Computational Fluid Dynamics

All CFD calculations performed in this study used the commercial CFD software suite STAR-CCM+ 8.06.005 to 9.04.11 developed by CD-adapco. All simulations were run with double precision. This software was used to solve the integral form of the 3 dimensional, incompressible (constant density), continuity and momentum equations (conservation equations) for liquid water given by equations (1.94) and (1.95)[13]. These are given in conservation form, which corresponds with an Eulerian perspective of the flow[14]. Here the flow was assumed incompressible because liquid water has a very high bulk modulus (i.e. its volume changes very little with changes in pressure).

$$\rho \oiint_S (\boldsymbol{V} - \boldsymbol{V}_g) \cdot d\boldsymbol{S} = 0 \tag{1.94}$$

$$\rho \iiint_V \frac{\partial \boldsymbol{V}}{\partial t} dV + \rho \oiint_S (\boldsymbol{V} - \boldsymbol{V}_g)\left((\boldsymbol{V} - \boldsymbol{V}_g) \cdot d\boldsymbol{S}\right) = -\oiint_S p d\boldsymbol{S} + \oiint_S \boldsymbol{\tau}^T d\boldsymbol{S} \tag{1.95}$$

where

$$\boldsymbol{\tau} = \begin{bmatrix} \tau_{xx} & \tau_{xy} & \tau_{xz} \\ \tau_{yx} & \tau_{yy} & \tau_{yz} \\ \tau_{zx} & \tau_{zy} & \tau_{zz} \end{bmatrix} \tag{1.96}$$

is the deviatoric stress tensor [17]. Note that all vectors are given with respect to the inertial coordinate system. Here τ_{ij} is the stress on the i face in the j direction of a differential cube of fluid. The previous two equations provide the foundation of CFD. They are both statements of principle physics which must be obeyed. Here, equation (1.94) is a restatement of the conservation of mass (i.e. mass cannot be created or destroyed). It can be interpreted as a statement of zero divergence flow (i.e. incompressible). Equation (1.95) is a statement of the conservation of momentum (Newton's Second Law: $F = ma$).

This system is comprised of 10 independent variables (u, v, w, τ_{xx}, τ_{yy}, τ_{zz}, $\tau_{xy} = \tau_{yx}$, $\tau_{xz} = \tau_{zx}$, $\tau_{yz} = \tau_{zy}$, and p). They form a nonlinear set of partial differential

[13] See Appendix A or Appendix B for details on tensor operations.

[14] An Eulerian perspective of the flow is one where the control volumes are fixed in the coordinate system. This is the perspective most experiments are taken in, where the dependent variables such as pressure and velocity are measured at specific (stationary) points in the flow.

equations (PDE's). They are precise (not necessarily exact) statements of the physics of fluid flows. However, there is currently no known closed form solution to the full equations. Analytic solutions are only available for simple flows (e.g. coquette flow). Because of this, numerical solutions are currently the foremost method of solving[15] this system of equations. These numerical solutions include finite difference, finite volume, and finite element methods. STAR-CCM+ uses a finite volume method to discretize the equations about the cell centers of control volumes. This discretization method directly relates the conservation equations by enforcing conservation both locally at each cell, and globally over the domain. The finite volume method can be summarized as follows:

Finite Volume Method

1. Discretize the domain into a finite number of cells and assign computational nodes to each cell. In STARCCM+ the computational nodes are assigned to be the cell centers.
2. Apply conservation equations ((1.94) and (1.95)) to each cell to form a finite number of equations equivalent to the number of control volumes and unknown variables.
3. Approximate volume and surface integrals of the conservation equations using appropriate order quadrature formulas and interpolating schemes where surface integrals account for fluxes across cell faces.
4. The conservation equations with approximate integrals form a set of algebraic equations which then can be used to solve for the unknowns.
5. The algebraic equations are linearized and solved implicitly in an iterative fashion (Gauss-Seidel) using under-relaxation factors until convergence, the simulation's 'physical time' is reached, or some other criterion is met. Refer to Appendix G for more details. STARCCM+ uses an algebraic multigrid (AMG) solver to accelerate the linear solver.

To simplify the momentum equations further, Stokes' hypothesis for Newtonian fluids (e.g. water) is used, where the shear and normal stresses are assumed to be products of the velocity gradients and the dynamic viscosity[16] as shown in (1.97).

$$\text{(Viscous Stresses)} \qquad \tau_{ij} = 2\mu s_{ij} - \frac{2}{3}\mu(\cancelto{0}{\nabla \cdot \boldsymbol{V}})\delta_{ij} \tag{1.97}$$

where

$$s_{ij} = \frac{1}{2}\left(\frac{\partial V_j}{\partial x_i} + \frac{\partial V_i}{\partial x_j}\right) \tag{1.98}$$

[15] The numerical solution to the continuity and momentum equations is not necessarily equivalent to the analytic solution because the numerical solution is a discretized solution.

[16] Dynamic viscosity can safely be assumed constant, because for water it varies little over a large temperature range (and here we implicitly assume the fluid stays at a constant temperature).

is the strain rate tensor of the fluid. With this assumption, the momentum equations become the Navier-Stokes (N-S) equations. This is a significant simplification, because the equations are reduced to a function of just 4 independent variables (u, v, w and p) that can be solved for using the 4 equations given by the continuity and N-S equations. The continuity and N-S momentum equations are then solved in a decoupled fashion using the SIMPLE (Semi-Implicit Method for Pressure Linked Equations) algorithm (this is what STARCCM+'s Segregated Flow Solver performs).

In order to avoid performing full direct numerical simulations (DNS) to capture turbulent structures on the Kolmogorov length and time scales, the Shear Stress Transport (SST) k-ω turbulence model was implemented with its default settings. This turbulence model was derived for the closure of the Reynolds averaged Navier-Stokes (RANS) equations, which break the independent variables into mean and fluctuating components such that $U_i = \bar{u}_i + u_i'$, and then time averages the equations, where the time average of $f(\boldsymbol{x}, t)$ is defined as

$$F_T(\boldsymbol{x}) = \lim_{T\to\infty} \frac{1}{T} \int_t^{t+T} f(\boldsymbol{x}, t) dt \tag{1.99}$$

This averaging process introduces an additional 6 unknowns in the form of the Reynolds-stress tensor given as

$$\tau_{R,ij} = -\rho \overline{u_j' u_i'} \tag{1.100}$$

where the over bar represents a time averaged quantity. Using the Boussinesq assumption, the specific Reynolds stress tensor assumes the form

$$\tau_{R,ij} = 2\nu_T S_{ij} - \frac{2}{3} k \delta_{ij} \tag{1.101}$$

where δ_{ij} is the Kronecker delta defined in Appendix B, $k = -\overline{u_i' u_i'}$ is the specific turbulent kinetic energy, S_{ij} is the mean strain rate tensor, and ν_T is the kinematic eddy viscosity defined to be

$$\nu_T = constant \cdot k^{1/2} \ell_{turb} \tag{1.102}$$

where ℓ_{turb} is the turbulent mixing layer length. On the grounds of dimensional analysis, it is assumed

$$\ell_{turb} = constant \cdot k^{1/2} / \omega_T \tag{1.103}$$

where ω_T is the turbulent dissipation rate per unit turbulent kinetic energy. As can be seen, this turbulence model introduces two additional unknowns k and ω_T. The addition of these two unknowns requires the solution of two additional transport equations, one for each additional unknown. The form of these transport equations is given in [18]. The RANS equations and two additional transport equations become the six PDE's solved for via numerical simulations to simulate virtual PMM tests. The simulations performed in this paper are known as unsteady RANS or URANS simulations because the ensemble averaging of RANS is performed over each time step in an unsteady fashion.

1.13 Final Remarks

It is important to point out that the choice of the oscillation amplitude and frequency have a major impact on the derived added mass and damping coefficients. Increasing amplitude and frequency also increases the nonlinear aspects of the flow response by making these motions fast. The previous assumptions of linear quasi-steady flow used to derive (1.48) become less valid as a_0 and ω are increased. This result will be shown in §4.

2. Simulation Setup

The following section describes the simulation setup, including model, domain, meshing, boundary conditions, initial conditions (IC's), and virtual PMM settings.

2.1 Model: 8:1 Prolate Spheroid

An ellipsoid is a body which surface is described by

$$\frac{x^2}{a^2}+\frac{y^2}{b^2}+\frac{z^2}{c^2}=1 \tag{2.1}$$

where a, b, and c are the lengths of the semi-principle axes. When $a > b = c$, the body becomes a body of revolution about the major axis and the ellipsoid is called a prolate spheroid. Half a prolate spheroid is shown in Figure 2-1.

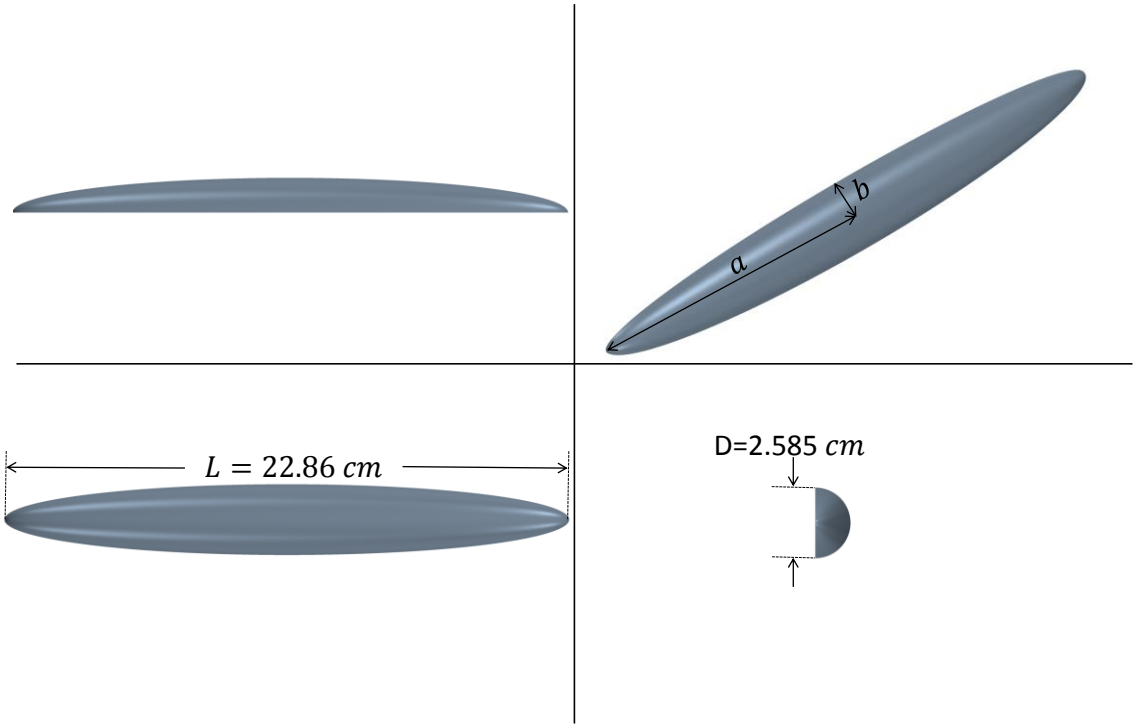

Figure 2-1: Half of a prolate spheroid model used in virtual PMM testing.

The prolate spheroid was chosen for this study because the added mass matrix can be derived analytically. The added mass coefficients for a prolate spheroid in an ideal fluid derived in [13] and given explicitly in [19] are

$$X_{\dot{u}} = -\frac{\alpha_0}{2-\alpha_0}\frac{4}{3}\pi\rho abc \tag{2.2}$$

$$Y_{\dot{v}} = -\frac{\beta_0}{2-\beta_0}\frac{4}{3}\pi\rho abc \tag{2.3}$$

$$Z_{\dot{w}} = -\frac{\gamma_0}{2-\gamma_0}\frac{4}{3}\pi\rho abc \tag{2.4}$$

$$K_{\dot{p}} = 0 \tag{2.5}$$

$$M_{\dot{q}} = -\frac{1}{5}\frac{(b^2-a^2)^2(\alpha_0-\beta_0)}{2(b^2-a^2)+(b^2+a^2)(\beta_0-\alpha_0)}\frac{4}{3}\pi\rho abc \tag{2.6}$$

$$N_{\dot{r}} = M_{\dot{q}} \tag{2.7}$$

where

$$\alpha_0 = \frac{2(1-e^2)}{e^3}\left(\frac{1}{2}\log\frac{1+e}{1-e} - e\right) \tag{2.8}$$

$$\beta_0 = \gamma_0 = \frac{1}{e^2} - \frac{1-e^2}{2e^3}\log\frac{1+e}{1-e} \tag{2.9}$$

and e is the eccentricity of the 2D ellipse given by

$$e^2 = 1 - \left(b/a\right)^2 \tag{2.10}$$

The model considered in this study was an 8:1 prolate spheroid with a length of 22.86 cm and a diameter of 2.858 cm as shown in Figure 2-1. Here the length of the spheroid is equivalent to $2a$, and the diameter is equivalent to $2b = 2c$. The model was tested at a nominal length based Reynolds number (Re_x) of 10^6. This Re_x was chosen such that the flow could be assumed turbulent over the majority of the body, corresponding to a more practical flow. Using standard pure water properties for density ($\rho = 997.561\ kg/m^3$) and dynamic viscosity ($\mu = 8.8871 \times 10^{-4}\ Pa\text{-}s$), the nominal forward speed (u_0) used was calculated to be $3.8978\ m/s$. The ellipsoid is assumed to have zero mass such that $\mathbf{M} = -\mathbf{M}_A$ and there are no resulting forces caused by gravity (e.g. buoyancy).

2.2 Domain

A cylindrical domain was used to specify the boundary conditions for the flow as shown in Figure 2-2.

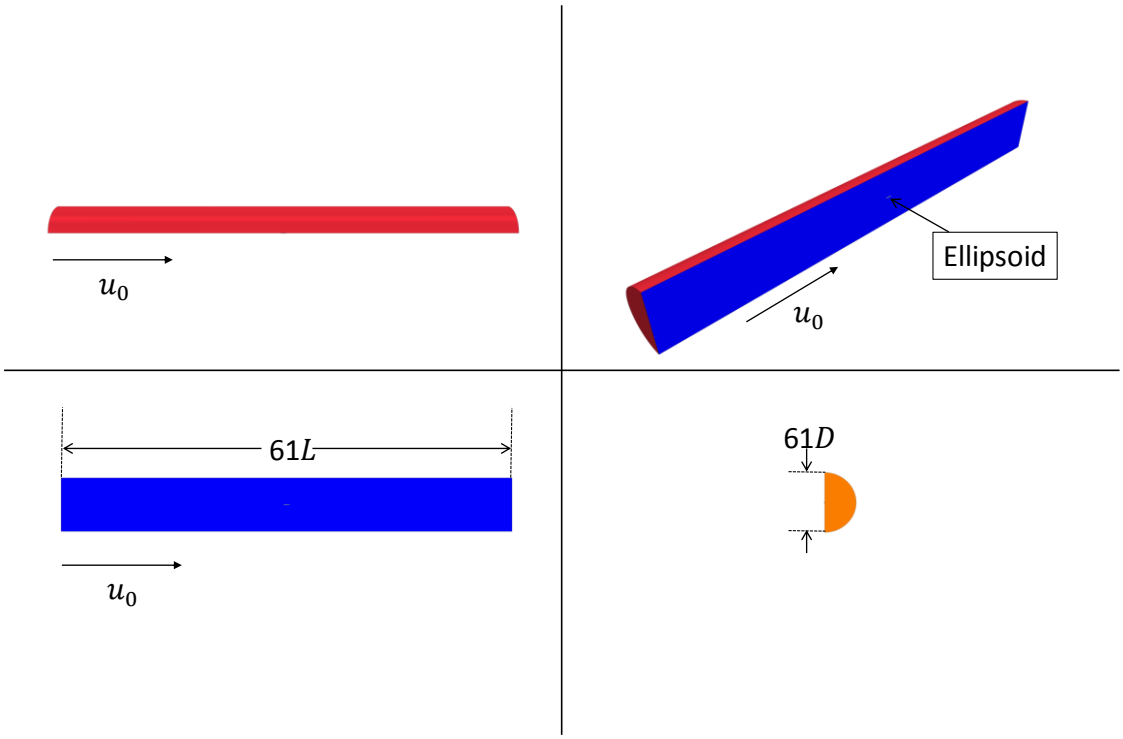

Figure 2-2: Domain used to specify BC's for simulation. Red surfaces indicate surfaces where the velocity was specified. Orange surface indicate where pressure was specified. Blue surface indicates a symmetry plane. As indicated in the figure, there are 30 body lengths upstream and downstream of the ellipsoid and 30 diameters above, below, and to the side of the ellipsoid.

All domain surfaces were placed far from the body surface such that all perturbations in the fluid due to the body could be assumed zero at the boundaries. Along the red surfaces ('velocity inlets' in STAR-CCM+), the velocity was specified to be the free stream velocity such that $\boldsymbol{V}_0 = [u_0, 0,0]^T$. It would have been ideal for the cylinder wall to be a pressure outlet instead of a velocity inlet, but this allowed the turbulent kinetic energy to be propagated through the domain in a nonphysical manner, so velocity inlets were used instead to solve this problem. The turbulence intensity

$$I = \frac{u'}{\|\boldsymbol{V}\|_2} \tag{2.11}$$

where

$$u' = \sqrt{{}^1\!/_3 \left(u_x'^2 + u_y'^2 + u_z'^2\right)} \tag{2.12}$$

and

$$\|\boldsymbol{V}\|_2 = \sqrt{\left(U_x^2 + U_y^2 + U_z^2\right)}$$

at the velocity inlet and pressure outlet boundaries were set to zero, and the turbulent length scale ℓ at these boundaries was set to $1.6\ cm$ based on a suggestion given in [20] reproduced below.

$$\ell = 0.07L \tag{2.13}$$

Note that the turbulence intensity due to the wake was assumed to damp out before reaching the domain boundaries. From this, the turbulent kinetic energy and specific turbulent dissipation can be locally calculated respectively as

$$k = \frac{3}{2} I^2 \boldsymbol{V}^T \boldsymbol{V} \tag{2.14}$$

$$\omega_T = \frac{\sqrt{k}}{\ell \beta^{*1/4}} \tag{2.15}$$

where β^* is a calibrated model coefficient.

Natural transition of the boundary layer from laminar to turbulent over a smooth flat plate with clean inlet conditions generally occurs at a Reynolds number of around 2.5×10^6. AUVs will not, in general, operate in clean conditions, and transition is assumed to occur closer to a Reynolds number of around 5.0×10^5. As can be seen in Figure 2-3, transition occurs earlier than would be expected using the Transport (SST) k-ω turbulence model with zero turbulence intensity at the boundaries.

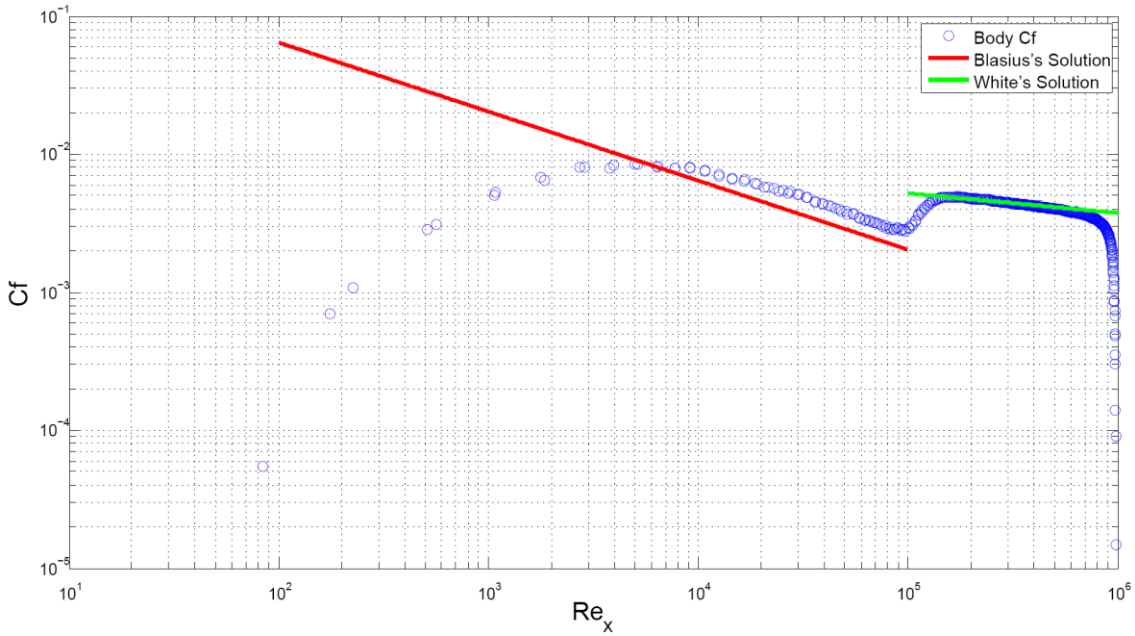

Figure 2-3: Coefficient of friction (C_f) distribution (blue circles) over surface of spheroid at $Re_x = 10^6$ from simulation at zero angle of attack. Red line is Blasius's solution for laminar flow over a flat plate derived in [21] and given as $C_f = 0.644/\sqrt{Re_x}$. Green line is an estimate of C_f for turbulent flow over a flat plate given in [22] as $C_f = 0.027/(Re_x)^{1/7}$. Both approximations come from integral analysis.

Early transition of the flow causes the flow to be turbulent over a greater portion of the model than would be expected in reality. As this is not a validation simulation, it was decided that inlet turbulence intensity was best set to zero to delay transition as long as possible. Using turbulence intensities greater than zero induced earlier transition. Along the orange surface ('pressure outlet' in STAR-CCM+),), the pressure was specified to be zero.

Large cells were able to be used far from the body where gradients in the dependent variables were small. In order to reduce the number of cells, a symmetry plane indicated by the blue surface was used because the model is symmetric about the planes of motion considered in this study. As an absurd example, if there was a fin on the port side of the ellipsoid and not on the starboard side, a symmetry plane would have been inappropriate, and the entire spheroid would have had to of been modeled.

2.3 Initial Conditions

The domain was initialized at $t_0 = 0$ with the nominal flow velocity such that

$$\boldsymbol{V}(x, y, z, t_0) = [u_0, 0, 0]^T \; \forall \; x, y, z \; \in int(Domain) \qquad (2.16)$$

where $int(Domain)$ stands for the interior of the domain and includes all the cell centers of the volume mesh not on a boundary. The pressure was initialized at a reference pressure of zero. The turbulence intensity and length scale was initialized to zero and 1.6 cm respectively throughout the domain to match the boundary conditions.

2.4 Discretization

In order to attain a numerical solution to the equations of motion (N-S Equations and 2 transport equations for k and ω_T), these equations and the domain over which they are applied must be discretized. In the finite volume method used by STAR-CCM+ for fluid flow, the domain is divided into a finite number of control volumes as described in Section 1.12. The shape of the volumes depends on the meshing model employed. Simulation in this paper used STARCCM+'s polyhedral mesher.

2.4.1 Spatial Discretization: Mesh

Except for possibly model setup, meshing is the most important aspect of the simulation setup process, requiring considerable attention in order to attain adequate results. In general a good mesh will have many cells in areas of large gradients. This is to keep the solution smooth such that large jumps and possibly large errors in the solution do not occur over adjacent cells.

The domain was meshed using STAR-CCM+'s polyhedral mesher, which creates volume cells of arbitrary shape, with an average of 14 faces per cell. Examples of the polyhedral cells used in these simulations are shown in Figure 2-4 and the mesh of the entire domain is shown in Figure 2-5.

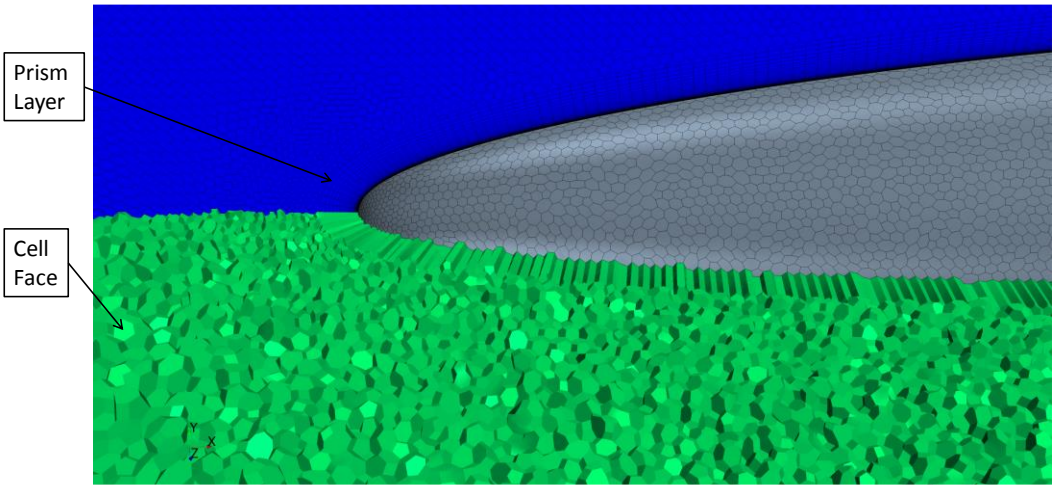

Figure 2-4: Polyhedral mesh of domain and prism layer along body.

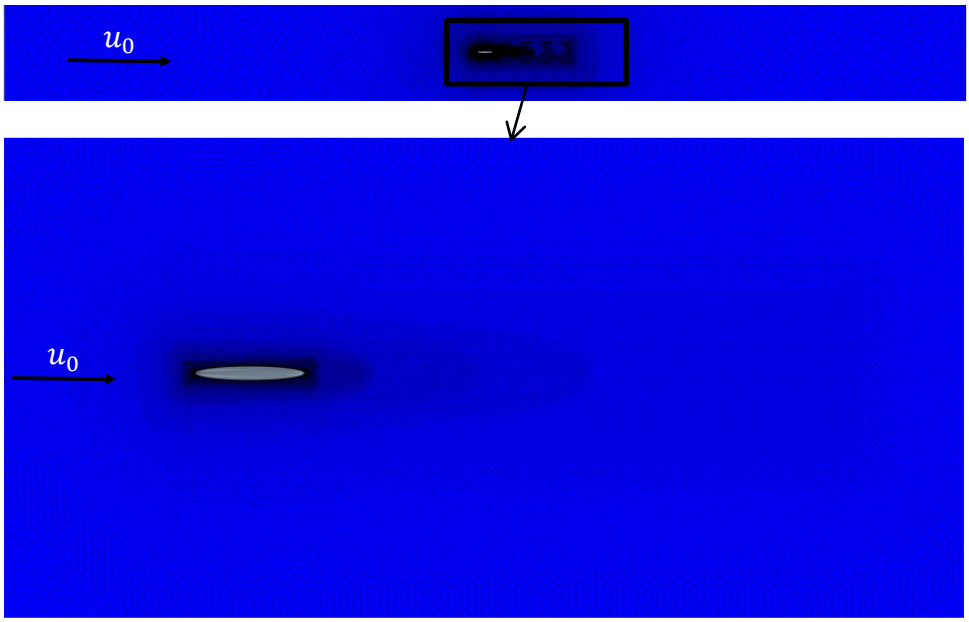

Figure 2-5: (Top) The mesh through the entire domain along the symmetry plane (blue). (Bottom) Mesh inside the box of top figure.

As can be seen, mesh density decreases rapidly as the cells move further from the body. This can be done because large gradients in the velocity profile get damped out as the fluid is advected towards the pressure outlet. Larger cells are acceptable far from the body because the boundaries are assumed to be far enough from the body that the flow near the outer boundaries is unaffected by the motion of the body and is therefore locally constant.

In the flow past a body, the largest gradients will occur in the boundary layer and wake of the flow. To capture the wake properly, 'control volumes' are used to increase the cell density where the wake will form. Increased cell density gives more cells per unit volume in the domain, leading to smaller jumps in the solution across cells. The wake control volumes used in these simulations are shown in Figure 2-6. Other control volumes not shown include a sphere centered at the nose of the ellipsoid and a large circular cylinder extending a few body lengths behind the body.

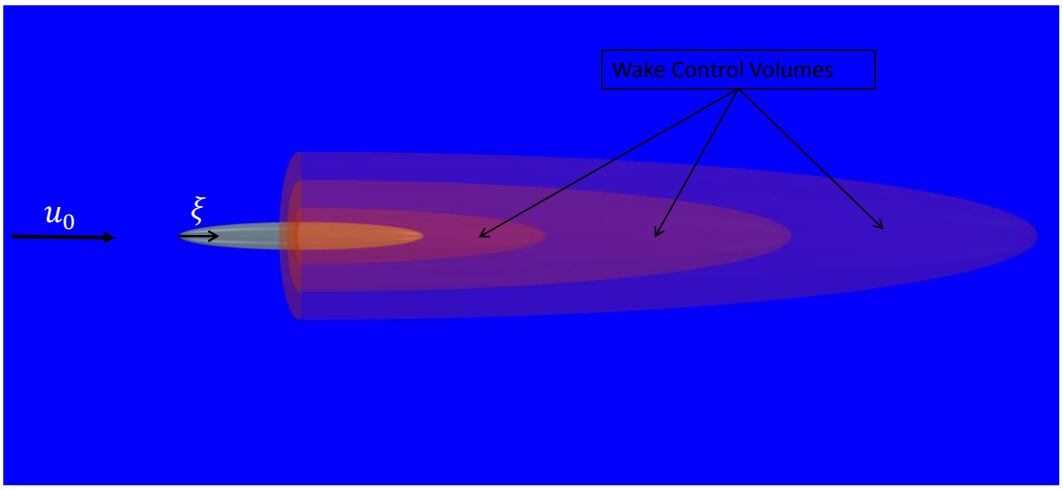

Figure 2-6: Control volumes shown in red for wake of ellipsoid. (Blue is symmetry plane)

To account for the boundary layer as best as possible, a prism layer along the surface of the ellipsoid was used, along with a boundary layer model. The maximum height of the boundary layer δ was approximated to be 0.1143 cm at the trailing edge of the body. This approximation was attained using the formula

$$\delta(\xi) = 5.0 Re_{\xi}^{-1/2} \xi \tag{2.17}$$

derived in [21] via integral boundary layer equations and experimental data, where ξ is the local coordinate system shown in Figure 2-6 and $Re_{\xi} = \frac{\rho u_0 \xi}{\mu}$. The prism layer was made to be approximately twice the predicted boundary layer thickness, spanning 45 cells, such that the height of the outermost layer was on the order of the size of the first polyhedral cells nearest the body, and the innermost layer gave $y^+ < 1$ over the entire surface of the body. This was to ensure that the viscous sublayer was being resolved such that STAR-CCM+'s All y+ boundary layer model reverts to its Low y+ wall treatment. The 45 cells are distributed with a stretch factor of 1.15, such that each layer is 1.15 times thicker than the previous layer. This prism layer stretching is done to account for the rapid change in velocity close to the surface of the body. This gives a prism layer profile similar to that shown in Figure 2-7.

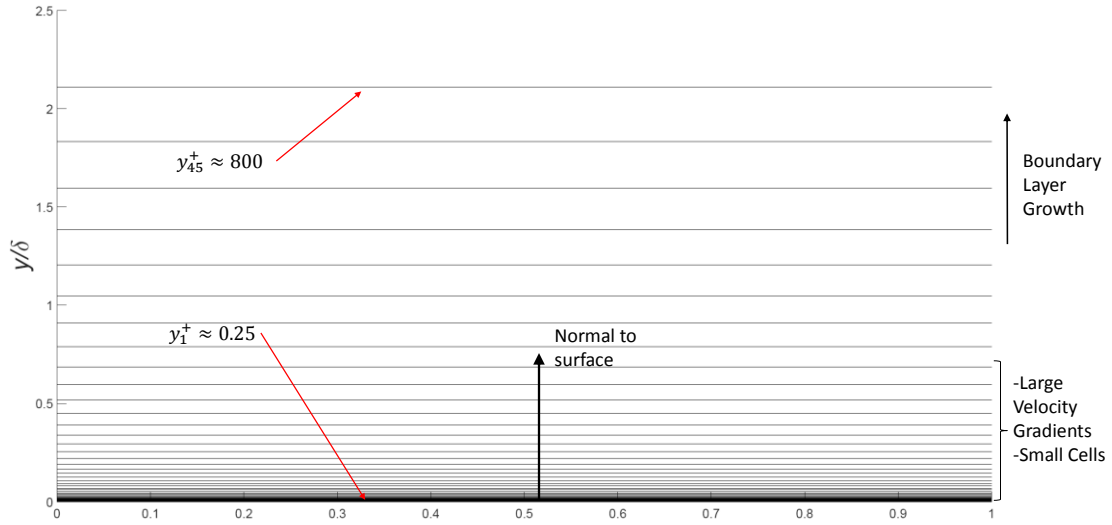

Figure 2-7: Approximate prism layer spacing shown by black horizontal lines.

The numerical algorithm used to solve the six PDE's is another crucial decision. Different schemes will provide differing degrees of accuracy, with some being more appropriate for one problem than another. All simulations presented in this paper were solved with a second order accurate upwind convection scheme (a finite differencing scheme).

2.4.2 Temporal Discretization

Time was also discretized using a second order accurate scheme. The time step used was 5e-5 seconds in order to keep the Courant-Friedrichs-Lewy (CFL) number under 1 throughout the majority of the domain where the CFL number is defined as

$$\mathrm{CFL} = \frac{\|V\|_2 \Delta t}{\Delta l} \tag{2.18}$$

where $\|V\|_2$ is the Euclidean norm of the fluid velocity at a given node, Δt is the time step, and Δl is the length of the cell in the direction of the local velocity. This number describes how far the fluid moves each time step with respect to the local cell sizes. For a $\mathrm{CFL} < 1$, the fluid moves from one cell to the next each time step, never skipping another cell. When the $\mathrm{CFL} > 1$, the fluid moves across multiple cells over a single time step. This is generally not preferred, and was only considered admissible in these simulations in areas close to the body where the cell size was very small, creating time step requirements which were too computationally expensive.

2.5 Verification and Validation

A limited number of verification and validation analyses were performed for the numerical methods employed in STAR-CCM+ to show mesh convergence. On the verification side, only an attempt to quantify spatial and temporal orders of accuracy were made to show convergence of the solution on the mesh used. On the validation side,

simulated drag was compared to experimental drag, and were shown to compare reasonably well.

2.5.1 Spatial Order Verification

When the exact solution to the differential equations is unknown the solution must be calculated on three meshes, h_1, h_2, and h_3, where each mesh is progressively coarser than the next by refinement factors

$$r_{12} = \left(\frac{N_1}{N_2}\right)^{1/d} \tag{2.19}$$

and

$$r_{23} = \left(\frac{N_2}{N_3}\right)^{1/d} \tag{2.20}$$

where N_1, N_2, and N_3 are the number of cells on the fine, medium, and coarse mesh respectively, and d is the dimension of the problem (i.e. 3 for a 3D simulation). The refinement factor is used to estimate the change in the cell sizes relative to each mesh. This version of the refinement factor was used because the mesh generated was an unstructured mesh. Each mesh level was uniformly refined[17] in STAR-CCM+ by referencing all cell sizes to the base size, and then reducing the base size by a factor of 1.5 for each mesh level. Round off error was assumed negligible because the simulation was run with double precision, and iterative error was assumed negligible because residuals[18] were allowed to drop at least 5[19] orders of magnitude until becoming relatively constant with increasing iterations. Finally, because temporal discretization was unimportant, the simulations were run with STAR-CCM+'s steady solver, which takes local time steps throughout the domain.

The drag coefficient

$$C_D = \frac{D}{1/2\,\rho u_0^2 S} \tag{2.21}$$

where D is the drag on the spheroid and $S = \pi b^2$ is the frontal surface area of the spheroid, was the system response quantity (SQR) for which the observed order of accuracy $\hat{p}$ was derived. One can solve for $\hat{p}$ by solving,

[17] The prism layer was not refined when progressively refining the grid. It is hoped that this does not introduce major errors.
[18] Residuals measure the degree to which the solution variables satisfy the equations of motion at each iteration.
[19] Most residuals dropped at least 8 orders of magnitude.

$$\hat{p}^{k+1} = \frac{\ln\left[\left(r_{12}^{\hat{p}^k} - 1\right)\left(\frac{f_3 - f_2}{f_2 - f_1}\right) + r_{12}^{\hat{p}^k}\right]}{\ln(r_{12} r_{23})} \tag{2.22}$$

given in [16], iteratively, where f_i is the SRQ at mesh level i, and the formal order of accuracy of the discretization scheme is used as an initial guess of $\hat{p}$.

The results of the simulations are summarized in Table 2-1. The observed order of accuracy was calculated to be 1.6786, which is slightly less than the formal order of accuracy of 2. One cause of this disagreement may be that the refining method used is not perfectly uniform. However, the results do indicate overall convergence of the solution at a higher than linear rate. The order also indicates that we are close to the asymptotic range, where the higher order terms in the discretization scheme can be safely neglected.

Table 2-1: Mesh level characteristics (drag) giving an observed order of accuracy of 1.6786.

Mesh Level	Number of Cells	C_D
h_1	7,061,591	0.1127
h_2	2,930,118	0.1130
h_3	1,375,610	0.1134

2.5.2 Temporal Order Verification

The temporal order of accuracy was estimated with a very similar approach. However, instead of refining the mesh, the time step Δt_i was refined by a factor $r_t = 2$ over 5 simulations such that the time steps on the temporal meshes are given by

$$\Delta t_5 = \Delta t_2 r_t = \Delta t_3 r_t^2 = \Delta t_2 r_t^3 = \Delta t_1 r_t^4 \tag{2.23}$$

where $\Delta t_5 = 4 \times 10^{-4}$.

In order to assess the temporal order, a time dependent solution is needed. A PMM test over a small portion of the period with $a_0' = 0.2$ and $f' = 0.2$ was used on mesh h_1, the finest mesh in §2.4.2, to reduce the effects of discretization errors. All simulations were initialized with the converged steady state solution and were run for the initial 0.01 seconds of the PMM test (100 iterations on Δt_3). Each iteration was allowed to fully converge by enforcing 500 inner iterations between time steps, diminishing the effect of iterative errors.

Evaluating the temporal convergence can be a very tricky matter. There are multiple ways to assess convergence. The problem is, depending on which method is employed, different conclusions may erroneously be drawn. Three methods will be presented here in the hopes of illuminating this problem. The first method is to simply evaluate the observed order at each coincident[20] time step of each temporal mesh where the observed order can now simply be calculated, as given in [16], as

[20] Coincident time steps are time steps which all simulations have in common.

$$\hat{p} = \frac{\ln\left(\frac{f_{i+2} - f_{i+1}}{f_{i+1} - f_i}\right)}{\ln(r_t)} \tag{2.24}$$

because the refinement through time (r_t) was constant. Note that here the index i in f_i represents the temporal coarseness. Results are shown in Figure 2-8 for various combinations of simulations. Depending on choice of mesh level and time to evaluate $\hat{p}$ one can reach a variety of conclusions on the temporal order of accuracy. Using the finest 3 temporal simulations (Figure 2-8 (a)), it appears that we initially have a temporal observed order of 2. The order diminishes through time, eventually becoming negative, reaching a minimum and then rising again. Negative order indicates that the difference between solutions is *increasing* with temporal refinement. This could indicate that the solution is not in the asymptotic range. Comparing this with the observed order of the 3 coarsest meshes (Figure 2-8 (c)), an entirely different picture of how the solution is converging is seen. Here the order starts very low, and tends to increase through time, reaching values indicative of convergence at a rate higher than the formal order. This method did not lead to any clear results. To avoid the problem of deciding where to evaluate $\hat{p}$, the Euclidean norm of the nondimensional drag force was used in the second method to calculate f_i given as

$$f_i = \left(\sum_{n=1}^{N} (\mathrm{X}'^{,n})^2\right)^{1/2} \tag{2.25}$$

where n is the time step beginning from the initial condition ($n = 1$). Equation (2.24) was then used with this f_i on the various temporal meshes given in Table 2-2. The calculated orders of accuracy are summarized in Table 2-3.

(a) (b)

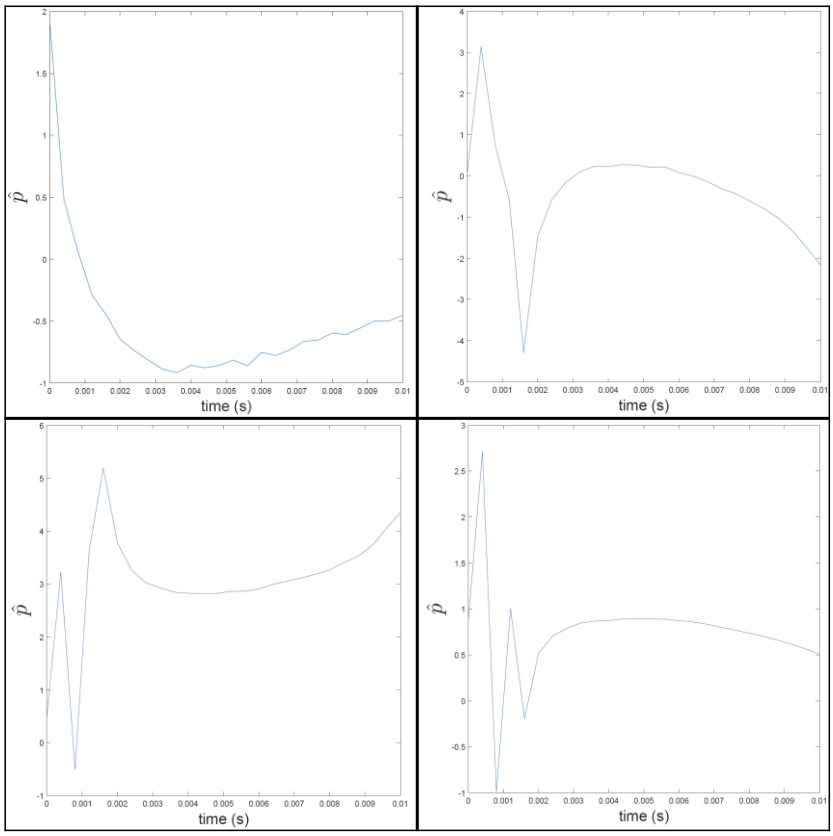

(c) (d)

Figure 2-8: Calculated order of accuracy over first 0.01 seconds of PMM test. (a) $\hat{\boldsymbol{p}}$ for girds 1, 2 and 3. (b) $\hat{\boldsymbol{p}}$ for girds 2, 3 and 4. (c) $\hat{\boldsymbol{p}}$ for girds 3, 4 and 5. (d) $\hat{\boldsymbol{p}}$ for girds 1, 3 and 5 with $\boldsymbol{r_t} = \mathbf{4}$. (Note: imaginary parts ignored).

Table 2-2: Temporal level characteristics (drag).

Temporal Levels	Time Step (Δt_i)	f_i
Δt_1	2.5e-5	4.967909
Δt_2	5.0e-5	4.967872
Δt_3	1.0e-4	4.967847
Δt_4	2.0e-4	4.967884
Δt_5	4.0e-4	4.967781

Table 2-3: Temporal observed order using different combinations of mesh levels.

Meshes Used	$\hat{p}$
$\Delta t_3, \Delta t_4, \Delta t_5$	1.5062 + 4.5324i
$\Delta t_2, \Delta t_3, \Delta t_4$	0.5387 + 4.5324i
$\Delta t_1, \Delta t_2, \Delta t_3$	-0.5482
$\Delta t_1, \Delta t_3, \Delta t_5$	0.0594

This method also leads to inconclusive results. Imaginary terms are usually caused by oscillatory convergence, where the solution oscillates about its true value as the mesh is refined.

The final and most illuminating method employed was as follows. The solution of the finest mesh was assumed to be the exact solution. The absolute value of the error of the solutions on the four coarser meshes were then calculated. This error was then plotted for each temporal level through time creating a 2D error surface, shown in Figure 2-9.

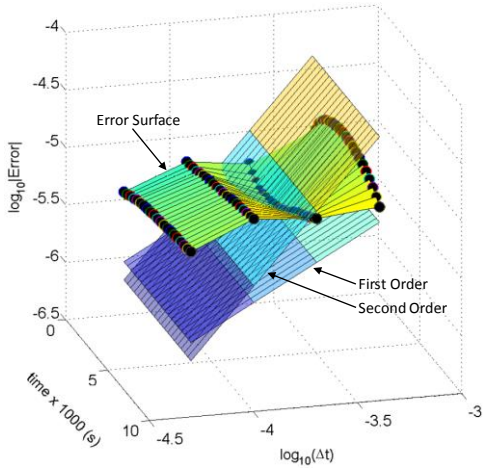

Figure 2-9: Error surface showing less than first order error convergence.

The error surface shows how temporal refinement changes the solution relative to the finest mesh solution. Ideally, the exact solution to the equations being solved would be used as the reference, but this is unknown. If it were known we would not need to perform these numerical simulations. The error surface suggests that the solution is converging, but at a lower than first order rate. This was unexpected because the formal temporal order is second order. The cause of this was not pursued any further because the error surface shows the solution converging with temporal refinement.

2.5.3 Drag Validation

Due to the lack of real PMM experiments on 8:1 spheroids, only the steady state drag coefficient of the spheroid was used to give some authority to the results obtained. In [23], the drag coefficient over an 8:1 spheroid with a tripped boundary layer at $Re = 10^6$ was measured to be 0.114. There is less than a 2% error as compared to the drag coefficient obtained numerically on the finest mesh of the preceding mesh study. This error is partly due to the many unknowns involved in the actual experimental setup, such as inlet turbulence conditions and surface roughness. The fact that the flow was tripped in the experiment was hoped to bring the simulations results into more alignment with the experimental results since the $k - \omega$ turbulence model is known to transition early. Because of this, one may tend to consider this validation experiment as more of a calibration. Clearly more extensive validation is needed, especially for the time dependent aspects of the PMM test.

2.6 PMM Summary

The procedure for PMM testing of AUV's (or any body immersed in a fluid) can be summarized as follows:

1. Determine PMM requirements such as desired accuracy, turnaround time, etc.
2. Generate mesh for CFD simulation as required by step 1.
3. Set up necessary physics as required by step 1.
4. Determine and enforce necessary initial and boundary conditions.
5. Virtually perform PMM test of AUV in all 6 DOF.
6. Determine model coefficients via parameter identification.

Once parameters have been determined, the model is fully characterized for a given operating condition. As was said at the very beginning, the three models considered in this paper have their limitations. These limitations will be shown for virtual PMM testing of the spheroid being considered in heave. The results can easily be extended to general bodies in all DOF by performing the PMM test in different DOF's.

3. Flow Analysis of 8:1 Spheroid

Before discussion of how well the models performed for the various PMM tests, it is helpful to have a more basic understanding of the flow around a prolate spheroid. This will be done in three stages. First an analysis of a spheroid at various steady angles of attack will be included to discuss various flow features. These flow features are observed in the unsteady PMM tests; however, care must be taken when comparing these steady features, to the unsteady features seen in PMM tests as they are not exactly the same. All angles of attack are purely in the x-z plane. Second, a short discussion on the behavior of the wake as a spheroid quickly stops at the apex or trough of its maneuver. Thirdly, these two stages will be brought together to discuss the flow features seen in a full PMM test.

3.1 Steady Analysis at Various Angles of Attack

The flow features discussed in this section will be based on the flow topology over the surface of the spheroid at steady angles of attack and Reynolds number of 10^6. Appendix H gives a brief overview of typical flow topology encountered in this study. It contains a topological description of nodes of attachment and separation, foci of attachment and separation, saddles of attachment and separation, and cross flow separation. These descriptions are based on phase plane analysis of vector fields, and are used here mostly as a heuristic means of describing the flow. The images shown use STARCCM+'s "line convolution integral," which takes the shear stress vector field, computes streamlines from the stress vector fields, and then convolves a white noise image along the streamlines to create a texture based image. These lines are called skin friction lines because they are derived from the shear stress vector field. The flow topology agrees fairly well qualitatively with experiments described in [11], where topological flow analysis was performed on 2:1 and 4:1 spheroids at Reynolds numbers between 7 and 14×10^4. The spheroid under investigation is twice as long as the 4:1 spheroid and at a much higher Reynolds number so direct comparisons are impossible. However, similar flow features such as lines of separation, saddles, and focuses seen in the experiments are seen in the present simulations giving them greater credibility.

All images use the "Jet" color map, which uses blue to represent low values and red to represent high values. Values scale linearly between low and high values. Refer to Figure 3-1 for reference.

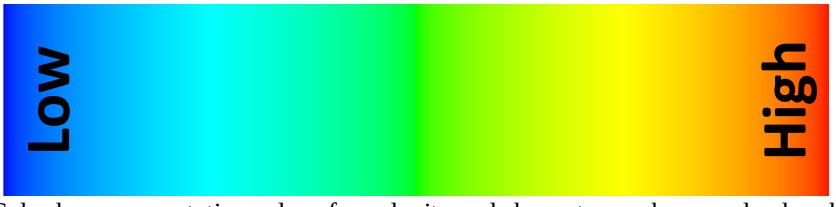

Figure 3-1: Color bar representative values for velocity and shear stress where cool colors like blue represent relatively smaller values than hotter colors like red.

3.1.1 $\alpha = 0°$

At $\alpha = 0°$, the flow is well behaved as shown in Figure 3-2. The skin friction lines start at the nose, where the fluid attaches to the body at an attachment node (N_{A1}), travels from the nose of the spheroid towards the tail, and does not separate until approximately 98% of the body has been covered. Here, a line of separation (L_1) emerges, at which point the flow separates, forming a toroidal vortex at the tail end of the spheroid. This vortex creates a reattachment node (N_{A2}) at the tail end of the spheroid, where the flow reattaches to the body and travels back towards the line of separation, where it again separates.

The line of separation occurs much further back on the body than that seen in Figure 6a of [11]. This is attributed to the blunter body and lower Reynolds number of the experiment leading to a stronger adverse pressure gradient and possibly lower turbulence in the boundary layer than in the present simulation.

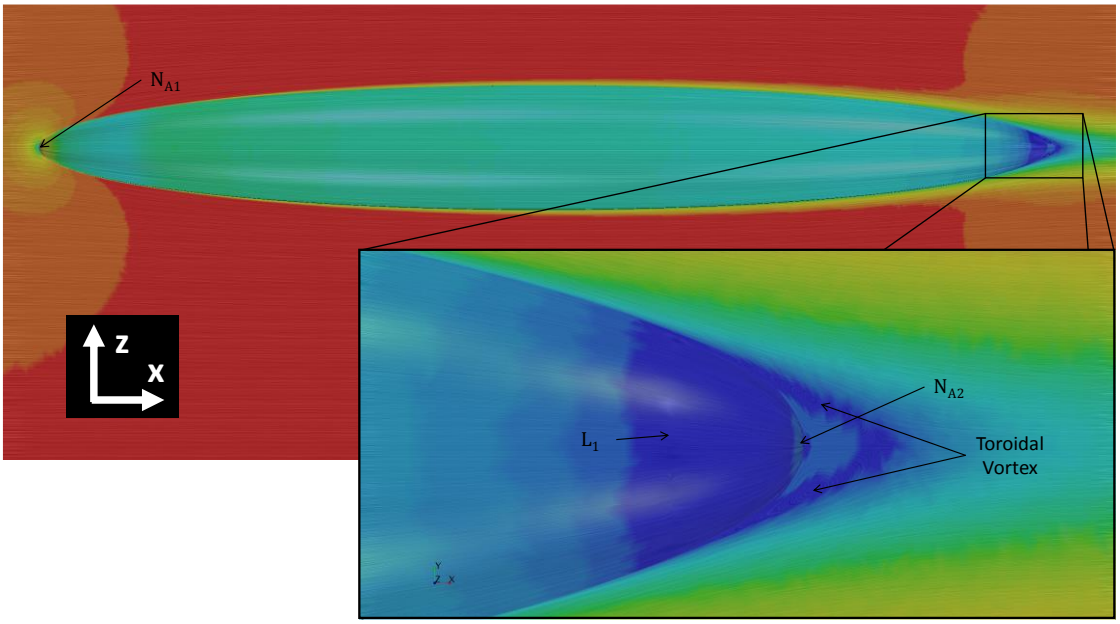

Figure 3-2: Flow over spheroid at $\boldsymbol{\alpha = 0°}$. In all similar figures below, streamlines on the symmetry plane were derived from the velocity vector field and skin friction lines on the surface of the spheroid were derived from the shear stress vector field. (For reference: $\|\boldsymbol{v}\| \boldsymbol{\epsilon}\ [\mathbf{0.0001}, \mathbf{4.0032}]$ m/s and $\boldsymbol{\tau_w}\ \boldsymbol{\epsilon}\ [\mathbf{0.0634}, \mathbf{99.3107}]$ Pa).

3.1.2 $\alpha = 2°$

A small change in the angle of attack, from $\alpha = 0°$ to $\alpha = 2°$, leads to a fairly drastic change in the flow topology towards the tail portion of the spheroid, as shown in Figure 3-3.

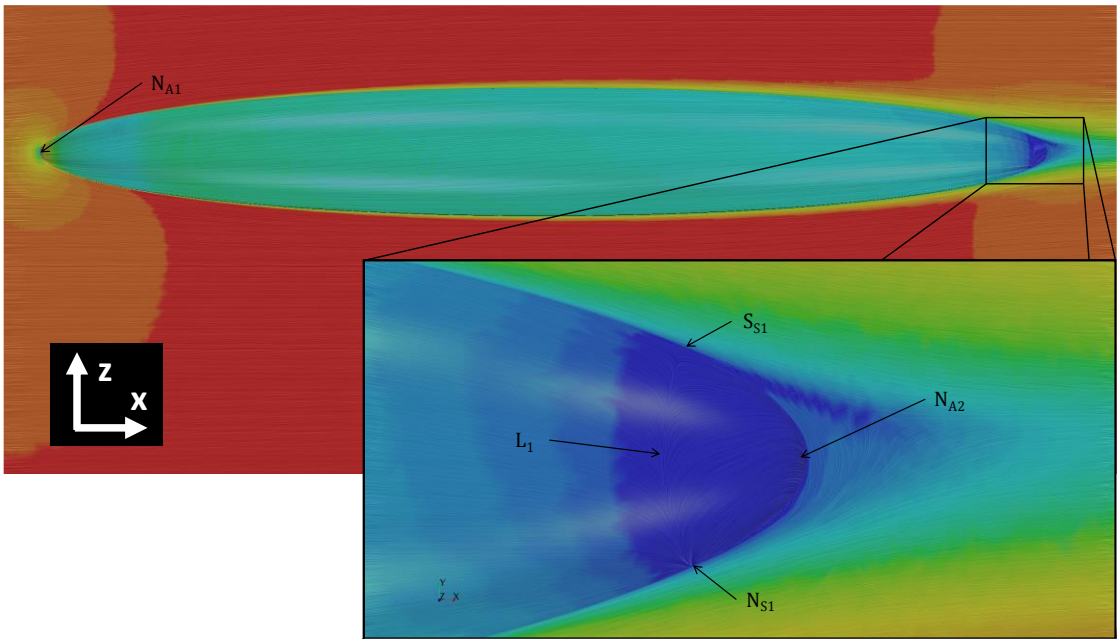

Figure **3-3:** Flow over spheroid at $\boldsymbol{\alpha = 2°}$. (For reference: $\|\boldsymbol{v}\|$ $\boldsymbol{\epsilon}$ $[\mathbf{0.0000}, \mathbf{4.0136}]$ m/s and $\boldsymbol{\tau_w}$ $\boldsymbol{\epsilon}$ $[\mathbf{0.1146}, \mathbf{103.6592}]$ Pa).

The flow attaches at node of attachment (N_{A1}) and travels down the body at a slight angle of attack before reaching the line of separation (L_1). At this point, the flow turns down and continues to travel along L_1 until separating at a node of separation (N_{S1}). Some separated flow reattaches at the tail end of the spheroid at N_{A2}, attaching then traveling up the body towards L_1. However, instead of traveling straight as it did at zero angle of attack, the flow diverges downward, similar to how it diverged downward on the other side of L_1. This line of separation is due in part to the saddle of separation S_{S1} which formed towards the top of the trailing edge.

3.1.3 $\alpha = 4°$

At $\alpha = 4°$, the flow once again changes fairly drastically. The saddle point S_{S1} has moved towards the center of the spheroid. Also, a tornado-like vortex begins to form on the bottom rear of the spheroid, spawning from a focus of separation (F_{s1}). This focus is believed to be formed by the separation surface, spawning from L_1, rolling up as shown in Figure H-4 of Appendix H. The node of attachment N_{A2} remains at the rear similar to how it appeared at $\alpha = 2°$, but S_{S1} diverges some flow up to a new node of separation N_{S2}. N_S and S_S also appear on the bottom of the spheroid, but are non-dominant features. Non-dominant in the sense that they do not look as if they have a large impact on the flow.

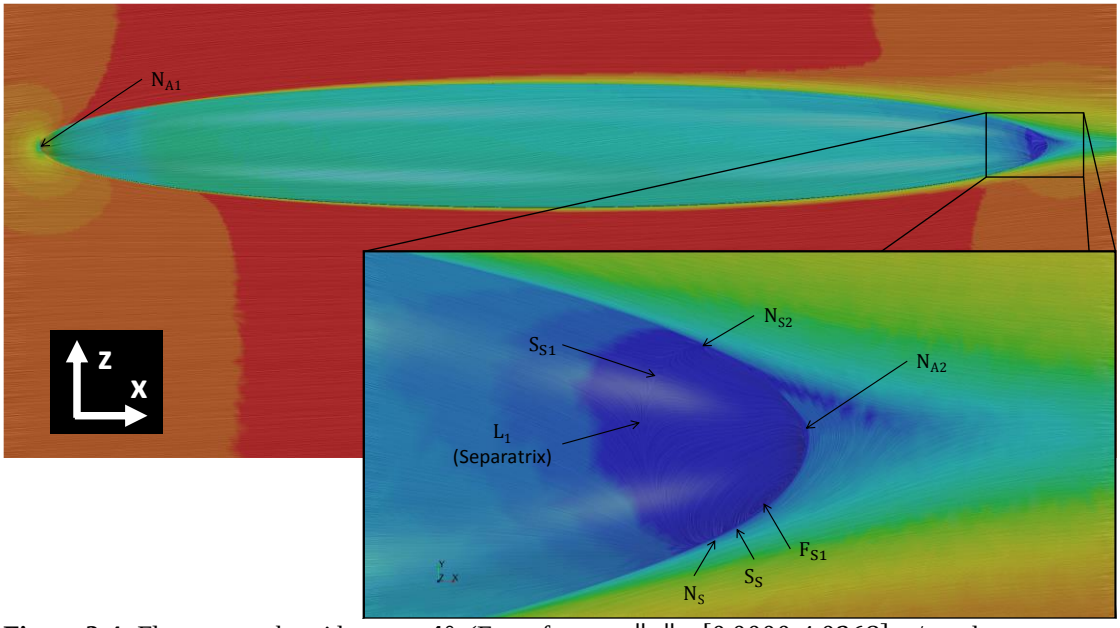

Figure 3-4: Flow over spheroid at $\boldsymbol{\alpha = 4°}$. (For reference: $\|v\| \in [0.0000, 4.0368]$ m/s and $\tau_w \in [0.0668, 111.0383]$ Pa).

3.1.4 $\alpha = 7°$

At $\alpha = 7°$, another tornado-like vortex forms, spawning from F_{S2}. It is thought that due to the symmetry of the problem, the tornado like vortices spawning from F_{S1} and F_{S2} form symmetrically on the other side of the symmetry plane and join at V_1 and V_2 respectively. The vortex structure V_1 is the cause of the surface topology at the aft tip of the spheroid where N_{A2} and S_s' are formed. Two saddles of separation labeled as S_S and split by the symmetry plane, also form due to the formation of F_{S1} and F_{S2}. The non-dominant features N_S and S_S at $\alpha = 4°$, have disappeared.

At $\alpha = 7°$, crossflow separation begins to become apparent, being revealed by local minima in the skin friction coefficient and the convergence of skin friction lines on the side of the body to the line of crossflow separation (CF_{S1}). This type of separation is often referred to as primary separation, as it is the point where the flow first separates from the body. Some of the separated flow reattaches along a line of attachment (CF_{A1}). at the symmetry plane. Because this type of separation does not have a well defined instantiation point, it is hard to define at what exact angle cross flow separation begins. Increasing angle of attack makes this type of separation clearer and more severe.

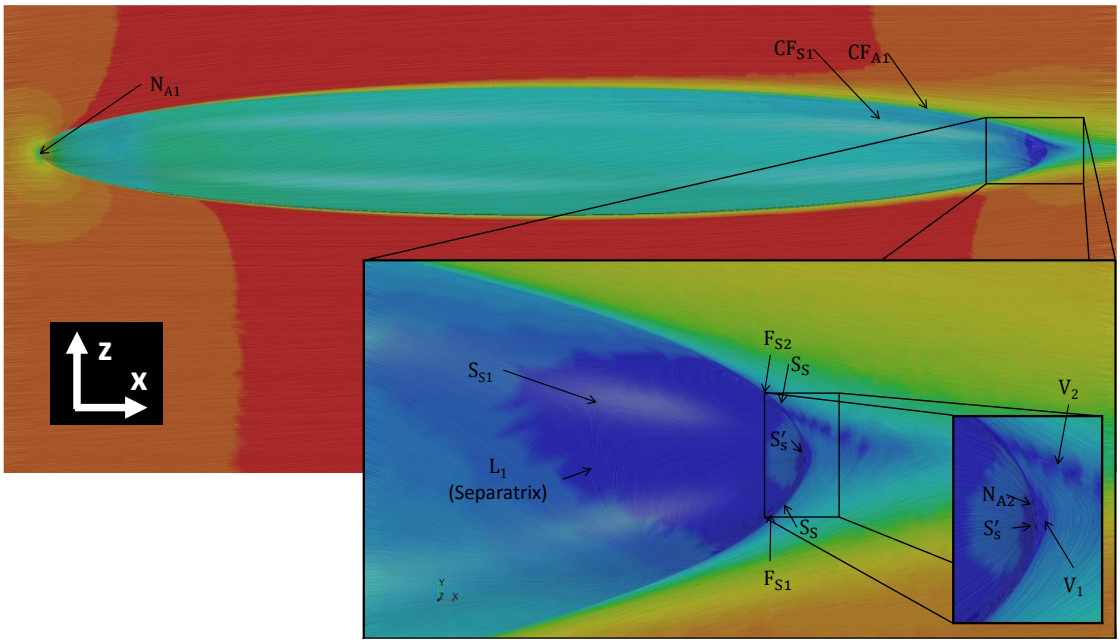

Figure 3-5: Flow over spheroid at $\boldsymbol{\alpha = 7°}$. (For reference: $\|\boldsymbol{v}\| \boldsymbol{\epsilon}\ [\mathbf{0.0000}, \mathbf{4.3940}]$ m/s and $\boldsymbol{\tau_w \epsilon}\ [\mathbf{0.3728}, \mathbf{150.4514}]$ Pa).

3.1.5 $\alpha = 10°$

By $\alpha = 10°$, the flow is clearly crossflow separating along a single line of separation, as shown in Figure 3-6 and indicated by CF_{S1}. Most flow features are very similar to those seen at $\alpha = 7°$ with a couple changes. The foci F_{S1} moves upstream towards the nose of the spheroid, positioning itself directly below F_{S2}. This is what causes the vortex structures V_1 and V_2 to stack symmetrically about the x-z plane in the wake, giving a similar velocity portrait to that seen at $\alpha = 0°$ at the tail end of the spheroid.

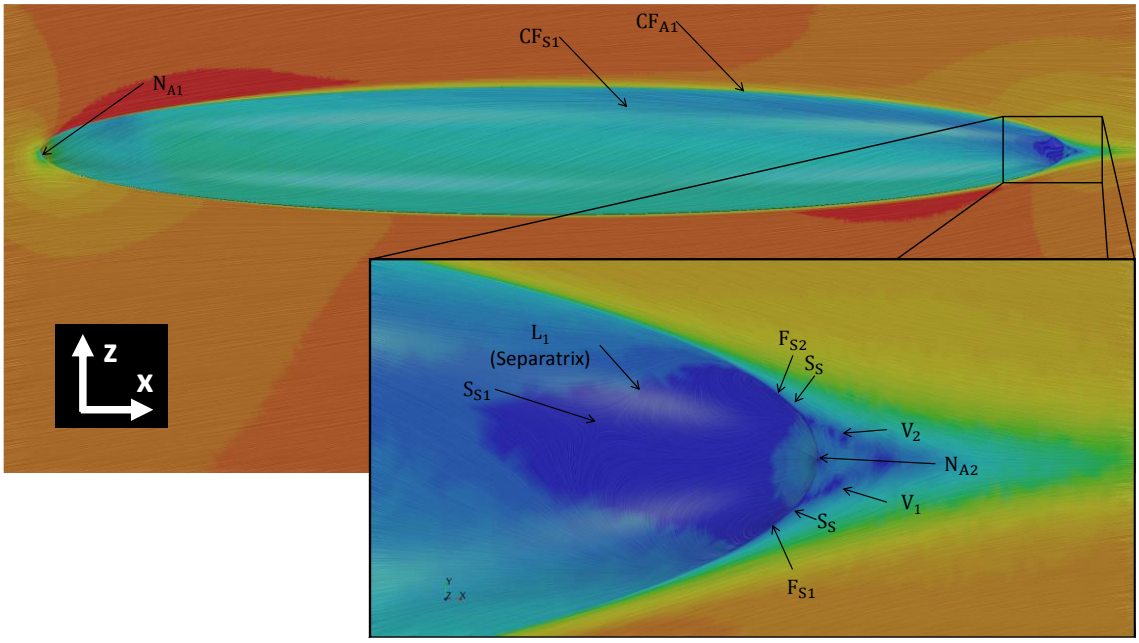

Figure **3-6:** Flow over spheroid at $\boldsymbol{\alpha = 10°}$. (For reference: $\|\boldsymbol{v}\| \boldsymbol{\epsilon}\ [\mathbf{0.0002, 4.1091}]$ m/s and $\boldsymbol{\tau_w}\ \boldsymbol{\epsilon}\ [\mathbf{0.2228, 122.0017}]$ Pa).

3.1.6 $\alpha = 14°$

When an angle of attack of 14 degrees is reached, secondary cross flow separation starts to emerge. This event is accompanied by the emergence of another saddle of separation (S_{S2}) and focus of separation (F_{S3}), which seem to spawn from one another. The lines of separation L_1 and L_2 which form due to the saddles of separation S_{S1} and S_{S2} form an almost curly separation line. The focus F_{S1} morphs into a structure similar to a node of separation and is labeled as N_{S3}. Despite the disappearance of F_{S1}, the vortical structure V_1 remains and begins to squeeze against the tail of the spheroid, while V_2 gets stretched as it moves further from the body. This movement corresponds with the focus F_{S2} moving towards the nose of the body. The nodes of attachment do not change position to much as compared to $\alpha = 10°$.

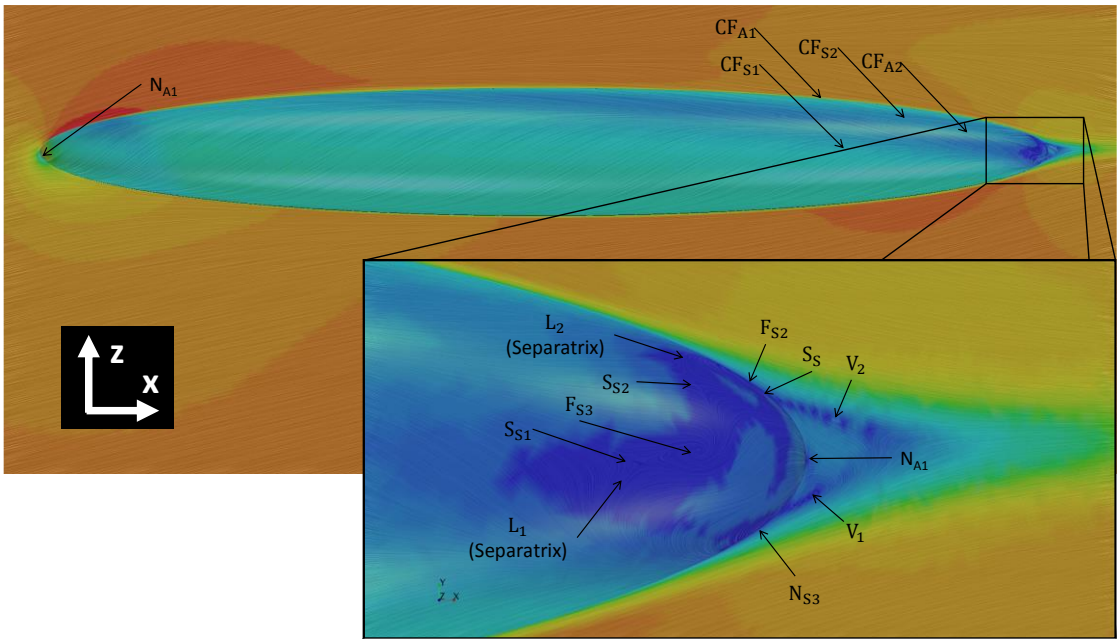

Figure **3-7:** Flow over spheroid at $\boldsymbol{\alpha = 14°}$. (For reference: $\|\boldsymbol{v}\| \boldsymbol{\epsilon}\ [\mathbf{0.0000}, \mathbf{4.3940}]$ m/s and $\boldsymbol{\tau_w}\ \boldsymbol{\epsilon}\ [\mathbf{0.2228}, \mathbf{122.0017}]$ Pa).

3.1.7 $\alpha = 20°$

At $\alpha = 20°$, the secondary crossflow separation becomes clear. The saddle S_{S1} and focus F_{S3} disappear, leaving only S_{S2}. However, even with only this saddle, the line of separation remains fairly curly. The vortical structures seen at $\alpha = 10°$ have been completely washed out, despite the persistency of F_{S2}. The node of attachment N_{A1} is starting to move down and towards the tail, while the node of reattachment N_{A2} remains at about the middle of the body as with the previous angles of attack.

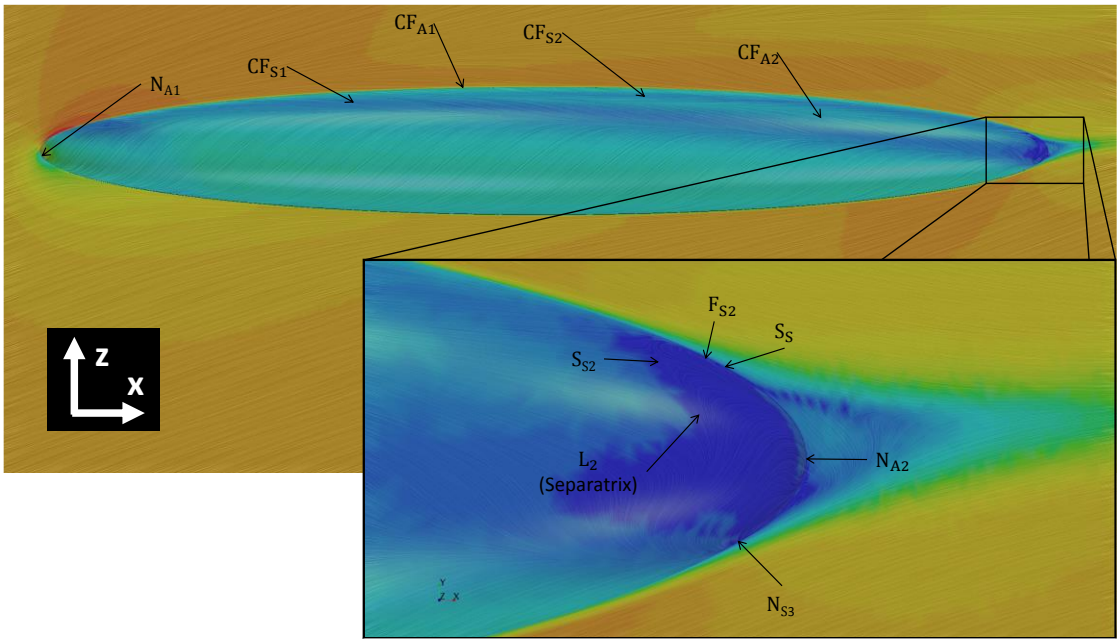

Figure 3-8: Flow over spheroid at $\boldsymbol{\alpha = 20°}$. (For reference: $\|\boldsymbol{v}\|$ $\boldsymbol{\epsilon}$ $[\mathbf{0.0004}, \mathbf{4.7989}]$ m/s and $\boldsymbol{\tau_w}$ $\boldsymbol{\epsilon}$ $[\mathbf{1.1201}, \mathbf{183.8327}]$ Pa).

3.1.8 $\alpha = 30°$

At $\alpha = 30°$, as shown in Figure 3-9, the secondary separation line is clearly visible. The surface topology is similar to that of the spheroid at $\alpha = 20°$, but a saddle, S_{S3}, and a focus, F_{S4}, form together. It is at this point we note that saddles often form with foci. Up to this point we have seen saddles with no associated foci as in the flow at $\alpha = 2°$ and 4°, but never a foci with no saddle. This is because the foci are often formed by the separating surface rolling up as explain in Appendix H. The vortex structure V_1 (believed to be create by F_{S4}) has been almost entirely squished against the surface, and V_2 has become indiscernible in the symmetry plane despite the continued existence of F_{S2}. The node of attachment N_{A2} has moved slightly more down and towards the tail of the spheroid, while the node of reattachment still remains around the middle of the tail at the aft end of the body.

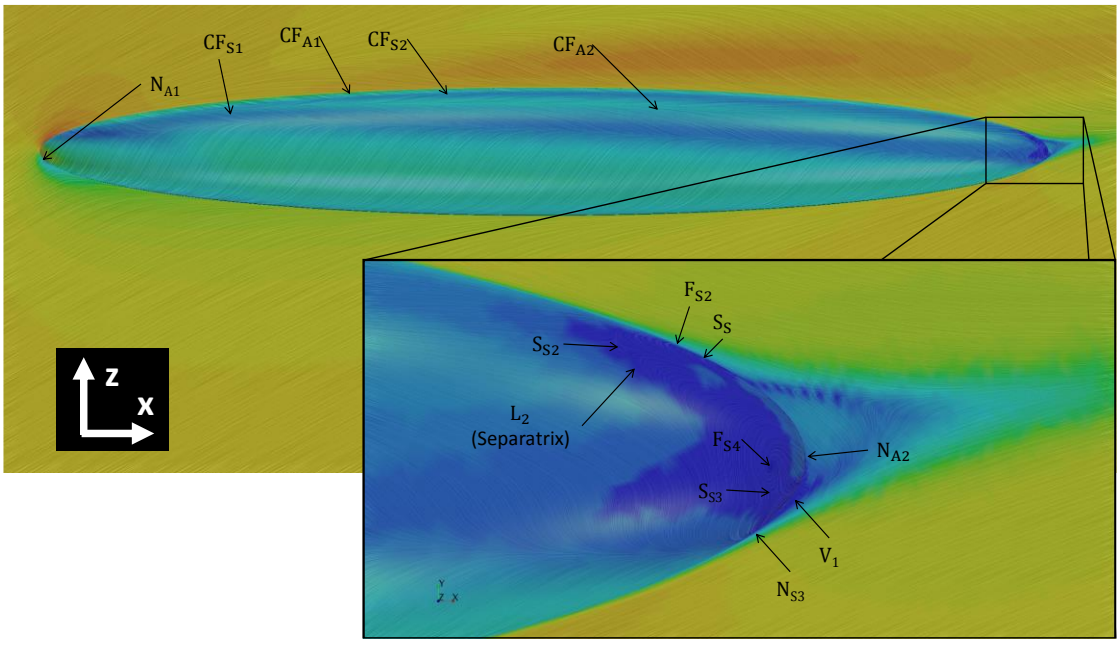

Figure **3-9:** Flow over spheroid at $\boldsymbol{\alpha = 30°}$. (For reference: $\boldsymbol{\|v\| \epsilon [0.0007, 5.8132]}$ m/s and $\boldsymbol{\tau_w \epsilon [0.3974, 260.1299]}$ Pa).

3.1.9 $\alpha = 60°$

Finally, the spheroid at $\alpha = 60°$ is discussed as this is near the maximum angle of attack the spheroid attains during all the PMM tests. As can be seen in Figure 3-10, the spheroid does not develop any additional (at least clearly defined) lines of crossflow separation. At this high angle of attack, the separation lines are more aligned with the horizontal axis (x-axis) than the vertical axis (z-axis), which is of no surprise given the spheroid is now traveling vertically faster than it is horizontally. Flow at the nose of the spheroid actually travels up along the x-axis before rounding the nose and traveling down the body. Comparing the flow features at the aft end of the vehicle to those at $\alpha = 30°$, F_{S4} and S_{S3} have both been washed out. The vortical structure V_1 disappears with the vanishing of F_{S4}. The vortical structure V_2, however, becomes clear once again at this angle of attack. The node of attachment N_{A1} has moved very far down and towards the nose, and the node of reattachment N_{A2} has moved up the aft end and slightly towards the nose due to the extreme angle of attack of the flow.

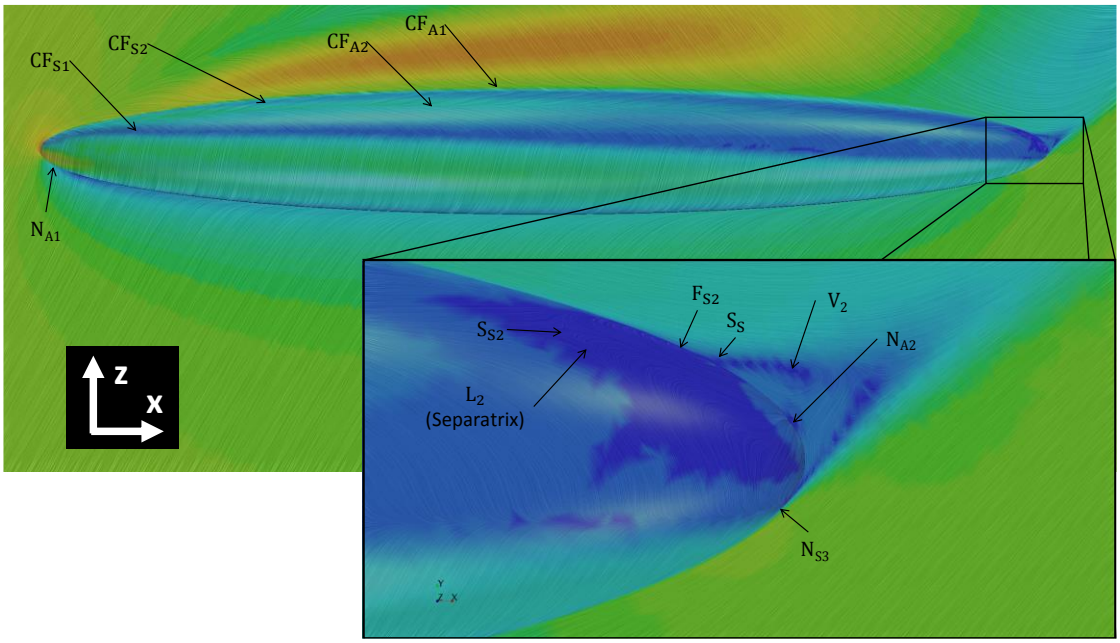

Figure **3-10:** Flow over spheroid at $\boldsymbol{\alpha = 60°}$. (For reference: $\|\boldsymbol{v}\| \boldsymbol{\epsilon}\ [\mathbf{0.0021}, \mathbf{13.3963}]$ m/s and $\boldsymbol{\tau_w}\ \boldsymbol{\epsilon}\ [\mathbf{2.3664}, \mathbf{867.2328}]$ Pa).

3.1.10 Steady Heave Force

It is important to look at how the heave force varies with the steady angles of attack of the spheroid. While the flow and heave force will be different for a spheroid at a steady angle of attack than it would be at the same angle of attack at some instance of a PMM test, this measure gives an idea of what forces to expect solely from the spheroid being at a given angle of attack. Figure 3-11 shows how the heave force increases faster than quadratically with angle of attack. Fitting the data to a power function reveals that with $Z' \approx a\alpha^b$, $a = 1.1792e-04$ and $b = 3.1011$ gives the best fit shown in Figure 3-11.

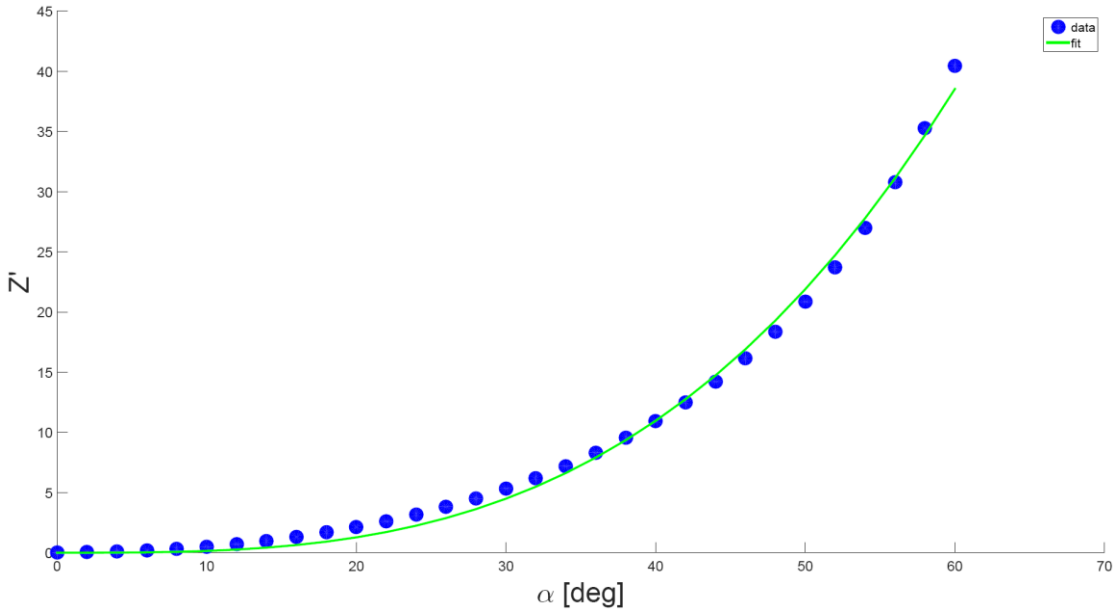

Figure 3-11: Spheroid heave force vs angle of attack.

Breaking down the lift force down into shear and pressure forces reveals that the heave force due to pressure at steady angles of attack increases faster than the heave force due to shear stresses, as is clearly shown in Figure 3-13. In region A of Figure 3-13 there is little cross flow separation until approximately $\alpha = 7°$. After, in region B, the cross flow separation increases in severity and the region over which it effects increases. Because separated flow leads to a lack of pressure recovery, the pressure in this region is in general lower as shown in Figure 3-12. This decrease in pressure on the backside (top) of the spheroid is associated with the rapid increase in heave force due to pressure relative to the heave force due to shear. In region C, the pressure force due to cross flow separation continues to increase faster than the heave force due to shear, but at a reduced rate. This is likely because the area over which the cross flow separation causes a drop in pressure does not increase as quickly with increasing angle of attack as it did at smaller angles. What this indicates is that the pressure forces associated with heave velocity should tend to dominate the heave force on the spheroid during PMM tests, especially at large angles of attack, because of cross flow separation.

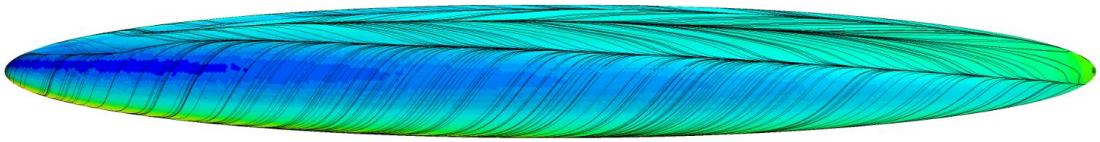

Figure 3-12: Flow over spheroid at $\boldsymbol{\alpha = 30°}$ showing how pressure is reduced after crossflow separation. Black lines indicate shear stress trajectories. (For reference: $\boldsymbol{p \in [-7428.8, 9981.2]}$ Pa)

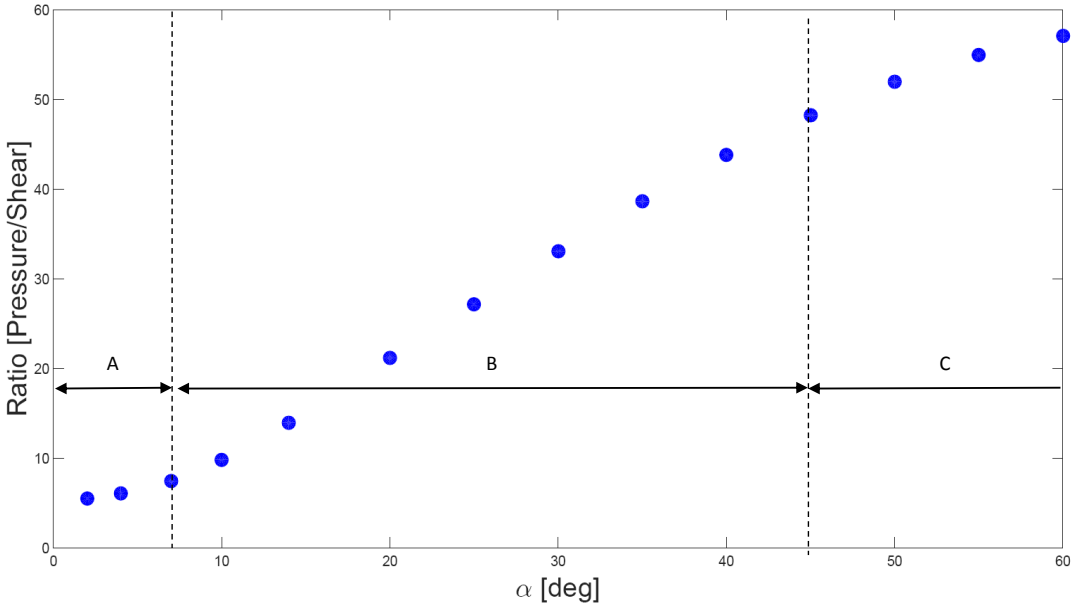

Figure 3-13: Graph shows how the ratio of the pressure heave force over the shear heave force increases with angle of attack.

3.2 Validity of Quasi-Steady Models

The assumption of quasi-steady flow is only good if the severity of the maneuver is slow enough such that the wake ("memory" in the fluid) from pervious motions are washed downstream before strongly interacting with the body. For PMM tests, this means a low nondimensional frequency. The nondimensional frequency can be defined as the inverse of the number of body lengths the body travels in one period.

$$f' = \frac{1}{\#\ Body\ Lengths\ Traveled\ per\ Period} \tag{3.1}$$

A nondimensional frequency less than one means the body travels more than 1 body length per period whereas a nondimensional frequency greater than 1 means the body travels less than 1 body length per period. These higher frequency test cause the wake of the body to interact heavily with the body.

In the interest of giving a feel for how the heave force differs for steady verses unsteady angles of attack, a simulation was performed where an ellipsoid was quickly brought from steady zero angle of attack to a steady angle of attack by adding heave

velocity, then quickly returned to zero angle of attack. An exact description of the motion is this:

1. Spheroid is at zero angle of attack for 2 body lengths.
2. Spheroid accelerates in heave at a constant rate such that the body heaves n diameters (where n is the number of diameters heaved) when it reaches its steady angle of attack of 30°.
3. Spheroid stays at $\alpha = 30°$ until it travels 3 body lengths at constant angle of attack.
4. Spheroid decelerates in heave at a constant rate such that the body heaves n diameters when it reaches zero angle of attack.
5. Spheroid travels at zero angle of attack until it travels 2 body lengths.

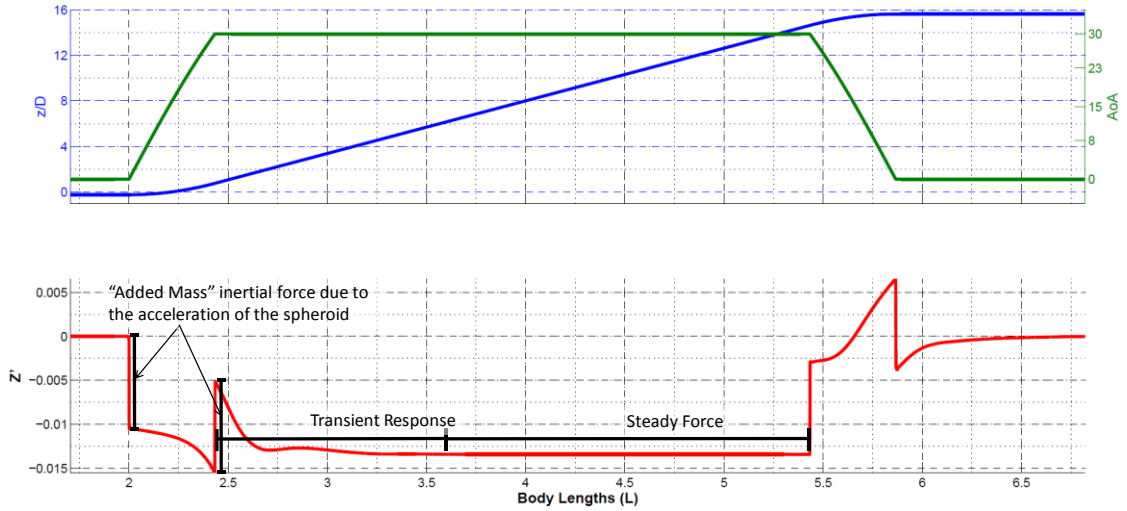

Figure 3-14: Simulation demonstrating transient response of the fluid body system to quick changes in angle of attack of $\boldsymbol{\alpha = 0°}$ to $\boldsymbol{\alpha = 30°}$ and then back to $\boldsymbol{\alpha = 0°}$ with $\boldsymbol{nD = 1}$.

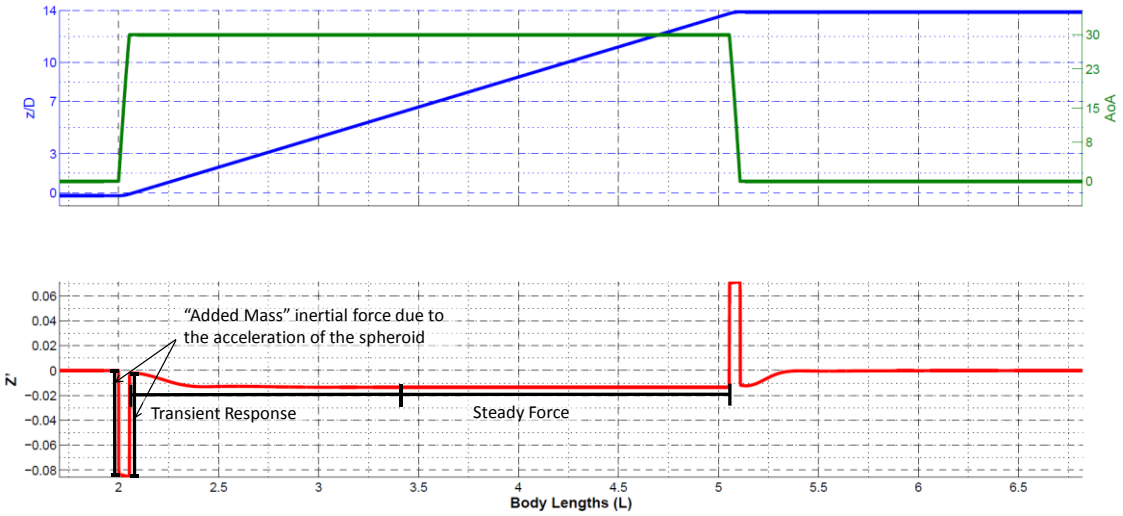

Figure 3-15: Simulation demonstrating transient response of the fluid body system to quick changes in angle of attack of $\boldsymbol{\alpha = 0°}$ to $\boldsymbol{\alpha = 30°}$ and then back to $\boldsymbol{\alpha = 0°}$ with $\boldsymbol{nD = 1/4}$.

For the case where $nD = 1$, some interesting features of the force response can easily be seen when analyzing Figure 3-14. First, the increase in force when the spheroid is being accelerated is approximately equal to the product of the ideal added mass coefficient and the acceleration. The same change in force when the spheroid is being accelerated is seen when the spheroid is being decelerated. Second, from the time the spheroid stops accelerating, it takes approximately 1.15 body lengths for most of the transients to die out before reaching a relatively steady heave force. If the spheroid is accelerated at 4 times the previous rate such that $nD = 1/4$, a slightly different force response is seen as shown in Figure 3-15. The spheroid which was accelerated faster takes longer to reach a state of equilibrium than the slower accelerating spheroid (~1.35 body lengths), but has larger transients relative to steady state. The reason for this is that the flow has more time to develop for $nD = 1$, traveling vertically much further before reaching the steady angle of attack. The differences in the heave force responses can be attributed to the memory in the fluid. If this were potential flow (a flow without memory), the fluid would respond instantly to the state of the body, and quasi-steady models would be acceptable. As an extreme example, if the body could be accelerated instantly to the desired angle of attack, the flow would instantly be at steady state in potential flow. For real flows however, the fluid takes time to adjust to the body's new state, making quasi-steady models less appropriate because the forces now depend on the previous states of the body and not just the current state.

In this simple simulation, the faster the acceleration, the more time the flow takes to adjust. This highlights the fact that the heave force response depends on the rate the spheroid was accelerated. Readers can conclude from these simple simulations that it takes time for the flow to reach a steady state, and because the flow for PMM tests is unsteady, steady forces on a spheroid such as those in Figure 3-11 can only hope to provide estimates of expected heave forces in a PMM test.

3.3 PMM Flow Features

The flow features generated in PMM tests are similar to those produced in steady flows. One difference is that some of these features do not fully develop, or develop into slightly different structures based on the frequency and amplitude of the test. The second difference is that when the body changes directions, the body will move through the wake generated by the previous upward/downward motion. This greatly changes the flow over the body, which in turn greatly affects the pressure and shear distribution over the spheroid. These effects however are thought to be small as they are not evident in heave force responses shown in the next section. This is most likely due to the fact that most of the body is out of the previous wake as it begins to heave in the opposite direction, which is due to the low nondimensional frequencies used for the PMM tests.

4. PMM Model Results and Discussion

In this section we analyze the heave force on the spheroid as it undergoes a PMM test at nondimensional amplitudes and frequencies both ranging over $\{0.05, 0.1, 0.2\ 0.3\ 0.4\ 0.5\}$. All quantities in this section are given in nondimensional form unless stated otherwise. Each simulation was run over 3 periods of oscillation, where only the final period was used for analysis to help eliminate transients due to the nonconformal initial conditions. In-depth discussions will follow on how the amplitude and frequency of the test effect the flow and the forces the spheroid experiences. I would like to be clear here that the system formed by the fluid and spheroid form a nonlinear system and that the goal is to then indicate which of the models best captures the physics of the flow, and at what amplitudes and frequencies these models begin to break down and why.

Important tabulated results to be discussed are provided in Appendix I for reference.

4.1 Fluid-Body System

It is important to first discuss how we will define when a system goes from something close to a linear time invariant (LTI) system to a more nonlinear and time varying system. Given an LTI system, a sinusoidal input will produce a sinusoidal output with possibly differing amplitude and phase. Hypothetically, this means that if the body is moved sinusoidally, then the force on the body will vary sinusoidally and the system given by (1.58) with the linear damping model can exactly describe the system. If this model is not able to reproduce the response exactly, then the system is not an LTI system and hence cannot be modeled precisely as such. Systems undergoing a PMM test which produce outputs 'close' to a sinusoid may be able to be modeled as an LTI system with some tolerable error. Here we define the error to be the difference between the actual force on the body, and the force predicted by the model. For the virtual PMM tests in heave being considered, the error is given as

$$error = |\mathrm{Z}'_{sim} - \mathrm{Z}'_{model}| \tag{4.1}$$

where Z'_{sim} is the actual nondimensional force calculated in the CFD simulation and Z'_{model} is the nondimensional force predicted by the model at the corresponding phase point. Ultimately, this error is only an indication of how well the model performed for a given PMM test. It only suggests how well the model will perform when the body undergoes general maneuvers, such as nonperiodic maneuvers in multiple DOF's.

For the heave PMM tests to be discussed, one qualitative tool and two quantitative measures were used to judge how well a given model performed over the final period of the PMM test. The qualitative tool was simply plotting the simulation force response with the model's fit and judging how well the model force response matched the simulation force response. If the simulated force response showed anything other than a sinusoidal response, it could immediately be concluded that the system under consideration was not LTI. Depending on how close the model fit matched the simulation force response, one

could begin to judge if the model was good enough. The first quantitative measure used was the total mean squared error (MSE_{tot}) given as

$$MSE_{tot} = \frac{SS_{res}}{N} \tag{4.2}$$

where

$$SS_{res} = \sum_{i=1}^{N} \left(\mathrm{Z}'_{sim}(i) - \mathrm{Z}'_{model}(i)\right)^2 \tag{4.3}$$

where N is the number of observations, SS_{res} is the sum of the squared residuals, and the sum is taken over the final full period of the simulation at each time step i. The MSE_{tot} can be thought of as a metric for the total error between the model and the simulation. The second quantitative measure is the coefficient of determination (R^2) given as

$$R^2 = 1 - \frac{SS_{res}}{SS_{tot}} \tag{4.4}$$

where

$$SS_{tot} = \sum_{i=1}^{N} (\mathrm{Z}'_{sim}(i) - \bar{\mathrm{Z}}'_{sim})^2 \tag{4.5}$$

and

$$\bar{\mathrm{Z}}'_{sim} = \frac{1}{N} \sum_{i=1}^{N} \mathrm{Z}'_{sim}(i) \tag{4.6}$$

is the average heave force output by the simulation. The coefficient of determination takes on values from zero to one, and represents how well the model fits the data. Models with higher R^2 values indicate the model is able to "explain" more of the data and hence gives a better fit. The MSE_{tot} is a metric that should only be used to compare models across similar PMM tests because the error is relative to the individual PMM tests. The coefficient of determination is better suited for comparing models across all PMM tests because it is on a normalized scale.

4.2 Added Mass Variation

Each model under consideration includes the product of the added mass and the acceleration of the body. However, even with different damping term formulations, the added mass term for each model are nearly identical as indicated in Figure 4-1. Differences only arise due to the different damping models with slightly different damping terms.

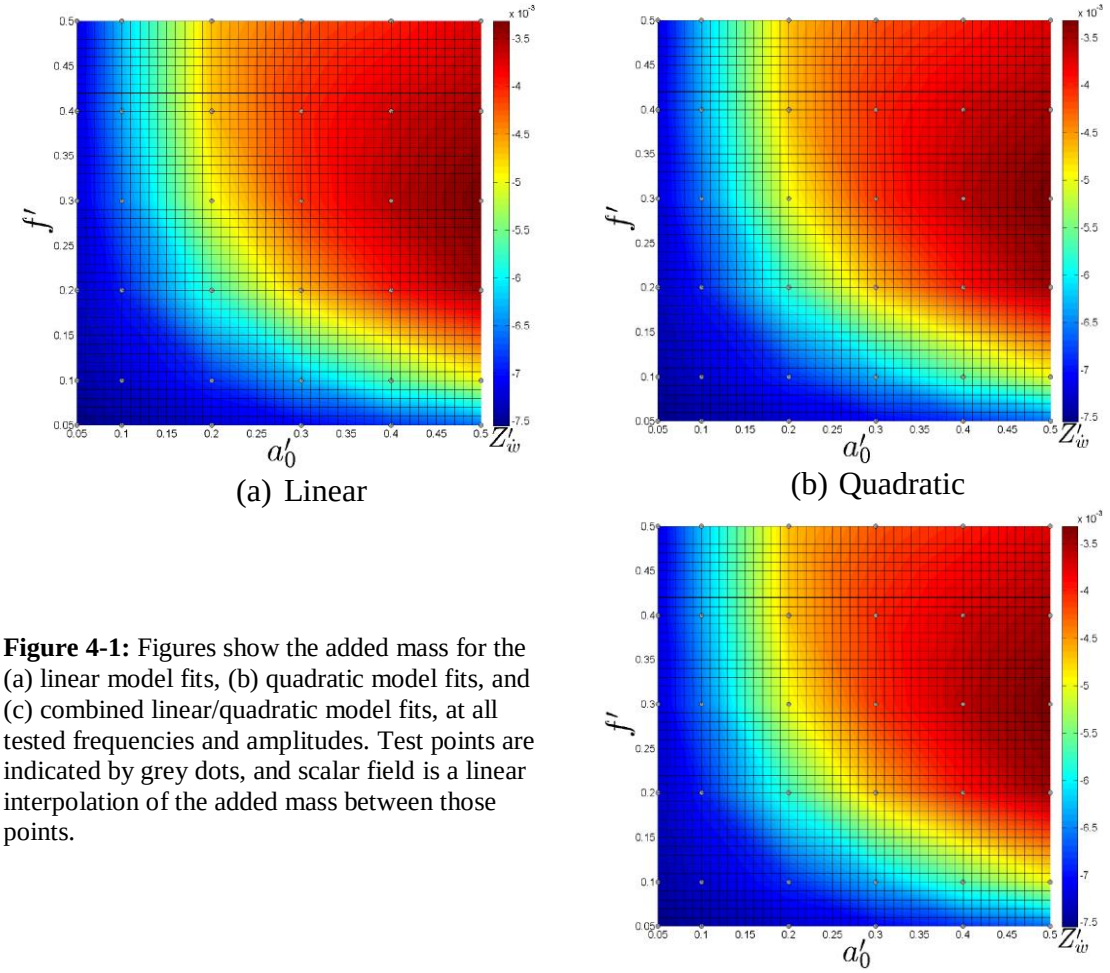

(a) Linear

(b) Quadratic

(c) Combined Linear/Quadratic

Figure 4-1: Figures show the added mass for the (a) linear model fits, (b) quadratic model fits, and (c) combined linear/quadratic model fits, at all tested frequencies and amplitudes. Test points are indicated by grey dots, and scalar field is a linear interpolation of the added mass between those points.

This highlights how the added mass term remains seemingly unchanged, no matter the damping model being employed. It also indicates how different viscous flow is compared to ideal flow, because if this were an ideal flow, the graphs would be constant across all amplitudes and frequencies.

4.3 Damping Coefficients

As will be shown in §4.5, the combined linear/quadratic damping model produces the least error in the model fit to the simulation force time history. This result is not surprising because by including both linear and quadratic damping models, it should be able to perform at least as well as either model on its own.

Comparing calculated values of the damping coefficients (see Appendix I) for the linear and quadratic models with the linear and quadratic damping coefficient of the combined linear/quadratic model, shows how the linear damping coefficients in the combined linear/quadratic damping model tend towards the damping coefficients in the purely linear model. This is especially true for the low amplitude and low frequency PMM tests where the nonlinearities in the force response are minor. This suggests the

superiority of the linear damping model over the quadratic, at least for the tested frequencies and amplitudes.

A striking relationship was found between the linear damping models and the quadratic damping models. If we compare the linear model to the quadratic model given explicitly by (4.7) and (4.8)

$$Z' = Z'_{\dot{w}'}\dot{w}' + Z'_{w'}w' \tag{4.7}$$

$$Z' = Z'_{\dot{w}'}\dot{w}' + Z'_{w'|w'|}w'|w'| \tag{4.8}$$

and assume the two models produce similar heave responses, then

$$Z'_{w'} \propto Z'_{w'|w'|}|w_{char}| \tag{4.9}$$

for some characteristic velocity w' in the PMM test. The characteristic velocity used was w_{max} yielding the following relation

$$\frac{Z'_{w'}}{Z'_{w'|w'|}|w_{max}|} = h \tag{4.10}$$

If this relationship holds for the same h over many frequencies and amplitudes, then the linear drag and quadratic drag coefficients can be estimated from one another.

Table I-10 shows that $h \approx 0.88 \mp 0.025$ over all amplitudes and frequencies considered. This means that at the maximum heave velocity, the linear model will predict 87% of the heave forces predicted by the quadratic model. From this one could potentially derive quadratic damping terms from linear damping terms and vice versa if h is constant over all the amplitudes and frequencies considered.

4.4 Qualitative Analysis

The following section gives a qualitative analysis, as outlined in §4.1, of the appropriateness of the linear and quadratic models for modeling PMM tests performed at various nondimensional amplitudes and frequencies. The change in the force response as the frequency and amplitude of oscillation is varied is most clearly seen keeping one variable constant while varying the other. These will be referred to as PMM sweeps. The combined linear/quadratic model is very similar to the linear model and is therefore not analyzed separately. All plots have time nondimensionalized by frequency such that $t^* = tf$. This is done so full periods of PMM tests of different frequencies can be shown on the same plot.

4.4.1 Linear Models

In this section, an analysis of the force response of PMM sweeps is performed, along with a linear analysis (where the system is assumed to be linear) of the linear force response model. An emphasis must be put on the fact that this is a linear analysis of a nonlinear system, so not all conclusions can be treated as decisive. This is because extrapolation and even interpolation can lead to erroneous conclusions when dealing with phenomena which are known to be nonlinear. Therefore, all interpolations should be taken as indicators of how the given variable will change if the data points are fine enough to capture the nonlinear features of the actual variation (and this is a big assumption, but a reasonable one for the system under consideration).

4.4.1.1 $a_o' = 0.05$ and $f' = 0.05$

In this section we compare how the force response changes with varying amplitude and frequency while holding individually the nondimensional frequency and amplitude at 0.05. We also discuss how well the linear damping model models the force response at these amplitudes and frequencies. These plots are shown in Figure 4-2.

(a)

(b)

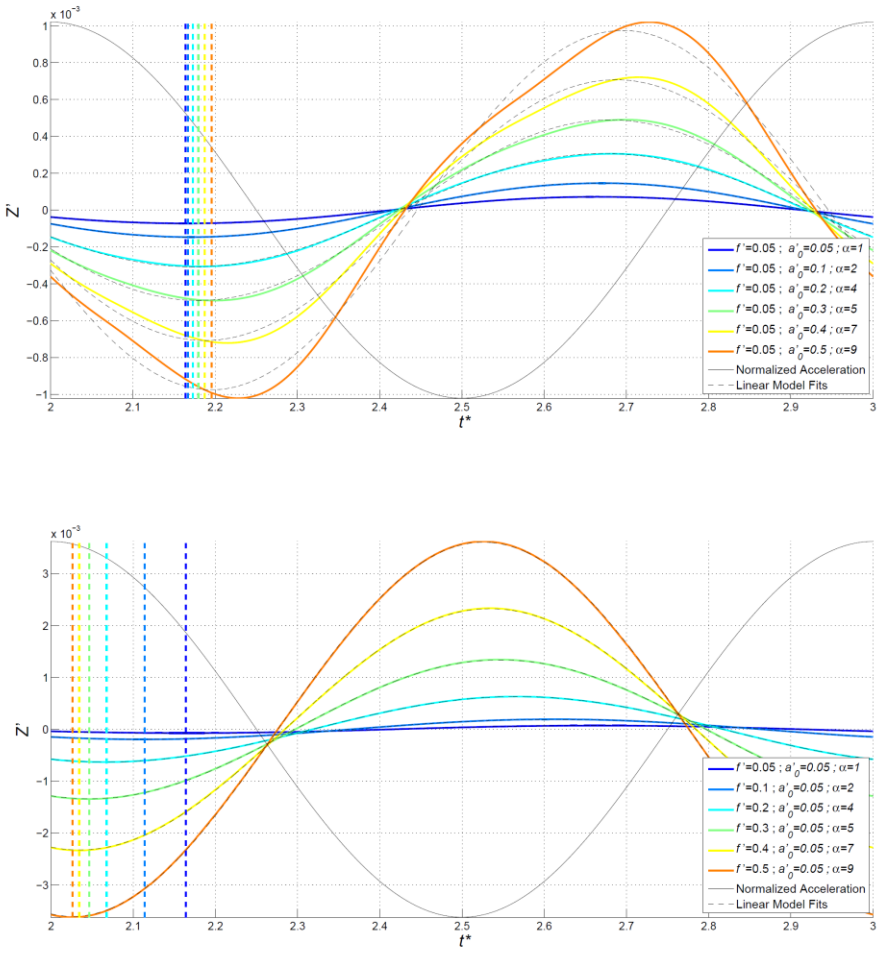

Figure 4-2: (a) Force time histories of heave PMM test holding the frequency at a constant 0.05 and varying the amplitude. (b) Force time histories of heave PMM test holding the amplitude at a constant 0.05 and varying the frequency. Vertical lines represent time shift of the linear model with respect to PMM test of matching color. Force time histories from the PMM simulation are color coded with accompanying linear model fits indicated by a dashed line. The normalized acceleration is shown to indicate the relative phase of the force response to acceleration.

The PMM sweeps shown in (a) and (b) of Figure 4-2 both sweep through the same angles of attack varying (defined in §1.9) between 1 and 9 degrees, but display very different force responses with increasing angles of attack. All force responses through the frequency sweep (Figure 4-2 (b)) show very linear responses, with decreasing phase shifts as frequency increases. This decreasing phase shift can be explained by equation (1.92), where it is seen that if the added mass and damping coefficients are approximately constant[21], the phase shift will decrease with increasing frequency. However, the force responses in Figure 4-2 (a) clearly shows an increasing nonlinear response as the amplitude is increased. This nonlinearity skews the force response to the left at low velocities and to the right at high velocities. As will be shown, this nonlinearity grows

[21] Refer to Appendix I to verify that the added mass and damping coefficient remain approximately constant.

larger with increasing amplitude because the ellipsoid travels a further distance, giving the flow the opportunity to more fully develop over the entire body. With $a' = 0.05$ the body travels just 0.4 diameters, while at $a' = 0.5$ the body travels 4 full diameters, 10 times as far as the lowest amplitude. At the high frequencies and low amplitudes of the frequency sweep, the body does not travel far enough for the flow to develop (e.g. the wake and cross flow separation). And because the frequency is constant (along with approximately constant added mass and damping coefficients), the phase shift is not as great, as suggested by equation (1.92). By visual inspection, the linear model can be said to perform fairly well for both frequency and amplitude sweeps in comparison to sweeps performed at larger amplitudes and frequencies.

4.4.1.2 $a_o' = 0.2$ and $f' = 0.2$

In this section we compare how the force response changes with varying amplitude and frequency while holding individually the nondimensional frequency and amplitude at 0.2. We also discuss how well the linear damping model models the force response at these amplitudes and frequencies. These plots are shown in Figure 4-3.

(a)

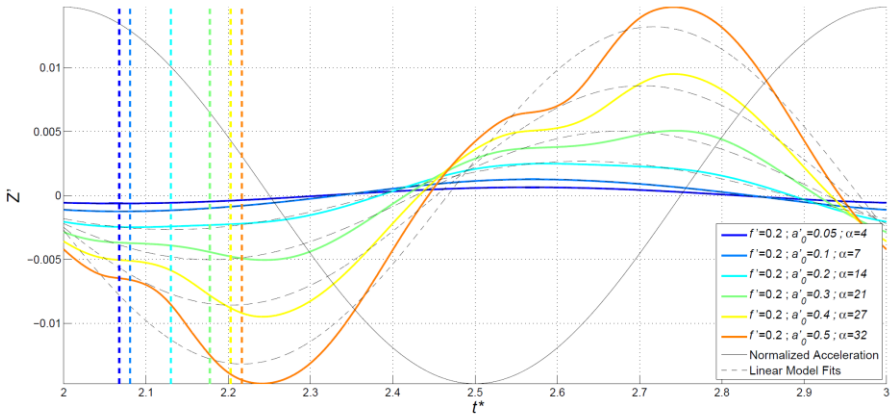

(b)

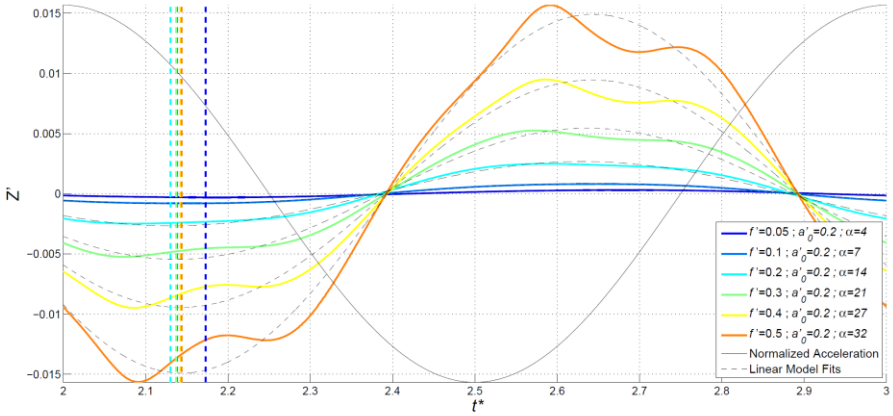

Figure 4-3: (a) Force time histories of heave PMM test holding the frequency at a constant 0.2 and varying the amplitude. (b) Force time histories of heave PMM test holding the amplitude at a constant 0.2 and varying the frequency.

Figure 4-3 shows PMM sweeps through angles of attack between 4 and 32 degrees. Both PMM sweeps show large nonlinearities in their force responses starting at an angle of attack of approximately 14 degrees. However, the character of the nonlinearity is slightly different than that seen in the amplitude sweep at a frequency of 0.05. In the amplitude sweep seen in Figure 4-3 (a), the global max per half period shifts towards the maximum velocity because the heave force due to the angle of attack (see Figure 3-11) increases faster than the heave force due to added mass. Here a dip (decrease in the force) occurs before the maximum force is reached. In the frequency

sweep shown in Figure 4-3 (b), the dip occurs after the maximum because the frequency sweep see's larger accelerations than in the amplitude sweep.

It was found that in general, lower amplitude, higher frequency PMM tests had a *global* maximum located near the maximum acceleration, followed by a *local* maximum on each half period. This is because higher accelerations lead to larger inertial forces (think added mass). Higher amplitude and lower frequency maneuvers will in general have a local maximum followed by a global maximum near the maximum velocity over each half period. This effect may be attributed to an increase in cross flow separation due to the longer heave motions which give the cross flow separation more time to fully develop than in the lower amplitude cases.

By visual inspection the linear model is still able to follow the main force response (i.e. capture its largest features); however, it is incapable of modeling these sudden dips. This inadequacy in the model is inherent in all damping models considered in this paper.

One might ask why the phase shift seems to be the opposite as that seen in Figure 4-2, and the answer is that the relative change in the added mass and damping coefficient begins to become large as can be deduced from the added mass and damping tables in Appendix I. For the amplitude sweep, the ratio $Z'_{\mathrm{w}}/Z'_{\dot{\mathrm{w}}}$ is increasing, meaning the phase is increasing. For the frequency sweep, the ratio $Z'_{\mathrm{w}}/Z'_{\dot{\mathrm{w}}}$ is proportional to the one over the frequency, so the phase varies only slightly. A more visual way to see how the phase changes with the frequency and amplitude is shown in §4.4.1.5.

4.4.1.3 $a_o' = 0.5$ and $f' = 0.5$

In this section we compare how the force response changes with varying amplitude and frequency while holding individually the nondimensional frequency and amplitude at 0.5. We also discuss how well the linear damping model models the force response at these amplitudes and frequencies. These plots are shown in Figure 4-4.

(a)

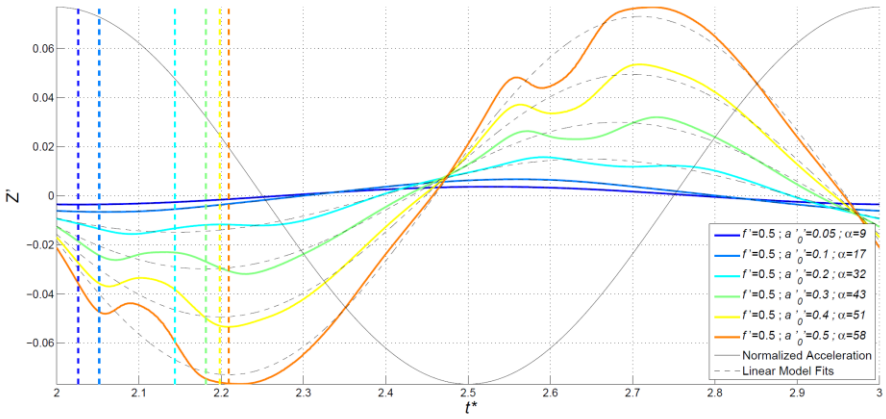

(b)

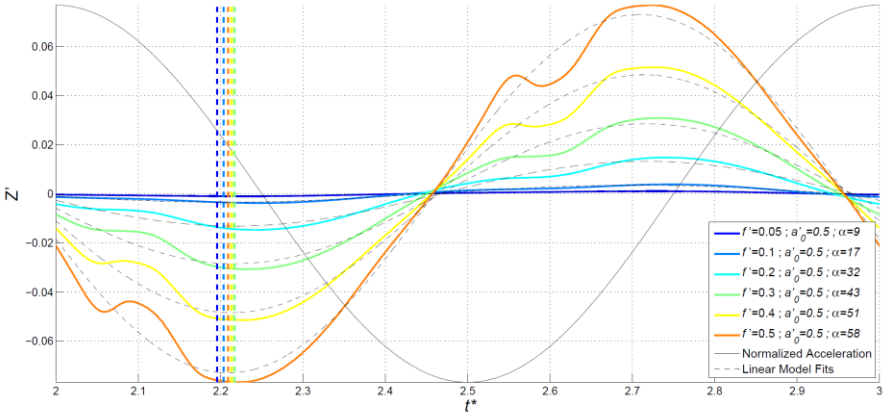

Figure 4-4: (a) Force time histories of heave PMM test holding the frequency at a constant 0.5 and varying the amplitude. (b) Force time histories of heave PMM test holding the amplitude at a constant 0.5 and varying the frequency.

Figure 4-4 shows PMM sweeps through angles of attack between 9 and 58 degrees. Because the PMM tests were performed at the largest amplitude or frequency considered, it is expected and seems to be that the force responses will show the greatest nonlinearity of all the sweeps. The character of all the force response of both PMM sweeps is most similar to that seen in the amplitude sweep in Figure 4-3 (a), where the dip occurs before the maximum force and the severity of the dip has increased. This is because large angles of attack lead to large heave forces, where the heave force due to the angle of attack (refer to Figure 3-11) dominates the heave force due to added mass. As

shown in §3.1.10, this is thought to be due to the cross flow separation. In Figure 4-4(a) and (b), the phase shift occurs for the same reasons as seen in Figure 4-3. By visual inspection, the linear model is still able to capture the major features of the force response.

4.4.1.4 Angle of Attack Sweep

In this section we compare how the force response changes with equal increases in amplitude and frequency. We also discuss how well the linear damping model models the force response at lowest and highest angles of attack. These plots are shown in Figure 4-5.

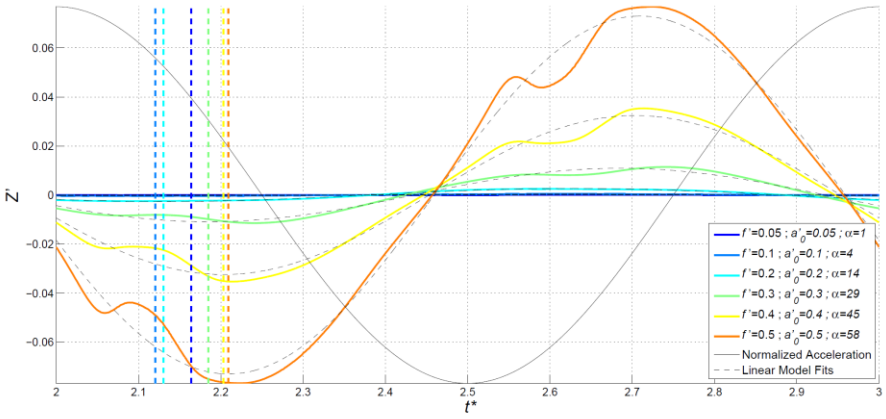

Figure 4-5: Force time histories of heave PMM test varying frequency and amplitude from 0.05 to 0.5.

Figure 4-5 can be deduced mostly from the previous PMM sweep graphs; however, this figure explicitly shows how the character of the force response changes from the lowest angle of attack to the highest on one figure. At low angles of attack, the major nonlinearity (the dip) is small. As the angle of attack is increased, this nonlinearity increases in severity. It is hard to quantify when this nonlinearity becomes large based solely on a visual inspection of the graphs because the scales of the forces change with changing frequency and amplitude. The MSE_{tot} and R^2 values will be used to distinguish this point in §4.5.

4.4.1.5 Linear Model Time Shift

The manner in which the phase changes with frequency and amplitude is most clearly shown in Figure 4-6.

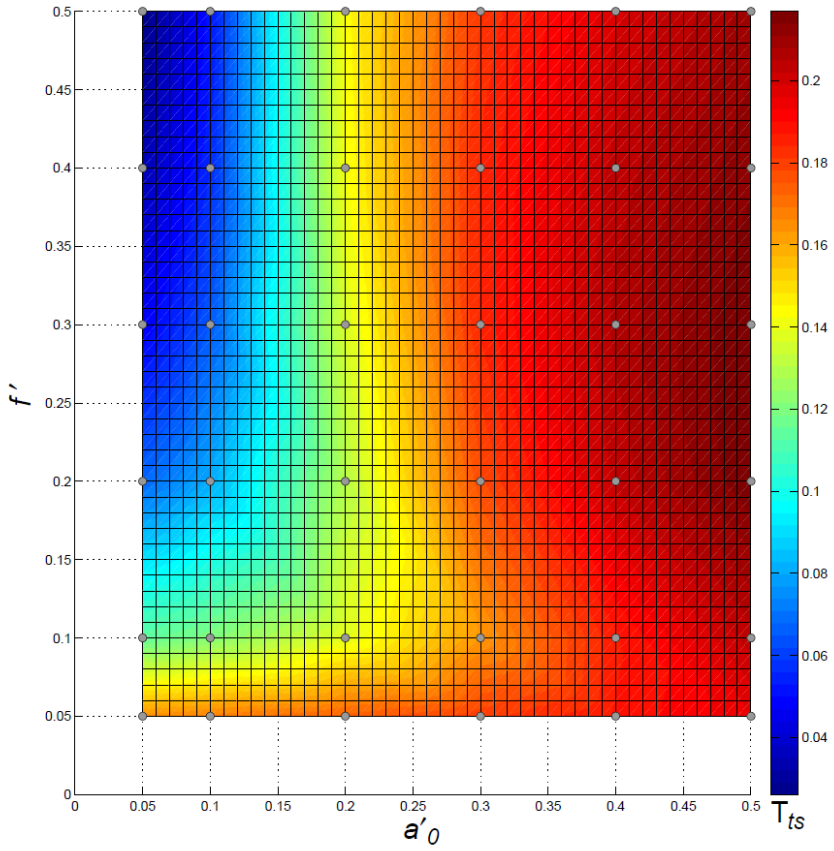

Figure 4-6: This figure shows how the phase changes with frequency and amplitude, where the grey points are simulation results, and the scalar field is a linear interpolation between these points.

Here we see just how complex the time shift is with varying frequency and amplitude. Small time (phase) shifts correspond to the cooler colors and large time shifts to the hot colors. The time shifts show how in or out of phase the force response is with the acceleration. For example, referring to Figure 4-2 (b), as the frequency is increased at low amplitude the phase shift decreases. This is why the dashed vertical lines move from right to left with increasing frequency. At low frequencies, the force response is less in phase with the acceleration than at higher frequencies. This complexity is due to the nonlinearity of the system.

4.4.2 Quadratic Model

The following section shows how well the quadratic model is able to represent the force response in comparison to how the linear model performed. Being a nonlinear model, it is able to represent some nonlinear responses; however, as will be shown it is not able to represent the nonlinear aspect of the flows at hand. Phase shifts are not included as these are really only relevant in a linear framework. Much of the comparison can be done by visual inspection, however, some must be done numerically. In these cases the reader is referred to Figure 4-7. Here the ratio of the MSE between linear and quadratic models is defined as

$$Ratio_{MSE} = \frac{MSE_{lin}}{MSE_{quad}} \tag{4.11}$$

where MSE_{lin} is the MSE between the force time history and linear model fit and MSE_{quad} is the MSE between the force time history and the quadratic model fit.

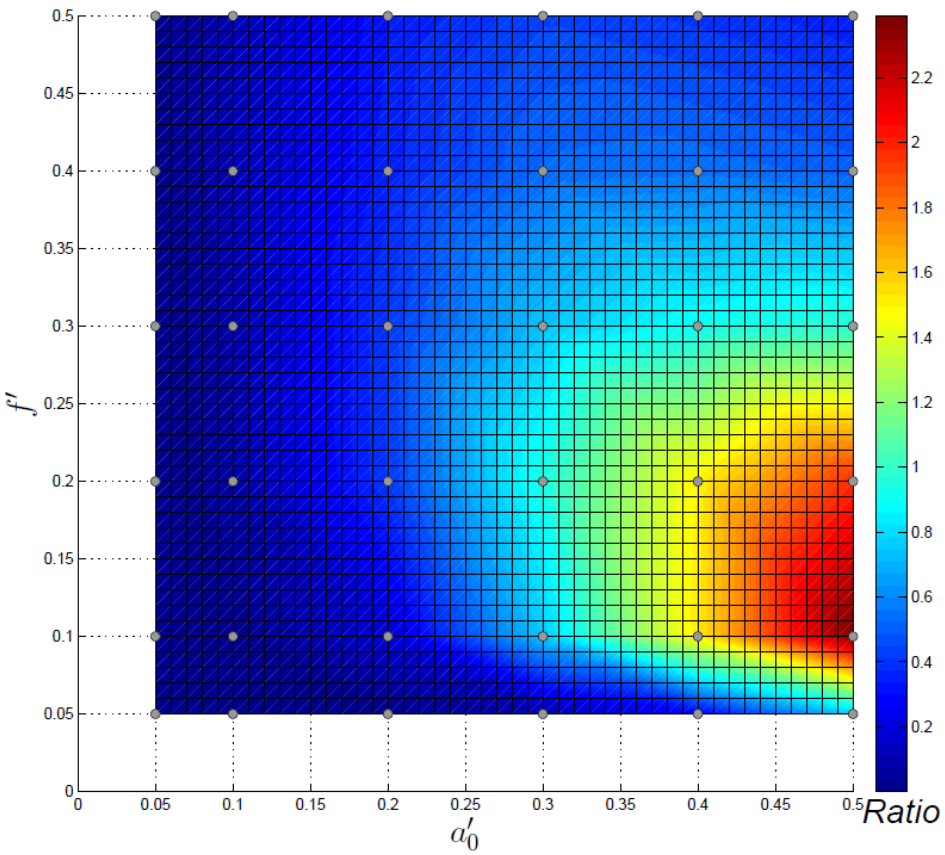

Figure 4-7: The above figure shows how the ratio of the ***MSE*** of the linear and quadratic model fits to the force response defined by equation (4.11) varies with frequency and amplitude. The grey points are data points, and the scalar in-between is an interpolation between those points.

Portions where the graph is below 1 (blueish) indicate the linear model having a lower MSE, indicating it is the better model. Only one area of the graph (red spot) where the frequency is low and the amplitude is high does the quadratic model outperform the linear model.

4.4.2.1 $a_o' = 0.05$ and $f' = 0.05$

In this section we discuss how well the quadratic damping model models the force response through amplitude and frequency sweeps holding both the nondimensional amplitude and frequency at 0.05. These plots are shown in Figure 4-8.

(a)

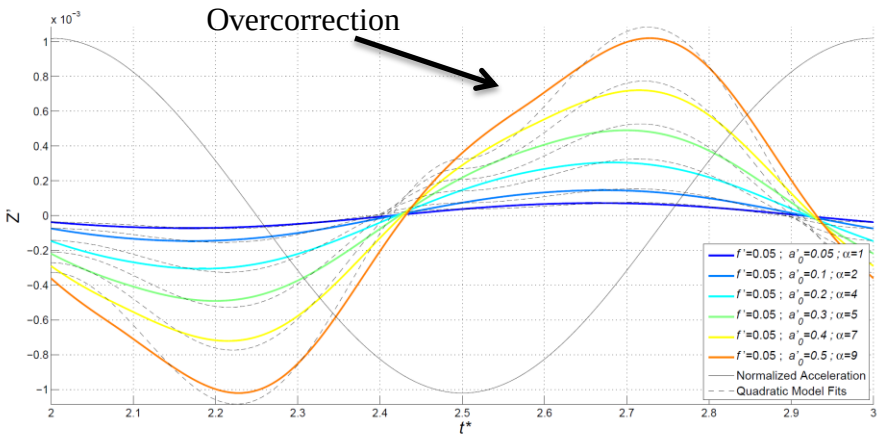

(b)

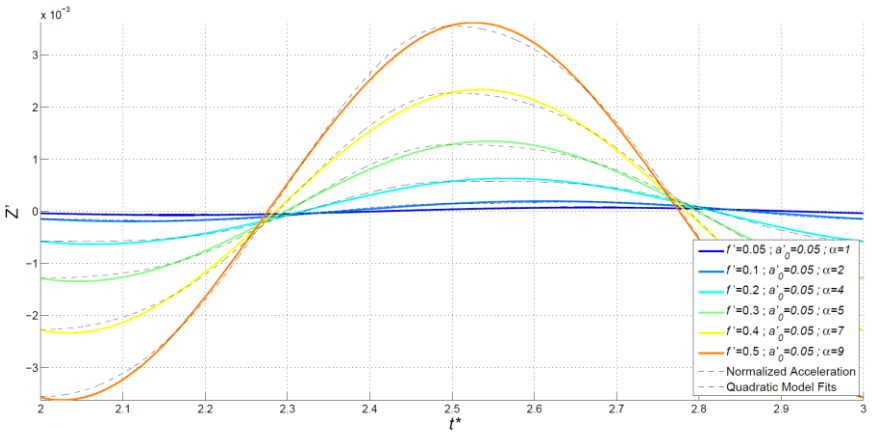

Figure 4-8: (a) Force time histories of heave PMM test holding the frequency at a constant 0.05 and varying the amplitude. (b) Force time histories of heave PMM test holding the amplitude at a constant 0.05 and varying the frequency.

Figure 4-8 shows PMM sweeps between 1 and 9 degree angles of attack. The quadratic model seems to overcorrect for the nonlinearities seen in the amplitude sweep in Figure 4-8 (a). Based on visual inspection it also does not seem to do as well

representing the force response in the frequency sweep shown in Figure 4-8 (b) as the linear model did. Referring to Figure 4-7, the linear model always outperforms the quadratic model through both PMM sweeps. The quadratic model does, however, do a relatively better job as the frequency and amplitude is increased, when compared to lower frequency and amplitude tests.

4.4.2.2 $a_o' = 0.2$ and $f' = 0.2$

In this section we discuss how well the quadratic damping model simulates the force response with varying amplitude and frequency while holding individually the nondimensional frequency and amplitude at 0.2. These plots are shown in Figure 4-9.

(a)

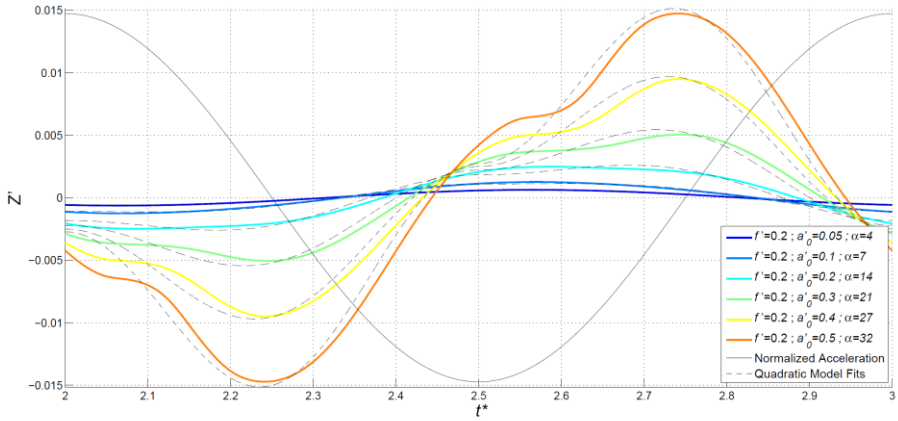

(b)

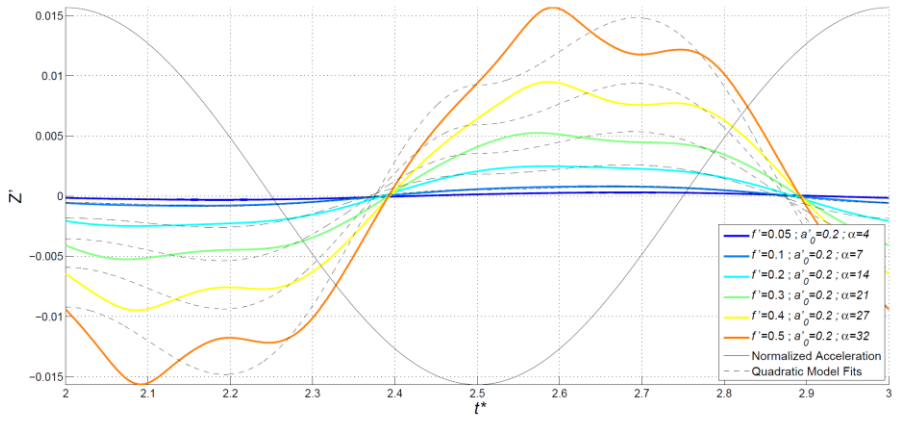

Figure 4-9: (a) Force time histories of heave PMM test holding the frequency at a constant 0.2 and varying the amplitude. (b) Force time histories of heave PMM test holding the amplitude at a constant 0.2 and varying the frequency.

Figure 4-9 shows PMM sweeps at angles of attack varying between 4 and 32 degrees. Once again the quadratic model, while able to include a quadratic nonlinearity in its force response, is not able to accurately represent the nonlinearity in the actual force response. Based solely on Figure 4-7, the linear model appears to generally do a better

job representing the force response. However, at high amplitudes, the quadratic model outperforms the linear model. This is probably because the quadratic model is capable of creating dips in the force response while the linear model is not.

4.4.2.3 $a_o' = 0.5$ and $f' = 0.5$

In this section we discuss how well the quadratic damping model models the force response with varying amplitude and frequency while holding individually the nondimensional frequency and amplitude at 0.5. These plots are shown in Figure 4-10.

(a)

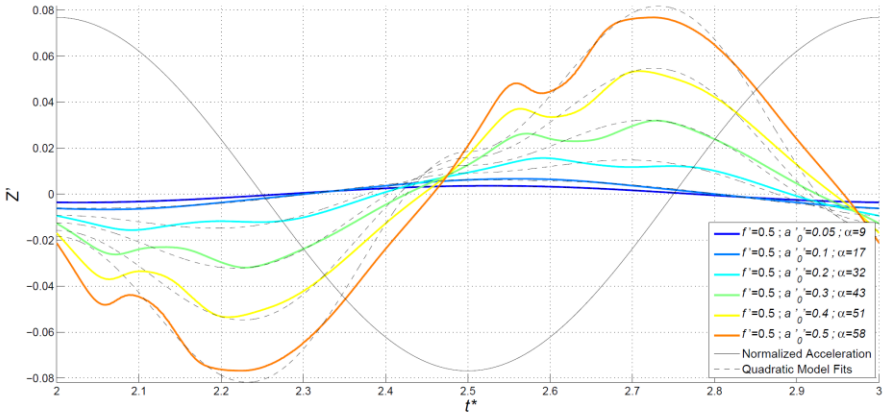

(b)

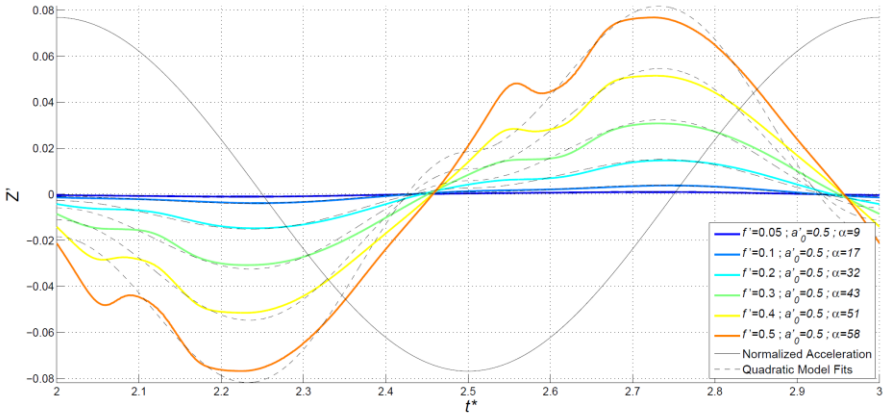

Figure 4-10: (a) Force time histories of heave PMM test holding the frequency at a constant 0.5 and varying the amplitude. (b) Force time histories of heave PMM test holding the amplitude at a constant 0.5 and varying the frequency.

Figure 4-10 shows PMM sweeps at angles of attack varying between 9 and 58 degrees. Like the force responses from Figure 4-9, the quadratic model is not able to represent the nonlinearity in the actual force response. Based solely on Figure 4-7, the linear model once again does a better job representing the force response.

4.4.2.4 Angle of Attack Sweep

In this section we discuss how well the quadratic model represents the force response with equal changes in amplitude and frequency through the entire range of angles of attack considered. These plots are shown in Figure 4-11.

(a)

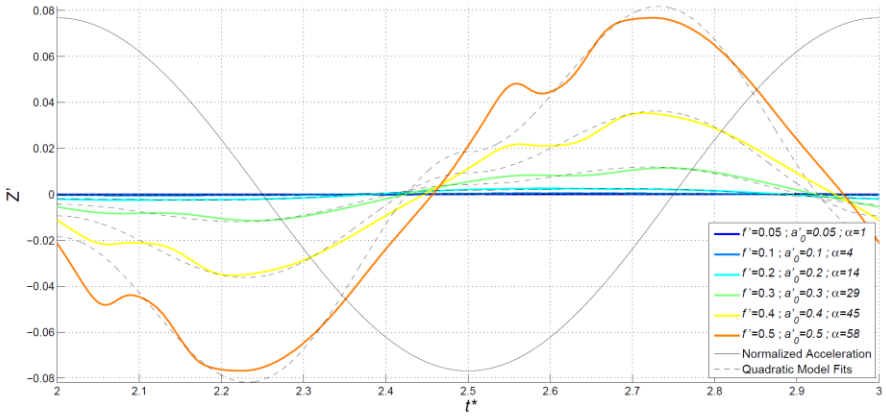

Figure 4-11: Force time histories of heave PMM test varying frequency and amplitude from 0.05 to 0.5. (Note: Quadratic model closest to respective simulation force time history is the model fit for that force time history.)

The trends displayed in Figure 4-11 can be deduced mostly from the previous PMM sweeps, but is shown here to explicitly show how the quadratic model performs through the entire range of angles of attack. It is hard to judge how well the model is doing at low amplitude and frequencies because of the scaling so Figure 4-7 can be used. The PMM tests considered here form a diagonal line across Figure 4-7, which is always in an area where the linear model has a lower MSE (i.e. the linear model outperforms the quadratic model).

4.5 Quantitative Analysis

In this section we use the tools discussed in §4.1, namely the MSE and the coefficient of determination, R^2, to quantitatively determine which model represents the force history response the best.

4.5.1 Model analysis using the MSE

The following section analyzes the MSE of the three models being considered for all virtual PMM tests performed, and visualized by Figure 4-12.

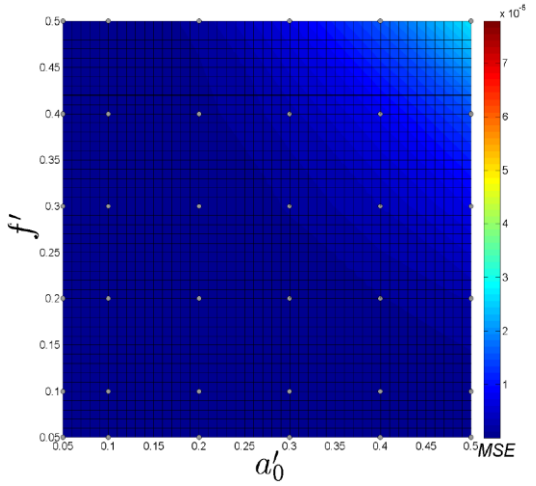

(a) Linear

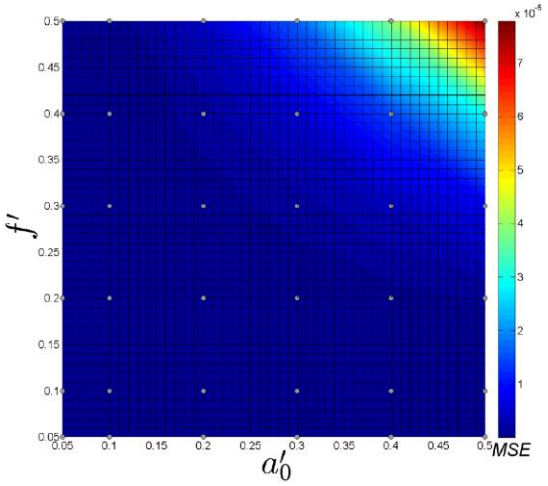

(b) Quadratic

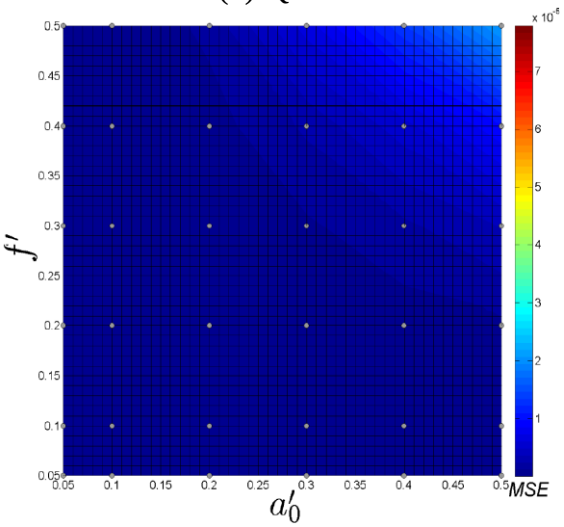

(c) Combined Linear/Quadratic

Figure 4-12: Figures show the ***MSE*** for the (a) linear model fits, (b) quadratic model fits, and (c) combined linear/quadratic model fits, at all tested frequencies and amplitudes. Test points are indicated by grey dots, and scalar field is a linear interpolation of the ***MSE*** between those points.

As was explained in §4.3, the combined linear/quadratic model is always able to reproduce the force time history with less error than the linear or quadratic model. And, because the combined model's linear coefficients converge to the linear coefficients in the linear model, it is not surprising that the MSE for these two models shown in Figure 4-12 (a) and (c) respectively are very similar (i.e. the combined linear/quadratic model approaches the linear model). Comparing all models, it is clear that all models perform poorest at large amplitudes and high frequencies. This is because the flow is the most nonlinear at these high amplitudes and frequencies. The amplitude and frequency at which the models are no longer applicable depends completely on the model requirements. If one requires an accurate model for a given vehicle, only low amplitude, low frequency maneuvers should be performed.

4.5.2 Model Analysis Using the Coefficient of Determination

This section analyzes the coefficient of determination (R^2) for all three models being considered for all virtual PMM tests performed and is visualized with Figure 4-13.

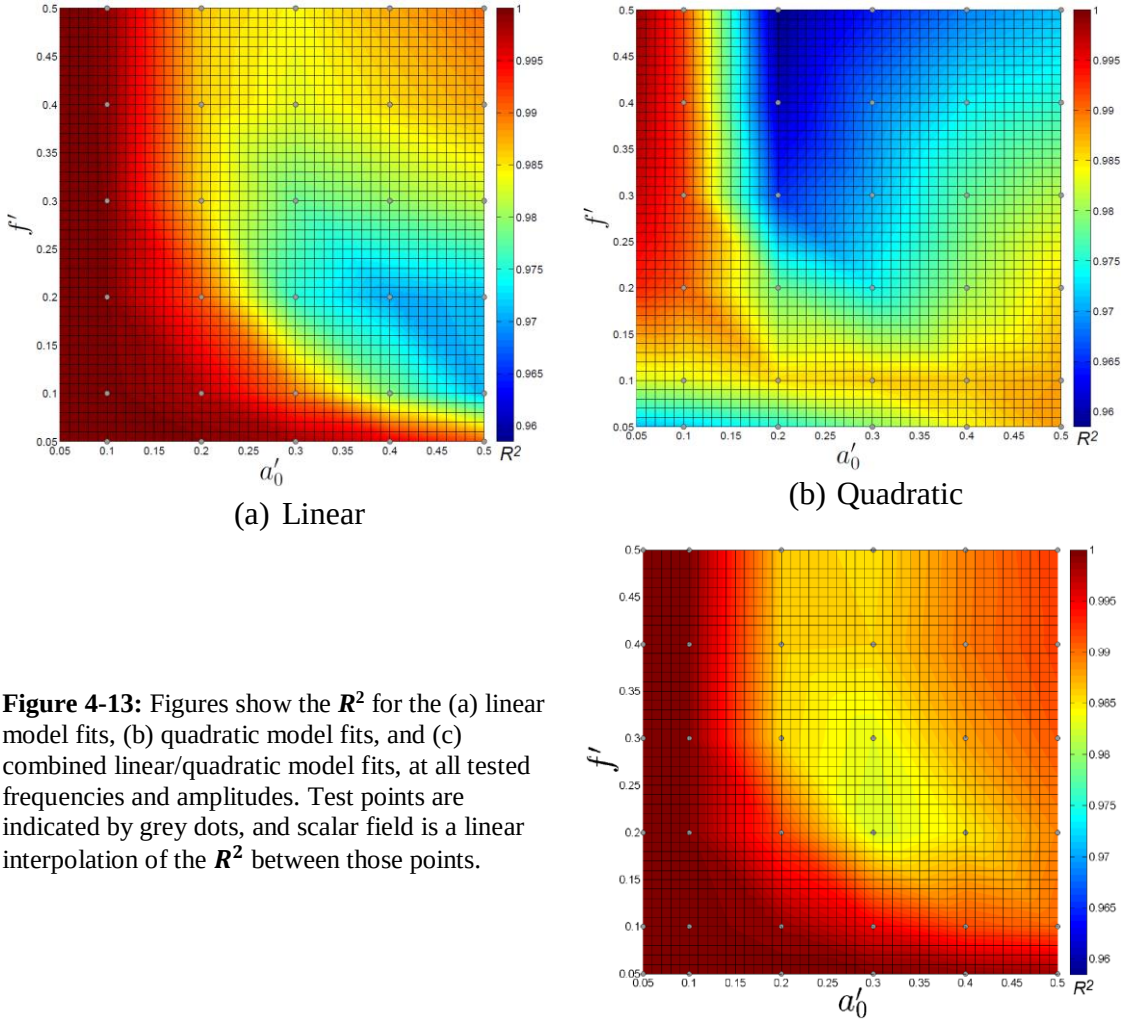

(a) Linear

(b) Quadratic

(c) Combined Linear/Quadratic

Figure 4-13: Figures show the R^2 for the (a) linear model fits, (b) quadratic model fits, and (c) combined linear/quadratic model fits, at all tested frequencies and amplitudes. Test points are indicated by grey dots, and scalar field is a linear interpolation of the R^2 between those points.

One may ask how this metric differs from the MSE, and the answer is that it takes into consideration the variance of the model to compute a value on a scale between 0 and 1. The most useful property of R^2 is that because it is confined to a scale between 0 and 1, this metric can easily be compared across PMM tests at all frequencies and amplitudes, whereas the MSE cannot. This is because the forces in higher frequency and amplitude PMM tests are in general higher leading to larger MSE.

Comparing the coefficient of determination across all 3 models leads to insight not seen in the graphs of the MSE. The linear model shown in Figure 4-13 (a) and the combined linear/quadratic model shown in Figure 4-13 (c) all perform the best at low frequencies and amplitudes, with the combined linear/quadratic model doing slightly better at the higher amplitudes and frequencies. The quadratic model on the other hand only performed well at low amplitudes. All three models performed the poorest at different frequencies and amplitudes. The linear model performed the worst at high

amplitudes and low frequencies. The quadratic model shown in Figure 4-13 (b) performed the poorest at medium amplitudes and high frequencies. Finally, the combined linear/quadratic model performed the poorest in the center of the frequency and amplitude range considered; medium frequencies and medium amplitudes. This may be because the optimizer is beginning to weight the linear and quadratic damping models equally, leading to modest results at amplitudes and frequencies where individually both the linear and quadratic damping models performed poorly.

4.6 PMM Test Guidance

Precise recommendations on how to perform PMM tests is highly dependent on the type of model that one is trying to identify for a given vehicle. However, for most applications where the vehicle is a general AUV, maneuvers will be gentle, and the linear model will be sufficient across most of the operating envelope. For this type of application, it would be recommended to perform PMM tests with both a nondimensional amplitude and nondimensional frequency less than 0.2. As was revealed in the previous figures, below this value, the heave force responses tend to stay fairly linear, with coefficients of determination for the linear model staying above 0.99, implying a highly linear response (which is what one wants when identifying parameters for a linear model).

5. Future Research

The area of computational fluid dynamics, despite major leaps in computing power, improved models, and numerical algorithms, is still very much in its infancy. It will be a long time before CFD tests can replace experimental tests, such that the user has as much confidence in CFD results as he would a physical test. A major drawback of CFD today is that the results obtained often still require experimental validation. The results thus far presented have hardly been validated at any reasonable level. Real PMM tests of an 8:1 spheroid would need to be performed with all the test conditions made as close to the simulation conditions as possible in order to obtain an estimate of the model error E_3 given by (1.75). Verification and Validation in Scientific Computing [16] gives a very detailed outline on how validation experiments should be performed. Without this type of validation, there is no way of knowing if the results obtained are physical. With a better idea of the total simulation error E_{sim} given by (1.74) and uncertainties associated with the simulation, an understanding of how the simulation will differ from a real experiment can be drawn, thereby increasing its predictive capabilities.

Perhaps the greatest shortcoming of this research endeavor was that model robustness was not determined. All models goodness of fit were analyzed with respect to the data they were derived from. An analysis on how robust the models can be at varying frequencies and amplitudes (with constant added mass and damping coefficients) should be performed. In this vein, the best coefficients over a range of amplitudes and frequencies should be made in an attempt to get as robust a model as possible.

All simulations considered in this report utilized a single degree of freedom: heave. This essentially prompted the assumption that the equations of motion for the body decoupled. Further research should be done to determine the validity of this assumption (i.e. do heave motions solely lead to heave forces). This research would then segue nicely into building models for coupled maneuvers, and determining how to virtually identify the model coefficients. Something more complex than PMM tests would need to be performed, as PMM tests can only impart "hydrodynamically pure" motions in one DOF.

In the above study, only heave PMM tests were considered, PMM tests for the rotational coefficients of a spheroid also need to be explored because phenomena not seen in the heave DOF may appear in the roll, pitch or yaw DOF. It is theorized that the analysis should be fairly similar for surge DOF of a spheroid (it will be exact in sway). After this, an analysis on the force response of arbitrary bodies in all 6 DOF would lead to even further insight.

Finally, as was alluded to in §3, the assumption of quasi-steady flow is useful but not good enough in some instances. As the nondimensional frequency is increased the wake will have an increasing impact on the flow and in effect, the force on the body. Models which contain information on the history of the past motion of the body are required to account for the current forces on the body. Attempts to encode this information into the model were made in [24] using Volterra Series but have not seen wide use.

6. Concluding Remarks

The use of CFD to both better understand fluid flows and to help design better models for those flows will continue to increase as computers get faster and fluid models get better. The work presented here is merely a stepping stone. What it provides are some of the basic ideas needed to pursue the integration of CFD and model development for AUVs. It was shown that PMM tests can be run in a virtual environment to assess the validity of linear, quadratic, and combined linear/quadratic damping models in the equations of motion generally represented by (1.48). Through virtual PMM testing, it was found that despite its simpler form, the linear damping model outperformed the quadratic damping model at all but a few amplitudes and frequencies. However, outside of the recommended nondimensional amplitude and frequency envelope of 0.2 neither model is entirely adequate. The ideas shown here can be extended to evaluate nearly any model for nearly any vehicle.

This paper also shows the usefulness of having virtual data from simulation over experimental data in that the user has the ability to easily access information one can, in many cases, not access in a real experiment. Examples of this are shown in §3.1, where the skin friction field for steady flow over a spheroid at various angles of attack is analyzed over the full body. It is in this detailed flow analysis that cross flow separation during PMM tests was found to have a major impact on the heave force response curves. It was also shown how the quasi-steady models considered in this paper are inadequate when the memory effects of the fluid need to be considered.

The robustness of CFD in getting all the desired data needed is something experiments may never be able to attain. However, this ability is what makes the use of CFD in the design of vehicles a great, and arguably necessary, tool.

Bibliography

[1] A. A. Sonin, "The Physical Basis of Dimensional Analysis," Cambridge, 2001.

[2] A. Goodman, "Experimental Techniques and Methods of Analysis Used in Submerged Body Research," 1960.

[3] R. E. D. Bishop and A. G. Parkinson, "On the Planar Motion Mechanism Used in Ship Model Testing," *Philosophical Transactions of the Royal Society of London. Series A, Mathematical andPhysical Sciences, Vol. 266, No. 1171,* pp. 35-61, 1970.

[4] A. C. Hochbaum, "Virtual PMM Tests for Manoeuvring Prediction," in *26th Symposium on Naval Hydrodynamics*, Rome, 2006.

[5] A. Phillips, M. Furlong and S. Turnock, "Virtual Planar Motion Mechanism Tests of the Autonomous Underwater Vehicle Autosub," in *STG-Conference / Lectureday "CFD in Ship Design"*, Hamburg, 2007.

[6] R. Coe and W. Neu, "Virtual Planar Motion Mechanism Tests in a CFD Enviornment," in *Virginia Space Grant Consortium Student Research Conference*, Williamsburg, 2012.

[7] R. Coe and W. Neu, "Amplitude Effects on Virtual PMM Tests," *IEEE,* 2012.

[8] M. Tobak and D. J. Peake, "Topology of Three-Dimensional Separated Flows," 1981.

[9] G. T. Chapman, "Topological Classifications of Flow Separation on Three-Dimensional Bodies," in *AIAA 24th Aerospace Sciences Meeting*, Reno, 1986.

[10] K. Wang, "Boundary Layer Over a Blunt Body at High Incidence with an Open Type of Separation," *Proc. Royal Soc*, p. 33–55, 1974.

[11] H. Zhou, K. Wang, C. Hu and S. Harrington, "Three-Dimensional Separated Flow Structure over Prolate Spheroids," The Royal Society, 1990.

[12] L. M. Milne-Thomson, Theoretical Hydrodynamics (Fourth Edition), London: Macmillan & Co LTD, 1962.

[13] H. Lamb, Hydrodynamics, London: Cambridge: At the University Press, 1895.

[14] K. Karamcheti, Principles of Ideal-Fluid Aerodynamics, Malabar: Krieger Publishing Company, 1966.

[15] T. I. Fossen, Handbook of Marine Craft Hydrodynamics and Motion Control, Chichester: Wiley, 2002.

[16] W. L. Oberkampf and C. J. Roy, Verification and Validation in Scientific Computing, Cambridge: Cambridge University Press, 2010.

[17] G. K. Batchelor, An Introduction to Fluid Dynamics, Cambridge: Cambridge University Press, 1967.

[18] D. C. Wilcox, Turbulence Modeling for CFD, DCW Industries, 2006.

[19] F. H. Imlay, "The Complete Expressions for "Added Mass" of a Rigid Body Moving in an Ideal Fluid," 1961.

[20] "7.2.2 Determining Turbulence Parameters," 20 09 2006. [Online]. Available: http://aerojet.engr.ucdavis.edu/fluenthelp/html/ug/node217.htm.

[21] J. A. Schetz, Boundary Layer Analysis Revised, Reston: american Institute of Aeronautics and Astronautics, Inc., 2010.

[22] F. M. White, Fluid Mechanics (fourth edition), McGraw-Hill.

[23] M. Judd, M. Vlajinac and E. Covert, "Sting-free drag measurements on ellipsoidal cylinders at transition Reynolds numbers," *J. Fluid Mech*, pp. 353-364, 1971.

[24] R. Bishop, R. Burcher and W. Price, "The Uses of Functional Analysis in Ship Dynamics," *Proceedings of the Royal Society of London. Series A, Mathematical and PhysicalSciences, Vol. 332, No. 1588,* pp. 23-35, 1973.

[25] J. Delery, Three-dimensional Separated Flow Topology: Critical Points, Separation Lines and Vortical Structures, London: ISTE Ltd, 2013.

[26] D. J. P. a. M. Tobak, "Three-Dimensional Interactions and Vortical Flows with Emphasis on High Speeds," 1980.

[27] L. A. Yates and G. T. Chapman, "Numerical Investigation of Crossflow Separation on a Three-Caliber Tangent Ogive Cylinder," *AIAA Journal,* pp. 1223-1230, 1988.

[28] D. T. Greenwood, Principles of Dynamics, 2nd ed., Upper Saddle River: Prentice hall, 1988.

Appendix A: Vector Operations

Appendix A defines operators used in terms of vector operations. All operations are assumed to be taken with respect to an inertially fixed rectangular coordinate system. All vectors are column vectors. Vectors and matrices are indicated by bold font.

1) Cross Product

The cross product, defined for two vectors $\boldsymbol{a}$, $\boldsymbol{b} \in \mathbb{R}^3$, is defined as

$$\boldsymbol{a} \times \boldsymbol{b} = \begin{vmatrix} \hat{\boldsymbol{e}}_1 & \hat{\boldsymbol{e}}_2 & \hat{\boldsymbol{e}}_3 \\ a_1 & a_2 & a_3 \\ b_1 & b_2 & b_3 \end{vmatrix} \tag{A.1}$$

where $|\square|$ represents the determinant of the given matrix.

2) Gradient Operator "∇"

The gradient operator ∇ elevates the rank of the tensor being operated on by 1. The gradient can be represented as a vector as

$$\nabla \equiv \left[\frac{\partial}{\partial x}, \frac{\partial}{\partial y}, \frac{\partial}{\partial z}\right]^T \tag{A.2}$$

where superscript T means transpose.

The gradient of a scalar function $f = f(x, y, z)$ results in a vector (tensor of rank 1) and describes how $f(x, y, z)$ changes in each coordinate direction. It is defined as

$$\nabla f = \left[\frac{\partial}{\partial x}, \frac{\partial}{\partial y}, \frac{\partial}{\partial z}\right]^T f = \left[\frac{\partial f}{\partial x}, \frac{\partial f}{\partial y}, \frac{\partial f}{\partial z}\right]^T \tag{A.3}$$

The gradient of a vector function given as

$$\boldsymbol{f} = \left[f_x(x, y, z), f_y(x, y, z), f_z(x, y, z)\right]^T \tag{A.4}$$

yields the Jacobian matrix $J(x, y, z)$, a tensor of rank 2 defined to be

$$\nabla \boldsymbol{f} \equiv \begin{bmatrix} \frac{\partial f_x}{\partial x} & \frac{\partial f_x}{\partial y} & \frac{\partial f_x}{\partial z} \\ \frac{\partial f_y}{\partial x} & \frac{\partial f_y}{\partial y} & \frac{\partial f_y}{\partial z} \\ \frac{\partial f_z}{\partial x} & \frac{\partial f_z}{\partial y} & \frac{\partial f_z}{\partial z} \end{bmatrix} = J(x, y, z) \tag{A.5}$$

3) Divergence Operator

The dot operator, " $\cdot$ ", is used to determine the divergence of vectors and matrices. It contracts the rank of the tensor being operated on by 1. The divergence of a vector function such as (A.4) is defined to be

$$\begin{aligned} \text{div}\boldsymbol{f} = \nabla \cdot \boldsymbol{f} &= \left[\frac{\partial}{\partial x}, \frac{\partial}{\partial y}, \frac{\partial}{\partial z}\right]^T \cdot \left[f_x, f_y, f_z\right] \\ &= \frac{\partial f_x}{\partial x} + \frac{\partial f_y}{\partial y} + \frac{\partial f_z}{\partial z}. \end{aligned} \tag{A.6}$$

The divergence of a vector field $\boldsymbol{f}$ represents the extent to which the field acts as a source or sink. For a vector field $\boldsymbol{V}$ representing fluid velocity

$$\nabla \cdot \boldsymbol{V} = \frac{1}{\delta V} \frac{D(\delta V)}{Dt} \tag{A.7}$$

where $\frac{D}{Dt}$ is the total derivative with respect to time and δV is a differential volume in the fluid, the divergence of the velocity field represents the proportionate rate of change of volume (δV) of the fluid. The total derivative is formally defined as

$$\frac{D(\square)}{Dt} = \frac{\partial(\square)}{\partial t} + \boldsymbol{V} \cdot \nabla(\square) \tag{A.8}$$

and the first term represents the local derivative and the second represents the convective derivative. Together the total derivative expresses how the argument $(\square)$ changes with respect to space and time. Often times this is used in the Lagrangian perspective of fluid flows, where the observer travels with the fluid.

4) Curl Operator

The curl operator is used to define the curl of a vector and describes the rotation of a vector field such as $\boldsymbol{f}$ and is given by

$$curl\ \boldsymbol{f} = \nabla \times \boldsymbol{f} = \begin{vmatrix} \hat{\boldsymbol{e}}_1 & \hat{\boldsymbol{e}}_2 & \hat{\boldsymbol{e}}_3 \\ \dfrac{\partial}{\partial x} & \dfrac{\partial}{\partial y} & \dfrac{\partial}{\partial z} \\ f_x & f_y & f_z \end{vmatrix} \tag{A.9}$$

The curl of the velocity field $\boldsymbol{V}$ equals the vorticity $\boldsymbol{\Omega}$ of a given point in the flow. The vorticity is twice the instantaneous angular velocity at any given point such that

$$\nabla \times \boldsymbol{V} = \boldsymbol{2\omega} \tag{A.10}$$

where $\boldsymbol{\omega}$ is the instantaneous angular velocity at the given point.

5) Laplacian Operator "∇^2"

The Laplacian operator is the divergence of the gradient such that

$$\nabla^2 \boldsymbol{f}(x, y, z) = \nabla \cdot \nabla \boldsymbol{f}(x, y, z) \tag{A.11}$$

Appendix B: Summation Notation

Often times it is easier to represent operations via summation notation (Einstein or index notation). The following is a brief overview of summation notation, where summation is applied over repeated (dummy) indices.

1. Gradient Operator "∇"

   In summation notation, the gradient of a scalar function is given as

$$\nabla f \equiv \frac{\partial f}{\partial x_i}\hat{\boldsymbol{e}}_i \tag{B.1}$$

The gradient of a vector (still yielding the Jacobian matrix) is given as

$$\nabla \boldsymbol{f} \equiv \frac{\partial f_i}{\partial x_j}\hat{\boldsymbol{e}}_i\hat{\boldsymbol{e}}_j. \tag{B.2}$$

2. Dot Operator " $\cdot$ "

   In summation notation, the divergence of a vector is

$$\nabla \cdot \boldsymbol{f} \equiv \frac{\partial f_i}{\partial x_i}. \tag{B.3}$$

3. Curl Operator " $\times$ "

   In summation notation, the curl of a vector is

$$\nabla \times \boldsymbol{V} = \epsilon_{ijk}\frac{\partial \boldsymbol{V}_k}{\partial x_j}\hat{\boldsymbol{e}}_i \tag{B.4}$$

where ϵ_{ijk} is the Levi-Civita symbol defined as

$$\epsilon_{ijk} = \begin{cases} 0 & i = j, or\ j = k, or\ k = i \\ +1 & (i,j,k) \in \{(1,2,3),(2,3,1),(3,1,2)\} \\ -1 & (i,j,k) \in \{(1,3,2),(2,1,3),(3,2,1)\} \end{cases} \tag{B.5}$$

4. Laplacian Operator "∇^2"

In summation notation the Laplacian is given as

$$\nabla^2 \boldsymbol{f} = \frac{\partial^2 f_i}{\partial x_j \partial x_j} \boldsymbol{e}_i \tag{B.6}$$

5. Kronecker delta

The Kronecker delta is often used with summation notation and is defined over indices such that

$$\delta_{ij} = \begin{cases} 1 & i = j \\ 0 & i \neq j \end{cases} \tag{B.7}$$

Appendix C: Kirchhoff's Equations of Motion

The following is the rough derivation of the equations of motion of a rigid body in an ideal fluid. The derivation follows closely the derivation of Milne-Thompson [12]. All vectors correspond to Figure 1-3.

1. Kinetic Energy of the Liquid

The kinetic energy of the liquid is given by

$$T_L = -\frac{1}{2}\oiint_S \phi \nabla \cdot d\boldsymbol{S} \tag{C.1}$$

where $\phi = \phi(\boldsymbol{r}, t)$ and $\boldsymbol{S}$ is vector pointing normal to the surface of the body representing the magnitude of a differential area dS. The integral is taken over just the surface of the body, and represents the kinetic energy of all fluid outside the body (the region outside the body extends to infinity). For full derivation see [14] pg 302.

2. Kinetic Energy of the Solid

The kinetic energy of the solid is given by

$$T_S = \frac{1}{2}\oiiint_V \sigma\left[\mathbf{v}_i + \left(\boldsymbol{\omega}_i^{b/i} \times \mathbf{r}_i\right)\right]^2 d\tau \tag{C.2}$$

where σ is the density of the solid, O is the origin of the inertially fixed reference frame, O' is the origin of the body fixed frame, $\mathbf{r}_i$ is the vector from the origin O to O', $\mathbf{v}_i$ is the velocity of O', V is the volume of the body, and $\boldsymbol{\omega}_i^{b/i}$ is the angular velocity of the body fixed frame. For full derivation see [12] pg 523.

3. Rate of Change of the Momentum

The impulse (see [14] pg 247 for full definition) is an infinitesimally small change in linear and angular momentum. Assume the total kinetic energy of the system given by

$$T = T_S + T_L \tag{C.3}$$

is initially zero, and that the motion of the fluid is due completely to the motion of the body. Also, assume that the body is brought from rest into motion by an impulse wrench[22]. The rate of change of the momentum assuming all vectors are given in the inertial reference frame (denoted by subscript i) is given by

[22] An impulse wrench is a force moment couple $(\mathbf{F}, \mathbf{L})$ applied to the body for an infinitesimal amount of time.

$$\frac{{}^{i}d\boldsymbol{\xi}_i}{dt} = \mathbf{F}_i \tag{C.4}$$

$$\frac{{}^{i}d\boldsymbol{\lambda}_i}{dt} = \mathbf{L}_i \tag{C.5}$$

are identically Eulers equations of motion where $\boldsymbol{\xi}_i$ is the linear momentum and $\boldsymbol{\lambda}_i$ is the angular momentum taken about O (note: derivatives are taken with respect to the inertial frame). Assuming the origin O and O' are initially coincident and that the vectors $\boldsymbol{\xi}$ and $\boldsymbol{\lambda}$ are given in the body frame (denoted by the subscript b), the rate of change of the unit vectors in the body frame $\mathcal{F}_b$ needs to be taken into account via the transport theorem given by

$$\frac{{}^{i}d\boldsymbol{a}_b}{dt} = \frac{{}^{b}\partial\boldsymbol{a}_b}{\partial t} + \boldsymbol{\omega}_b^{b/i} \times \boldsymbol{a}_b \tag{C.6}$$

This leads to the equations of motion of the following form

$$\frac{{}^{i}d\boldsymbol{\xi}_b}{dt} = \frac{{}^{b}\partial\boldsymbol{\xi}_b}{\partial t} + \boldsymbol{\omega}_b^{b/i} \times \boldsymbol{\xi}_b = \mathbf{F}_b \tag{C.7}$$

$$\frac{{}^{i}d\boldsymbol{\lambda}_b}{dt} = \frac{{}^{b}\partial\boldsymbol{\lambda}_b}{\partial t} + \boldsymbol{\omega}_b^{b/i} \times \boldsymbol{\lambda}_b + \mathbf{v}_b \times \boldsymbol{\xi}_b = \mathbf{L}_b \tag{C.8}$$

where the term $\mathbf{v}_b \times \boldsymbol{\xi}_b$ comes from the fact that the angular momentum is taken about the point O. If it had been taken about O' this term would equal zero (note: some may refer to angular momentum defined in this way as "moment of momentum," and "angular momentum" when the momentum is measured about O').

4. Kirchhoff's Equations

The work done by a force-wrench over an infinitesimal time (the impulse) equals the change in kinetic energy of the system[23]. Using Euler's Theorem of Homogeneous Functions of degree 2 shown below

$$\mathbf{v}_b \frac{\partial T}{\partial \mathbf{v}_b} + \boldsymbol{\omega}_b^{b/i} \frac{\partial T}{\partial \boldsymbol{\omega}_b^{b/i}} = 2T \tag{C.9}$$

[23] $\delta W = \mathbf{F}_b \cdot (\mathbf{v}_b \delta t) + \mathbf{L}_b \cdot \left(\boldsymbol{\omega}_b^{b/i} \delta t\right) = \mathbf{v}_b \cdot \delta\boldsymbol{\xi} + \boldsymbol{\omega}_b^{b/i} \cdot \delta\boldsymbol{\omega}_b^{b/i} = \delta T$ where δW W is the work done one the system and $\mathbf{v}_b \cdot \delta\boldsymbol{\xi} + \boldsymbol{\omega}_b^{b/i} \cdot \delta\boldsymbol{\omega}_b^{b/i}$ is a homogeneous linear function. (###This NEEDS clarification###)

where T is an arbitrary scalar function of $\mathbf{v}$ and $\boldsymbol{\omega}$, and $\mathbf{v}$ and $\boldsymbol{\omega}$ are two independent vectors, one can show that

$$\boldsymbol{\xi} = \frac{\partial T}{\partial \mathbf{v}}, \quad \boldsymbol{\lambda} = \frac{\partial T}{\partial \boldsymbol{\omega}} \tag{C.10}$$

Substituting the relations given by Equation (C.9) into equations (C.7) and (C.8), one arrives at Kirchhoff's Equations of Motion for a rigid body in an infinite fluid shown below

$$^{i}\frac{d}{dt}\left(\frac{\partial T}{\partial \mathbf{v}_b}\right) = {}^{b}\frac{\partial}{\partial t}\left(\frac{\partial T}{\partial \mathbf{v}_b}\right) + \boldsymbol{\omega}_b^{b/i} \times \frac{\partial T}{\partial \mathbf{v}_b} = \mathbf{F} \tag{C.11}$$

$$^{i}\frac{d}{dt}\left(\frac{\partial T}{\partial \boldsymbol{\omega}_b^{b/i}}\right) = {}^{b}\frac{\partial}{\partial t}\left(\frac{\partial T}{\partial \boldsymbol{\omega}_b^{b/i}}\right) + \boldsymbol{\omega}_b^{b/i} \times \frac{\partial T}{\partial \boldsymbol{\omega}_b^{b/i}} + \mathbf{v}_b \times \frac{\partial T}{\partial \mathbf{v}_b} = \mathbf{L} \tag{C.12}$$

where T is the total kinetic energy

Appendix D: Direction Cosines

The direction cosines $\{l, m, n\}$ are related by the angles $\{\alpha, \beta, \gamma\}$ formed between the three body axis $\{\hat{\boldsymbol{b}}_1, \hat{\boldsymbol{b}}_2, \hat{\boldsymbol{b}}_3\}$ as shown below

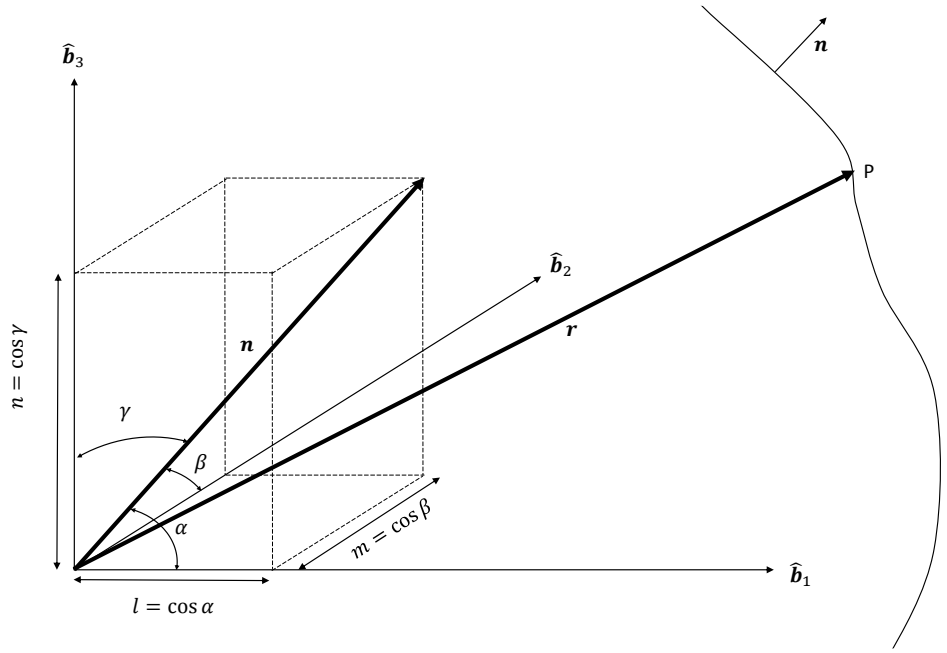

Figure D-1: Diagram of direction cosines.

where

$$l^2 + m^2 + n^2 = cos^2\,\alpha + cos^2\,\beta + cos^2\,\gamma = 1 = \|\boldsymbol{n}\|_2$$

And

$$l\hat{\boldsymbol{b}}_1 + m\hat{\boldsymbol{b}}_2 + n\hat{\boldsymbol{b}}_3 = n_x\hat{\boldsymbol{b}}_1 + n_y\hat{\boldsymbol{b}}_2 + n_z\hat{\boldsymbol{b}}_3 = \boldsymbol{n} \tag{D.1}$$

where $\|\square\|_2$ is the Euclidean norm and $\boldsymbol{n}$ is a unit vector pointing normal to the body's surface. As is shown in Figure D-1, l, m, and n are equivalent to the magnitudes of the vector $\boldsymbol{n}$ projected onto the $\hat{\boldsymbol{b}}_1$, $\hat{\boldsymbol{b}}_2$, and $\hat{\boldsymbol{b}}_3$ axes respectively

With this in mind (1.28) will be derived. Take any point P lying on the surface of the body such that it satisfies (1.22) and

$$\boldsymbol{r} = x\hat{\boldsymbol{b}}_1 + y\hat{\boldsymbol{b}}_2 + z\hat{\boldsymbol{b}}_3 \tag{D.2}$$

Taking the derivative of $\boldsymbol{r}$ with respect to time

$$\dot{\boldsymbol{r}} = {}^{i}\frac{d}{dt}\boldsymbol{r} = {}^{b}\frac{\partial}{\partial t}\boldsymbol{r} + \boldsymbol{\omega} \times \boldsymbol{r} = u\hat{\boldsymbol{b}}_1 + v\hat{\boldsymbol{b}}_2 + w\hat{\boldsymbol{b}}_3 + \hat{\boldsymbol{b}}_1(qz - ry) - \hat{\boldsymbol{b}}_2(pz - xr) + \hat{\boldsymbol{b}}_3(py - qx)$$
$$\updownarrow$$
$$\dot{\boldsymbol{r}} = (u + qz - ry)\hat{\boldsymbol{b}}_1 + (v + \dot{rx} - pz)\hat{\boldsymbol{b}}_2 + (w + py - qx)\hat{\boldsymbol{b}}_3 = \boldsymbol{V}_s \tag{D.3}$$

The boundary condition given by (1.21), which enforces the no penetration condition across the surface of the body, can be rewritten as

$$\frac{\partial \phi}{\partial n} = grad\ \phi \cdot \boldsymbol{n} = \boldsymbol{V} \cdot \boldsymbol{n} = \boldsymbol{V}_s \cdot \boldsymbol{n}$$

$$= l(u + qz - ry) + m(v + rx - pz) + n(w + py - qx) \tag{D.4}$$

It is clear that in order to satisfy (1.27) and (D.4) such that

$$\frac{\partial \phi}{\partial n} = u\frac{\partial \varphi_1}{\partial n} + v\frac{\partial \varphi_2}{\partial n} + w\frac{\partial \varphi_3}{\partial n} + p\frac{\partial \varphi_4}{\partial n} + q\frac{\partial \varphi_5}{\partial n} + r\frac{\partial \varphi_6}{\partial n} \tag{D.5}$$

the relations given by (1.28) must be true.

Appendix E: Ideal Added Mass Coefficients

The following table explicitely gives the added mass coefficients, which are functions of the body's surface and velocity potential of the fluid ϕ.

Table E-1: Added mass coefficients

$X_{\dot{u}} = \iint_S \left(\varphi_1 \frac{\partial \varphi_1}{\partial n}\right) dS$	$Y_{\dot{w}} = \frac{1}{2}\iint_S \left(\varphi_2 \frac{\partial \varphi_3}{\partial n} + \varphi_3 \frac{\partial \varphi_2}{\partial n}\right) dS$	$Z_{\dot{r}} = \frac{1}{2}\iint_S \left(\varphi_3 \frac{\partial \varphi_6}{\partial n} + \varphi_6 \frac{\partial \varphi_3}{\partial n}\right) dS$
$X_{\dot{v}} = \frac{1}{2}\iint_S \left(\varphi_1 \frac{\partial \varphi_2}{\partial n} + \varphi_2 \frac{\partial \varphi_1}{\partial n}\right) dS$	$Y_{\dot{p}} = \frac{1}{2}\iint_S \left(\varphi_2 \frac{\partial \varphi_4}{\partial n} + \varphi_4 \frac{\partial \varphi_2}{\partial n}\right) dS$	$K_{\dot{p}} = \iint_S \left(\varphi_4 \frac{\partial \varphi_4}{\partial n}\right) dS$
$X_{\dot{w}} = \frac{1}{2}\iint_S \left(\varphi_1 \frac{\partial \varphi_3}{\partial n} + \varphi_3 \frac{\partial \varphi_1}{\partial n}\right) dS$	$Y_{\dot{q}} = \frac{1}{2}\iint_S \left(\varphi_2 \frac{\partial \varphi_5}{\partial n} + \varphi_5 \frac{\partial \varphi_2}{\partial n}\right) dS$	$K_{\dot{q}} = \frac{1}{2}\iint_S \left(\varphi_4 \frac{\partial \varphi_5}{\partial n} + \varphi_5 \frac{\partial \varphi_4}{\partial n}\right) dS$
$X_{\dot{p}} = \frac{1}{2}\iint_S \left(\varphi_1 \frac{\partial \varphi_4}{\partial n} + \varphi_4 \frac{\partial \varphi_1}{\partial n}\right) dS$	$Y_{\dot{r}} = \frac{1}{2}\iint_S \left(\varphi_2 \frac{\partial \varphi_6}{\partial n} + \varphi_6 \frac{\partial \varphi_2}{\partial n}\right) dS$	$K_{\dot{r}} = \frac{1}{2}\iint_S \left(\varphi_4 \frac{\partial \varphi_6}{\partial n} + \varphi_6 \frac{\partial \varphi_4}{\partial n}\right) dS$
$X_{\dot{q}} = \frac{1}{2}\iint_S \left(\varphi_1 \frac{\partial \varphi_5}{\partial n} + \varphi_5 \frac{\partial \varphi_1}{\partial n}\right) dS$	$Z_{\dot{w}} = \iint_S \left(\varphi_3 \frac{\partial \varphi_3}{\partial n}\right) dS$	$M_{\dot{q}} = \iint_S \left(\varphi_5 \frac{\partial \varphi_5}{\partial n}\right) dS$
$X_{\dot{r}} = \frac{1}{2}\iint_S \left(\varphi_1 \frac{\partial \varphi_6}{\partial n} + \varphi_6 \frac{\partial \varphi_1}{\partial n}\right) dS$	$Z_{\dot{p}} = \frac{1}{2}\iint_S \left(\varphi_3 \frac{\partial \varphi_4}{\partial n} + \varphi_4 \frac{\partial \varphi_3}{\partial n}\right) dS$	$K_{\dot{r}} = \frac{1}{2}\iint_S \left(\varphi_5 \frac{\partial \varphi_6}{\partial n} + \varphi_6 \frac{\partial \varphi_5}{\partial n}\right) dS$
$Y_{\dot{v}} = \iint_S \left(\varphi_2 \frac{\partial \varphi_2}{\partial n}\right) dS$	$Z_{\dot{q}} = \frac{1}{2}\iint_S \left(\varphi_3 \frac{\partial \varphi_5}{\partial n} + \varphi_5 \frac{\partial \varphi_3}{\partial n}\right) dS$	$N_{\dot{r}} = \iint_S \left(\varphi_6 \frac{\partial \varphi_6}{\partial n}\right) dS$

The above relations can be simplified using Greens theorem of the second form shown below

$$\iiint_R \left(\varphi_i \nabla^2 \varphi_j - \varphi_j \nabla^2 \varphi_i\right) d\tau = \iint_{S+\Sigma} \left(\varphi_i \frac{\partial \varphi_j}{\partial n} - \varphi_j \frac{\partial \varphi_i}{\partial n}\right) dS \qquad \text{(E.1)}$$

where R is the region exterior to the body extending from the body's surface S to Σ. Allowing Σ to approach infinity and noting that φ_i and φ_j are both harmonic functions of position satisfying Laplace's equation one finds

$$\iint_S \varphi_i \frac{\partial \varphi_j}{\partial n} dS = \iint_S \varphi_j \frac{\partial \varphi_i}{\partial n} dS \qquad \text{(E.2)}$$

This allows for the simplification of the relations given in Table E-1. For example, $X_{\dot{v}}$ becomes $X_{\dot{v}} = \iint_S \varphi_1 \frac{\partial \varphi_2}{\partial n} dS$.

Appendix F: Added Mass and Damping Matrices

This section describes the matrices seen in the state space representation of the body's equations of motion though a fluid when $\boldsymbol{\eta}$ is expressed in the body frame. It is also assumed the origin of the body frame coincides with the center of mass of the body.

1. Mass Matrix $\mathbf{M}$

The mass matrix is the combination of the rigid body mass matrix $\mathbf{M}_{RB}$ and the added mass matrix $\mathbf{M}_{\mathrm{A}}$ defined as

$$\mathbf{M}_{\mathrm{RB}} = \begin{bmatrix} \mathrm{m}\mathbf{I}_{3\times3} & \mathbf{0}_{3\times3} \\ \mathbf{0}_{3\times3} & \mathbf{I} \end{bmatrix} \tag{F.1}$$

$$\mathbf{M}_{\mathrm{A}} = \begin{bmatrix} \boldsymbol{A}_{11} & \boldsymbol{A}_{12} \\ \boldsymbol{A}_{21} & \boldsymbol{A}_{22} \end{bmatrix} = \begin{bmatrix} \mathrm{X}_{\dot{u}} & \mathrm{X}_{\dot{v}} & \mathrm{X}_{\dot{w}} & \mathrm{X}_{\dot{p}} & \mathrm{X}_{\dot{q}} & \mathrm{X}_{\dot{r}} \\ \mathrm{Y}_{\dot{u}} & \mathrm{Y}_{\dot{v}} & \mathrm{Y}_{\dot{w}} & \mathrm{Y}_{\dot{p}} & \mathrm{Y}_{\dot{q}} & \mathrm{Y}_{\dot{r}} \\ \mathrm{Z}_{\dot{u}} & \mathrm{Z}_{\dot{v}} & \mathrm{Z}_{\dot{w}} & \mathrm{Z}_{\dot{p}} & \mathrm{Z}_{\dot{q}} & \mathrm{Z}_{\dot{r}} \\ \mathrm{K}_{\dot{u}} & \mathrm{K}_{\dot{v}} & \mathrm{K}_{\dot{w}} & \mathrm{K}_{\dot{p}} & \mathrm{K}_{\dot{q}} & \mathrm{K}_{\dot{r}} \\ \mathrm{M}_{\dot{u}} & \mathrm{M}_{\dot{v}} & \mathrm{M}_{\dot{w}} & \mathrm{M}_{\dot{p}} & \mathrm{M}_{\dot{q}} & \mathrm{M}_{\dot{r}} \\ \mathrm{N}_{\dot{u}} & \mathrm{N}_{\dot{v}} & \mathrm{N}_{\dot{w}} & \mathrm{N}_{\dot{p}} & \mathrm{N}_{\dot{q}} & \mathrm{N}_{\dot{r}} \end{bmatrix} \tag{F.2}$$

such that

$$\mathbf{M} = \mathbf{M}_{RB} - \mathbf{M}_{\mathrm{A}} \tag{F.3}$$

and $\mathbf{I}_{3\times3}$ is the identity matrix. Note that for a body moving through an ideal fluid, the added mass matrix is symmetric such that

$$\mathbf{M}_{\mathrm{A}} = \mathbf{M}_{A}^{T} = \begin{bmatrix} \mathrm{X}_{\dot{u}} & \mathrm{X}_{\dot{v}} & \mathrm{X}_{\dot{w}} & \mathrm{X}_{\dot{p}} & \mathrm{X}_{\dot{q}} & \mathrm{X}_{\dot{r}} \\ \mathrm{X}_{\dot{v}} & \mathrm{Y}_{\dot{v}} & \mathrm{Y}_{\dot{w}} & \mathrm{Y}_{\dot{p}} & \mathrm{Y}_{\dot{q}} & \mathrm{Y}_{\dot{r}} \\ \mathrm{X}_{\dot{w}} & \mathrm{Y}_{\dot{w}} & \mathrm{Z}_{\dot{w}} & \mathrm{Z}_{\dot{p}} & \mathrm{Z}_{\dot{q}} & \mathrm{Z}_{\dot{r}} \\ \mathrm{X}_{\dot{p}} & \mathrm{Y}_{\dot{p}} & \mathrm{Z}_{\dot{p}} & \mathrm{K}_{\dot{p}} & \mathrm{K}_{\dot{q}} & \mathrm{K}_{\dot{r}} \\ \mathrm{X}_{\dot{q}} & \mathrm{Y}_{\dot{q}} & \mathrm{Z}_{\dot{q}} & \mathrm{K}_{\dot{q}} & \mathrm{M}_{\dot{q}} & \mathrm{M}_{\dot{r}} \\ \mathrm{X}_{\dot{r}} & \mathrm{Y}_{\dot{r}} & \mathrm{Z}_{\dot{r}} & \mathrm{K}_{\dot{r}} & \mathrm{M}_{\dot{r}} & \mathrm{N}_{\dot{r}} \end{bmatrix} \tag{F.4}$$

Also, many references define the added mass matrix to be the negative of (F.4), and then define $\mathbf{M} = \mathbf{M}_{RB} + \mathbf{M}_{\mathrm{A}}$. The effect is the same either way; the inertia of the body is effectively increased by the added mass effect.

2. Coriolis Matrix $\mathbf{C}$

The matrix $\mathbf{C} = \mathbf{C}_{RB}(\boldsymbol{\eta}) + \mathbf{C}_{A}(\boldsymbol{\eta})$ is a combination of the rigid body centripetal matrix $\mathbf{C}_{RB}$ accounting for the moving reference frame, and a matrix $\mathbf{C}_{A}$ accounting for the nonlinear terms caused by a body moving through an ideal fluid both given as

$$\mathbf{C}_{RB}\left(\boldsymbol{\omega}^{b/i}\right) = \begin{bmatrix} m\boldsymbol{S}\left(\boldsymbol{\omega}^{b/i}\right) & 0_{3x3} \\ 0_{3x3} & -m\boldsymbol{S}\left(\mathbf{I}_b\boldsymbol{\omega}^{b/i}\right) \end{bmatrix} \tag{F.5}$$

$$\mathbf{C}_A(\boldsymbol{\eta}) = \begin{bmatrix} 0_{3x3} & -\boldsymbol{S}\left(\boldsymbol{A}_{11}\mathbf{v} + \boldsymbol{A}_{12}\boldsymbol{\omega}^{b/i}\right) \\ -\boldsymbol{S}\left(\boldsymbol{A}_{11}\mathbf{v} + \boldsymbol{A}_{12}\boldsymbol{\omega}^{b/i}\right) & -\boldsymbol{S}\left(\boldsymbol{A}_{21}\mathbf{v} + \boldsymbol{A}_{22}\boldsymbol{\omega}^{b/i}\right) \end{bmatrix} \tag{F.6}$$

such that

$$\mathbf{C} = \mathbf{C}_{RB} - \mathbf{C}_A \tag{F.7}$$

Here, $\mathbf{S}(\boldsymbol{\omega})$ is a scew symmetric matrix

$$\mathbf{S}(\boldsymbol{\omega}) = \begin{bmatrix} 0 & -\omega_3 & \omega_2 \\ \omega_3 & 0 & -\omega_1 \\ -\omega_2 & \omega_1 & 0 \end{bmatrix} \tag{F.8}$$

such that

$$\mathbf{S}(\boldsymbol{\omega})\boldsymbol{a} = \boldsymbol{\omega} \times \boldsymbol{a} \tag{F.9}$$

is the cross product between $\boldsymbol{\omega}$ and $\boldsymbol{a}$.

Appendix G: STAR-CCM+ Iterative Scheme

The following is an outline of the iterative technique employed by STAR-CCM+ to solve the linearized set of algebraic equations. If we had assumed both incompressible and invicid flow, the N-S equations would have been reduced to solving a single partial differential equation, namely Laplace's equation given in § 1.6.3. This equation is elliptic in nature, and can be solved in a straightforward manner using iterative relaxation techniques. With the assumption of viscous flow, the governing equations cannot be reduced in a similar fashion, and therefore all 3 equations must be solved simultaneously. The governing equations exhibit a mixed elliptic-parabolic behavior, and are not easily solved with standard iterative relaxation techniques. The pressure correction method, to be described shortly, transcends this difficulty through the SIMPLE, or Semi-Implicit Method for Pressure Linked Equations, algorithm. This method is combined with STAR-CCM's Algebraic Multigrid (AMG) solver and Gauss-Seidel's (GS) iterative method, both to be discussed, to completely solve the N-S equations.

The SIMPLE algorithm along with the AMG solver and GS iterative method are summarized as follows:

1. Intuitively guess the pressure field at the current time step *n*, denoted by p^*. Often times P^* is set to the current pressure field, $P^* = P^n$ where superscript n denotes the current time step.
2. Intuitively guess the velocity field to be used as the initial condition, $\boldsymbol{V}^{IC}$, to solve the momentum equations using the guessed pressure field P^*.
3. Solve the momentum equations for the velocity field $\boldsymbol{V}^* = [u^*, v^*, w^*]^{\mathrm{T}}$ using an AMG solver and the GS iterative method.
    a. The AMG solver essentially agglomerates cells to form progressively coarser mesh[24] levels. GS iterations are then used to solve the resulting linear equations on each mesh level. The solutions on the coarser meshes are interpolated back to the finer meshes through a process called prolongation. An example cycle is shown in Figure G-1. By coarsening the grid, low frequency errors are made into progressively higher frequency errors, which are generally damped out by GS iterations relatively quickly. The AMG solver is used solely to speed convergence.

[24] The algebraic multigrid solver coarsens the "mesh" by combining the coefficients from different mesh levels, as opposed to the geometric multigrid method (FAS) which coarsens the actual mesh.

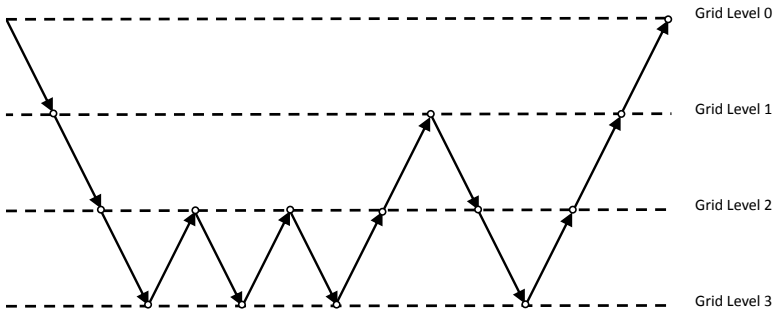

Figure G-1: F cycle for AMG solver where grid level 0 is the finest grid level and grid level 3 is the coarsest.

4. Determine how well the resulting velocity field satisfies the continuity equation.
    a. If satisfactory (i.e. the LHS of (1.94) is sufficiently close to zero) , set $p^{n+1} = p^*$ and $\boldsymbol{V}^{n+1} = \boldsymbol{V}^*$
    b. If not satisfactory, then correct p^* and $\boldsymbol{V}^*$ with correction terms p' and $\boldsymbol{V}'$, obtained from the continuity equation, such that

$$p^{corrected} = p^* + p' \tag{G.1}$$

$$\boldsymbol{V}^{IC} = \boldsymbol{V}^* + \boldsymbol{V}' \tag{G.2}$$

Set p^*=P^{corrected} and $\boldsymbol{V}^{IC} = \boldsymbol{V}^{corrected}$ and return to step 3.

Appendix H: Flow Topology

As explained in [25], the analysis of fluid flows via topological methods is not a means for predicting flow. Its utility is derived from its ability to describe the flow in a self-consistent and useful manner. What follows will be a brief introduction to some fundamental concepts in flow topology.

Flow topology is defined locally for a body over its planar surface, such that (ξ, η, ζ) is a general curvilinear coordinate system with ζ being directed outward normal to the surface of the body. The skin friction[25] field is then defined on this plane as

$$\boldsymbol{\tau}_w = (\tau_\xi, \tau_\eta) \tag{H.1}$$

where

$$\tau_\xi = \mu \left.\frac{\partial u_\xi}{\partial \zeta}\right|_w$$

$$\tau_\eta = \mu \left.\frac{\partial u_\eta}{\partial \zeta}\right|_w$$

and u_ξ and u_η are the velocity of the fluid in the ξ and η direction respectively, and the subscript w is understood as the wall. This field defines a continuous vector field of the shear stress over the surface of the body. One can then define skin friction lines in a similar manner to streamlines, as solutions to the following differential equation

$$\frac{dx}{\tau_\xi} = \frac{dy}{\tau_\eta} \tag{H.2}$$

In general, all points on the surface have one skin friction line passing through them. Points which have more than one skin friction line coinciding with the same point are called critical points, and are points where the shear stress goes to zero (i.e. $\tau_\xi = \tau_\eta = 0$).

H1 Critial Points

Critical point analysis used in this paper considers the behavior of the vector field near the critical points. These critical points can be divided into nodes and saddles, with nodes being further subdivided into nodal points and foci. See [25] for details on deriving the behavior of different types of critical points. In [25], he also explains how the planar topological theory can be extended to the three dimensional flow domain, where the streamlines defined by the velocity vector field of the flow are used instead of skin

[25] Skin friction field is what is used to derive the skin friction lines which are sometimes synonymously called limiting streamlines, however, this convention can sometimes be misleading. See [25] for details on the differences between skin friction line and limiting streamlines.

friction lines defined by the skin friction field. And because streamlines tend to coincide with skin friction lines as the wall is approached, intuitively it is conceivable that the critical points on the surface also coincide with those in the flow field.

The nodal point of attachment, N_A, (and node of separation, N_S, or stagnation node) is one type of critical point where the flow "attaches" to (or separates from) the surface of the. This type of node has an infinite number of skin friction lines common to the point. All these skin friction lines are tangential to a single line at the critical point. Examples of this type of node are shown in Figure H-1. If the skin friction lines are going away from the node, it is a nodal point of attachment. Likewise, if the skin friction lines are going towards the node, it is a nodal point of separation. In connection with the streamlines in the flow, a single streamline is associated with this point, whether it be a point of attachment or separation.

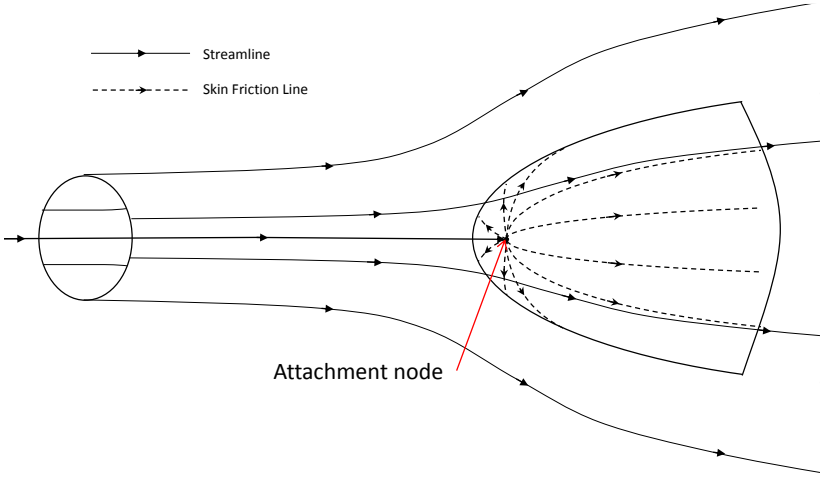

Figure H-1: Example node of attachment at front of spheroid at zero angle of attack. Node of separation looks the same with arrows in opposite direction.

The next major type of critical point is called a focus of attachment, F_A, (or separation, F_S). The only difference between a focus of attachment (or separation) and a node of attachment (or separation) is that the skin friction lines do not share a common tangency line as shown in Figure H-2.

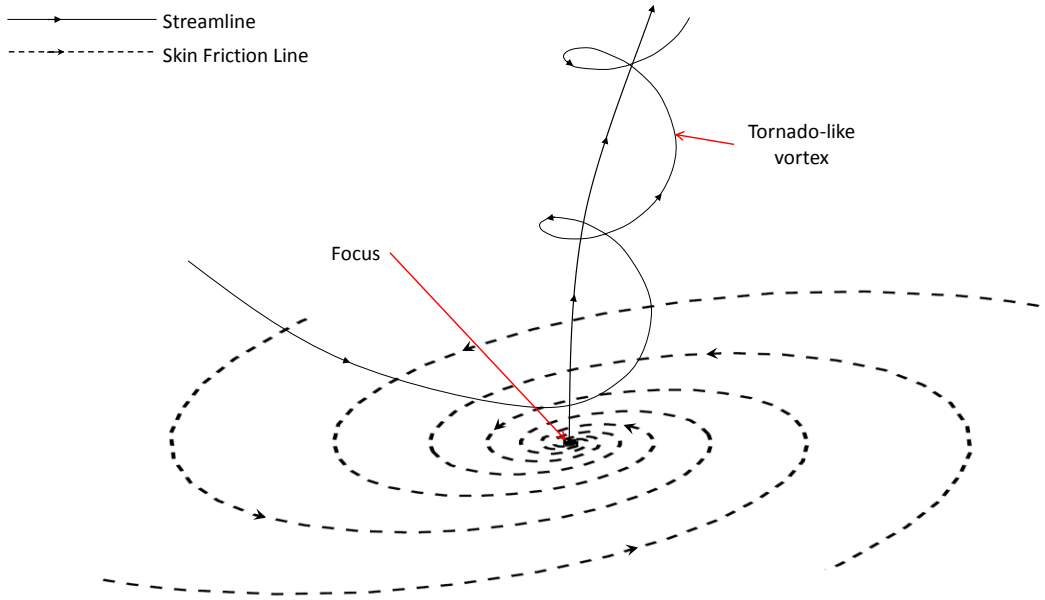

Figure H-2: Examples of focus of separation.

The final major critical point is the saddle of attachment, S_A,(and separation, S_S). This point has two (and only two) streamlines passing through it. Trajectories on one line are all pointing towards the critical point, and trajectories on the other line are all pointing away from the critical point. All other skin friction lines passing close to this critical point diverge away from it. The two lines crossing the critical point are referred to as separatrixes, as these lines form a barrier between skin friction lines on the other side of the separatrix. This line is often referred to as a line of separation as it is often associated with a separation surface (or attachment surface) in the fluid flow, with infinitely many streamlines attaching to (or separating from) that point. An example of this surface is shown in Figure H-3. This surface of separation can sometimes roll up and form vertical structures similar to tornados as shown in Figure H-4.

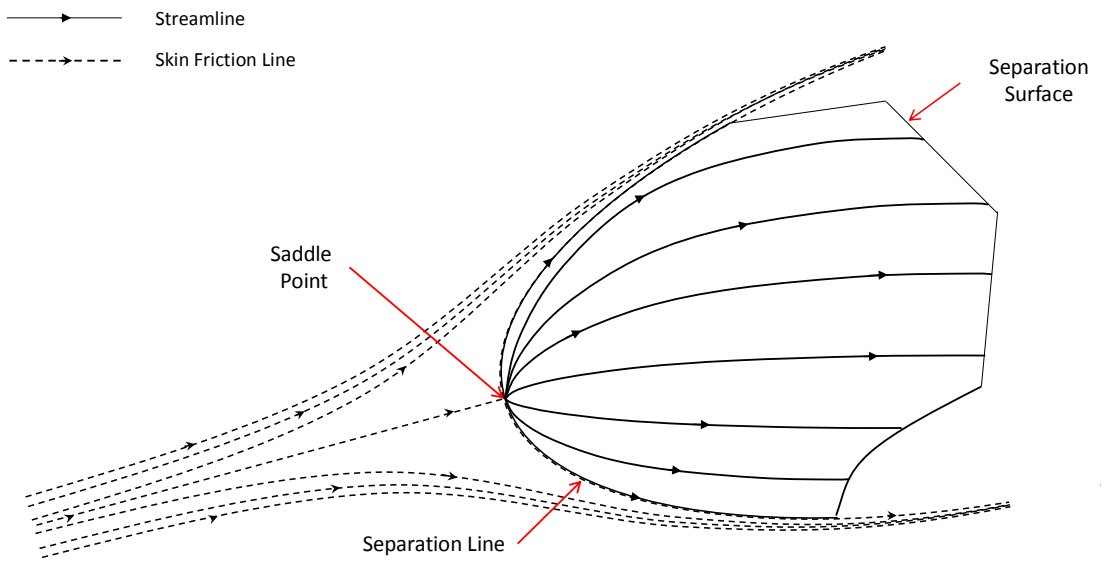

Figure H-3: Example of a saddle of separation. Saddle of attachment looks the same with arrows in opposite directions.

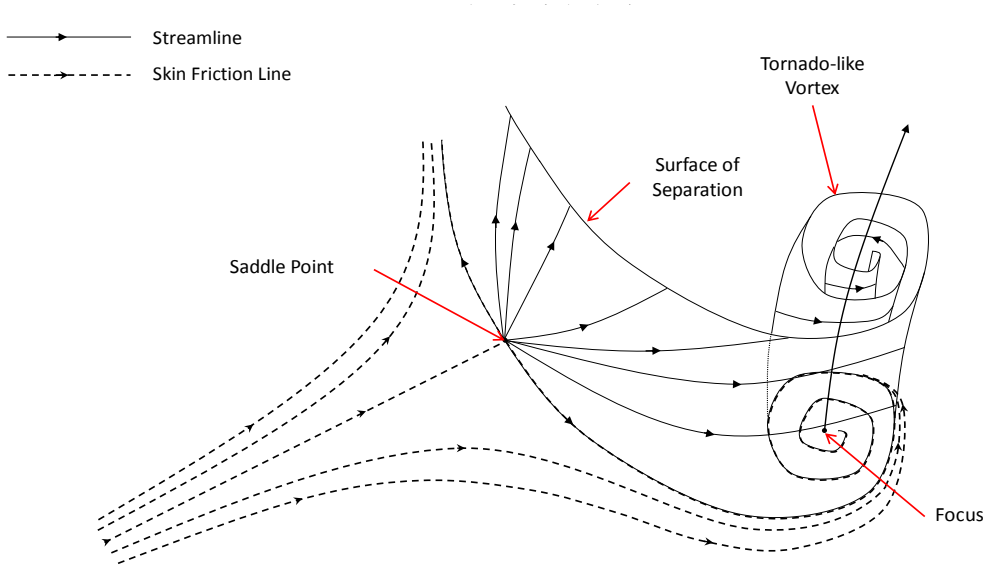

Figure H-4: Example surface of separation rolling up to form a tornado-like vortex.

Two special forms of separation are often observed when looking at flow over a spheroid. The first is seen when the spheroid is at zero angle of attack as shown in Figure 3-2. Here symmetry conditions allow for the formation of a singular line. As Chapman states in [9], this singular line is considered to be 'between' a node and a saddle. This line of separation causes a Toroidal vortex to form behind the body, like that shown in Figure H-5.

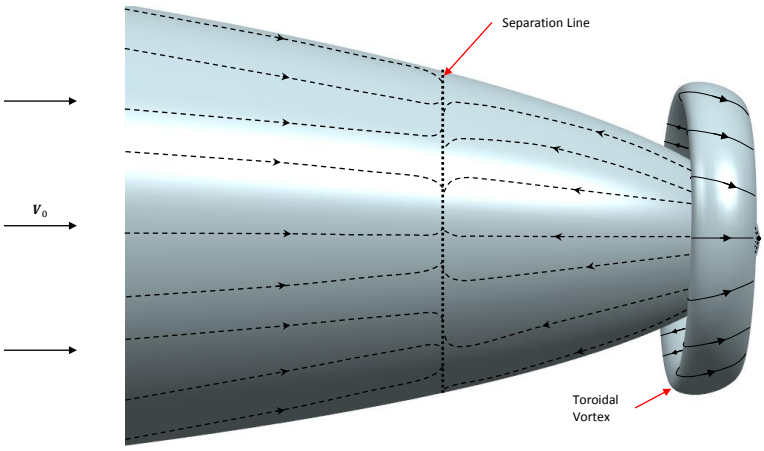

Figure H-5: Toroidal vortex forming behind spheroid at zero angle of attack.

The second type of separation seen with spheroids is what has come to commonly be called crossflow separation due to the appearance of topological features such as nodes and saddles in the crossflow plane as shown in Figure H-7. This type of separation has also been called "open" separation by Wang [10] and "local" separation by Tobak and Peake [26]. This type of separation form slowly over the body and no topological features are present on the surface of the body, making this type of separation extremely hard to concretely define. The only visual indicator of this type of separation is a convergence of the skin friction lines. The convergence line can also be used to indicate lines of attachment. As noted in [27], this line does not always indicate that the flow has separated.

H2 Cross Flow Separation

A very special type of separation is cross flow separation, because the start of this separation is not indicated by a critical point in the skin friction vector field. However, when the flow is projected onto a crossflow plane, a plane whose normal is parallel to the major axis of a spheroid, critical points do appear.

Figure H-6 shows the streamlines over a spheroid at $\alpha = 2°$. The cross flow plane (A-A) is shown to the right. The flow in the cross flow plane is similar to what would be expected for 2D ideal flow over a circular cylinder; two critical points. A half-saddle of attachment (S'_A) (indicated by the " $'$ ") at the leading edge and a half-saddle of separation (S'_S) at the trailing edge. It needs to be iterated that this 2D crossflow plane does not fully represent the 3D flow, and hence is given the distinction of being a "half" saddle. For example, the flow does not actually attach at S'_A on the bottom of the spheroid. It actually attaches at a node of attachment at the nose.

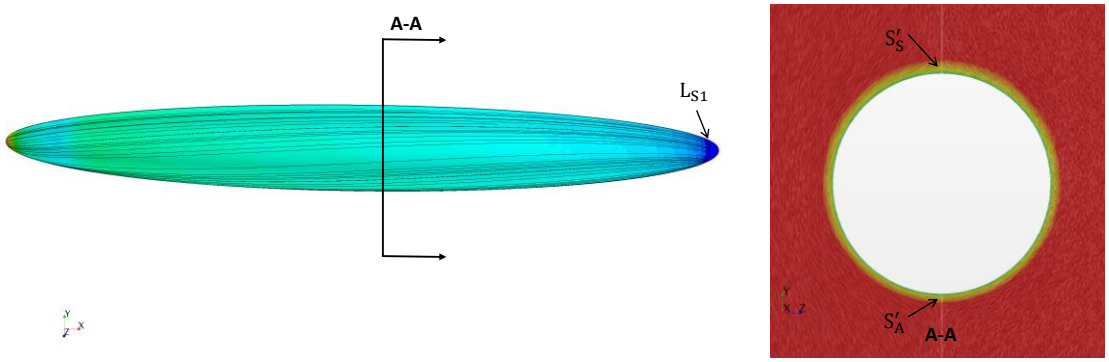

Figure H-6: Left: spheroid at $\boldsymbol{\alpha = 2°}$ showing skin friction lines of flow over the body. Right: cross flow plane at section A-A of spheroid showing line convolution integrals of the velocity vector field.

When an 8:1 spheroid reaches $\alpha = 2°$ cross flow separation becomes clear, as shown in Figure H-7. The flow separates along the line CF_{S1} associated with the half-saddle of separation S'_{S1}, circulates in a vortex structure V_1, and finally reattaches at the half-saddle of attachment S'_{A1}. The vortex V_2 is created from the vorticity in the boundary layer before separation, similar to the mechanisms which cause vortex structures to form behind a circular cylinder and the toroidal vortex behind a spheroid at zero angle of attack. In Figure H-7 V_2 is rotating counterclockwise when viewed in the direction A-A.

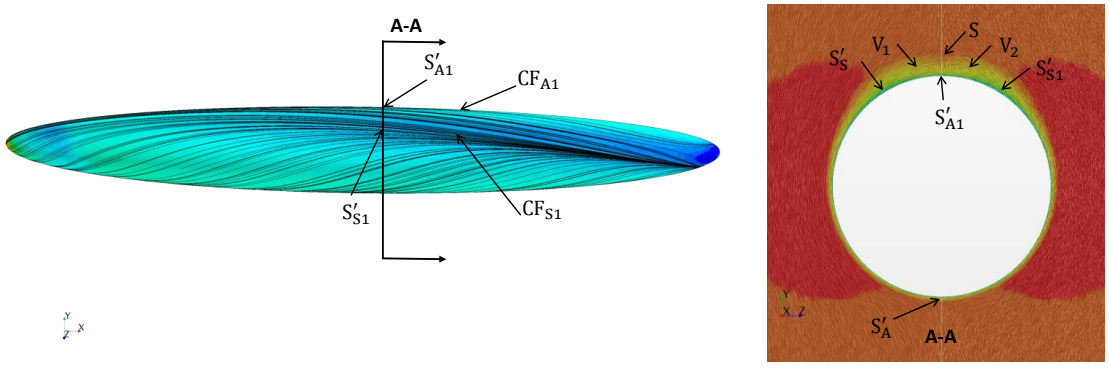

Figure H-7: Left: spheroid at $\boldsymbol{\alpha = 10°}$ showing skin friction lines of flow over the body. Right: cross flow plane at section A-A of spheroid showing line convolution integrals of the velocity vector field.

If the intensity of the cross flow separation is increased by increasing the angle of attack, secondary separation can occur, as shown in Figure H-8. Larger angles of attack lead to the generation of larger vortical structures which create this secondary flow. Looking at the cross flow plane, the flow separates at S'_{S1}, circulates in the counterclockwise direction in V_3, and reattaches at S'_{A1} before separating at S'_{S2}, and circulating in the clockwise direction in V_4, finally attaching at S'_{A2}. Because the cross flow separation occurs sooner when at larger angles of attack, more momentum is lost in the flow than would otherwise be lost if the flow separated later, which enables the secondary separation at S'_{S2}.

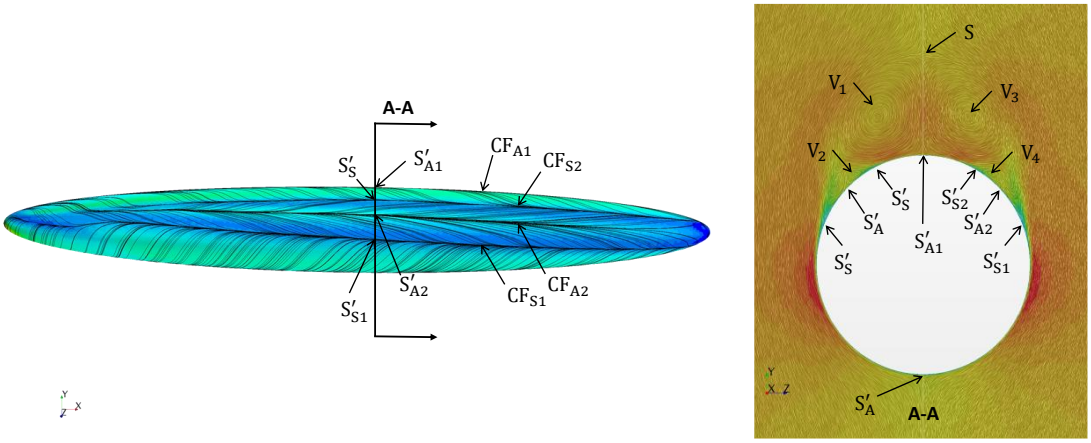

Figure H-8: Left: spheroid at $\boldsymbol{\alpha = 30°}$ showing skin friction lines of flow over the body. Right: cross flow plane at section A-A of spheroid showing line convolution integrals of the velocity vector field.

Appendix I: Model Coefficients and Goodness of Fit's

1. Linear Coefficients

Table I-1: Nondimensional Added Mass

$Z'_{\dot{w}}$

		Non-dimensional Amplitude						
		0.05	0.10	0.20	0.30	0.40	0.50	Δ
Non Dim Frequency	0.05	-0.0075	-0.0074	-0.0073	-0.0071	-0.0069	-0.0066	9.3708E-04
	0.10	-0.0074	-0.0073	-0.0069	-0.0063	-0.0056	-0.0050	2.4252E-03
	0.20	-0.0073	-0.0069	-0.0058	-0.0047	-0.0040	-0.0035	3.8165E-03
	0.30	-0.0072	-0.0066	-0.0050	-0.0041	-0.0036	-0.0033	3.9020E-03
	0.40	-0.0072	-0.0064	-0.0047	-0.0040	-0.0037	-0.0035	3.6947E-03
	0.50	-0.0072	-0.0063	-0.0047	-0.0042	-0.0040	-0.0037	3.4743E-03
	Δ	3.5549E-04	1.1721E-03	2.5822E-03	3.0507E-03	3.2702E-03	3.2980E-03	Max-Min

Table I-2: Nondimensional Linear Damping

Z'_{w}

		Non-dimensional Amplitude						
		0.05	0.10	0.20	0.30	0.40	0.50	Δ
Non Dim Frequency	0.05	-0.0040	-0.0041	-0.0043	-0.0047	-0.0052	-0.0058	1.8918E-03
	0.10	-0.0041	-0.0043	-0.0051	-0.0065	-0.0084	-0.0105	6.4514E-03
	0.20	-0.0041	-0.0048	-0.0078	-0.0120	-0.0163	-0.0205	1.6406E-02
	0.30	-0.0041	-0.0054	-0.0110	-0.0177	-0.0239	-0.0296	2.5478E-02
	0.40	-0.0040	-0.0059	-0.0146	-0.0234	-0.0309	-0.0375	3.3574E-02
	0.50	-0.0037	-0.0066	-0.0186	-0.0288	-0.0373	-0.0450	4.1217E-02
	Δ	3.8656E-04	2.5503E-03	1.4313E-02	2.4086E-02	3.2095E-02	3.9118E-02	Max-Min

Table I-3: Mean Square Error

MSE

		Non-dimensional Amplitude						
		0.05	0.10	0.20	0.30	0.40	0.50	Δ
Non Dim Frequency	0.05	6.10E-14	8.22E-13	2.23E-11	2.08E-10	1.12E-09	4.32E-09	4.3156E-09
	0.10	3.24E-13	1.47E-11	9.46E-10	1.10E-08	5.56E-08	1.78E-07	1.7845E-07
	0.20	3.48E-12	4.79E-10	3.27E-08	3.20E-07	1.13E-06	2.57E-06	2.5716E-06
	0.30	1.88E-11	2.25E-09	2.18E-07	1.33E-06	3.62E-06	7.49E-06	7.4929E-06
	0.40	5.64E-11	8.21E-09	6.37E-07	3.15E-06	7.73E-06	1.46E-05	1.4607E-05
	0.50	1.48E-10	1.96E-08	1.57E-06	7.16E-06	1.55E-05	2.67E-05	2.6714E-05
	Δ	1.4786E-10	1.9588E-08	1.5657E-06	7.1636E-06	1.5528E-05	2.6710E-05	Max-Min

Table I-4: Coefficient of Determination

R^2

		Non-dimensional Amplitude						
		0.05	0.10	0.20	0.30	0.40	0.50	Δ
Non Dim Frequency	0.05	1.0000	0.9999	0.9995	0.9983	0.9955	0.9910	8.9739E-03
	0.10	1.0000	0.9998	0.9973	0.9895	0.9792	0.9708	2.9196E-02
	0.20	1.0000	0.9994	0.9909	0.9753	0.9702	0.9713	2.9761E-02
	0.30	1.0000	0.9993	0.9855	0.9782	0.9798	0.9819	2.1772E-02
	0.40	1.0000	0.9991	0.9859	0.9832	0.9855	0.9877	1.6762E-02
	0.50	1.0000	0.9991	0.9861	0.9842	0.9875	0.9901	1.5785E-02
	Δ	6.0000E-06	8.4709E-04	1.3999E-02	2.2965E-02	2.5314E-02	2.0216E-02	Max-Min

Table I-5: Time Phase Shift

T_{TS}

		Non-dimensional Amplitude						
		0.05	0.10	0.20	0.30	0.40	0.50	Δ
Non Dim Frequency	0.05	0.1641	0.1671	0.1729	0.1796	0.1874	0.1957	3.1617E-02
	0.10	0.1140	0.1202	0.1384	0.1630	0.1864	0.2038	8.9881E-02
	0.20	0.0676	0.0806	0.1304	0.1776	0.2029	0.2168	1.4919E-01
	0.30	0.0467	0.0652	0.1372	0.1849	0.2060	0.2169	1.7022E-01
	0.40	0.0343	0.0561	0.1422	0.1850	0.2033	0.2134	1.7903E-01
	0.50	0.0261	0.0517	0.1439	0.1813	0.1983	0.2093	1.8324E-01
	Δ	1.3797E-01	1.1541E-01	4.2495E-02	2.1948E-02	1.9577E-02	2.1187E-02	Max-Min

2. Quadratic Coefficients

Table I-6: Nondimensional Added Mass

$Z'_{\dot{w}}$

		Non-dimensional Amplitude						
		0.05	0.10	0.20	0.30	0.40	0.50	Δ
Non Dim Frequency	0.05	-0.0075	-0.0074	-0.0073	-0.0071	-0.0069	-0.0066	9.3708E-04
	0.10	-0.0074	-0.0073	-0.0069	-0.0063	-0.0056	-0.0050	2.4252E-03
	0.20	-0.0073	-0.0069	-0.0058	-0.0047	-0.0040	-0.0035	3.8165E-03
	0.30	-0.0072	-0.0066	-0.0050	-0.0041	-0.0036	-0.0033	3.9020E-03
	0.40	-0.0072	-0.0064	-0.0047	-0.0040	-0.0037	-0.0035	3.6947E-03
	0.50	-0.0072	-0.0063	-0.0047	-0.0042	-0.0040	-0.0037	3.4743E-03
	Δ	3.5549E-04	1.1721E-03	2.5822E-03	3.0507E-03	3.2702E-03	3.2980E-03	Max-Min

Table I-7: Nondimensional Quadratic Damping

$Z'_{w|w|}$

		Non-dimensional Amplitude						
		0.05	0.10	0.20	0.30	0.40	0.50	Δ
Non Dim Frequency	0.05	-0.2852	-0.1467	-0.0783	-0.0569	-0.0475	-0.0429	2.4225E-01
	0.10	-0.1460	-0.0775	-0.0466	-0.0399	-0.0387	-0.0390	1.0730E-01
	0.20	-0.0745	-0.0437	-0.0353	-0.0367	-0.0377	-0.0380	3.9241E-02
	0.30	-0.0493	-0.0323	-0.0330	-0.0360	-0.0366	-0.0362	1.6968E-02
	0.40	-0.0356	-0.0262	-0.0329	-0.0355	-0.0352	-0.0343	9.4675E-03
	0.50	-0.0269	-0.0234	-0.0335	-0.0348	-0.0339	-0.0327	1.1401E-02
	Δ	2.5826E-01	1.2324E-01	4.5388E-02	2.2068E-02	1.3557E-02	1.0222E-02	Max-Min

Table I-8: Mean Square Error

MSE

		Non-dimensional Amplitude						
		0.05	0.10	0.20	0.30	0.40	0.50	Δ
Non Dim Frequency	0.05	7.55E-11	3.03E-10	1.18E-09	2.49E-09	3.99E-09	5.54E-09	5.4678E-09
	0.10	3.22E-10	1.30E-09	5.20E-09	1.44E-08	3.64E-08	7.47E-08	7.4336E-08
	0.20	1.34E-09	7.25E-09	7.81E-08	3.39E-07	7.51E-07	1.30E-06	1.2995E-06
	0.30	3.09E-09	2.58E-08	5.25E-07	1.78E-06	4.00E-06	7.72E-06	7.7184E-06
	0.40	5.34E-09	7.23E-08	1.77E-06	5.92E-06	1.41E-05	2.90E-05	2.9030E-05
	0.50	7.99E-09	1.75E-07	4.68E-06	1.62E-05	3.89E-05	7.78E-05	7.7829E-05
	Δ	7.9180E-09	1.7452E-07	4.6764E-06	1.6184E-05	3.8869E-05	7.7831E-05	Max-Min

Table I-9: Coefficient of Determination

R^2

		Non-dimensional Amplitude						
		0.05	0.10	0.20	0.30	0.40	0.50	Δ
Non Dim Frequency	0.05	0.9713	0.9720	0.9750	0.9793	0.9841	0.9884	1.7185E-02
	0.10	0.9829	0.9833	0.9854	0.9862	0.9864	0.9878	4.9100E-03
	0.20	0.9933	0.9908	0.9783	0.9738	0.9802	0.9855	1.9447E-02
	0.30	0.9966	0.9921	0.9651	0.9707	0.9777	0.9813	3.1409E-02
	0.40	0.9980	0.9921	0.9608	0.9685	0.9736	0.9756	3.7188E-02
	0.50	0.9988	0.9918	0.9585	0.9643	0.9686	0.9711	4.0293E-02
	Δ	2.7514E-02	2.0080E-02	2.6929E-02	2.1933E-02	1.7773E-02	1.7374E-02	Max-Min

Table I-10: Linear-Quadratic Relationship Factors

		Non-dimensional Amplitude						
		0.05	0.10	0.20	0.30	0.40	0.50	Δ
Non Dim Frequency	0.05	0.8834	0.8825	0.8799	0.8763	0.8719	0.8673	1.6151E-02
	0.10	0.8838	0.8817	0.8750	0.8680	0.8623	0.8579	2.5870E-02
	0.20	0.8837	0.8823	0.8765	0.8668	0.8612	0.8595	2.4162E-02
	0.30	0.8843	0.8865	0.8820	0.8700	0.8670	0.8663	2.0176E-02
	0.40	0.8851	0.8927	0.8848	0.8738	0.8718	0.8717	2.1001E-02
	0.50	0.8863	0.8989	0.8864	0.8768	0.8754	0.8750	2.3893E-02
	Δ	2.8700E-03	1.7247E-02	1.1333E-02	1.0009E-02	1.4193E-02	1.7155E-02	Max-Min

3. Combined Linear/Quadratic Coefficients

Table I-11: Nondimensional Added Mass

$Z'_{\dot{w}}$

		Non-dimensional Amplitude						
		0.05	0.10	0.20	0.30	0.40	0.50	Δ
Non Dim Frequency	0.05	-0.0075	-0.0074	-0.0073	-0.0071	-0.0069	-0.0066	9.3708E-04
	0.10	-0.0074	-0.0073	-0.0069	-0.0063	-0.0056	-0.0050	2.4252E-03
	0.20	-0.0073	-0.0069	-0.0058	-0.0047	-0.0040	-0.0035	3.8165E-03
	0.30	-0.0072	-0.0066	-0.0050	-0.0041	-0.0036	-0.0033	3.9020E-03
	0.40	-0.0072	-0.0064	-0.0047	-0.0040	-0.0037	-0.0035	3.6947E-03
	0.50	-0.0072	-0.0063	-0.0047	-0.0042	-0.0040	-0.0037	3.4743E-03
	Δ	3.5549E-04	1.1721E-03	2.5822E-03	3.0507E-03	3.2702E-03	3.2980E-03	Max-Min

Table I-12: Nondimensional Linear Damping

Z'_{w}

		Non-dimensional Amplitude						
		0.05	0.10	0.20	0.30	0.40	0.50	Δ
Non Dim Frequency	0.05	-0.0039	-0.0040	-0.0039	-0.0037	-0.0035	-0.0032	7.8461E-04
	0.10	-0.0041	-0.0041	-0.0039	-0.0037	-0.0033	-0.0028	1.2528E-03
	0.20	-0.0041	-0.0047	-0.0062	-0.0063	-0.0060	-0.0065	2.3369E-03
	0.30	-0.0042	-0.0058	-0.0105	-0.0110	-0.0128	-0.0152	1.0963E-02
	0.40	-0.0041	-0.0073	-0.0151	-0.0170	-0.0207	-0.0250	2.0914E-02
	0.50	-0.0040	-0.0094	-0.0201	-0.0234	-0.0288	-0.0343	3.0225E-02
	Δ	2.5097E-04	5.4285E-03	1.6191E-02	1.9723E-02	2.5436E-02	3.1436E-02	Max-Min

Table I-13: Nondimensional Quadratic Damping

$Z'_{w|w|}$

		Non-dimensional Amplitude						
		0.05	0.10	0.20	0.30	0.40	0.50	Δ
Non Dim Frequency	0.05	-0.0011	-0.0043	-0.0083	-0.0120	-0.0159	-0.0201	1.9024E-02
	0.10	0.0008	-0.0042	-0.0115	-0.0179	-0.0237	-0.0288	2.9589E-02
	0.20	0.0002	-0.0016	-0.0071	-0.0177	-0.0243	-0.0264	2.6538E-02
	0.30	0.0011	0.0027	-0.0015	-0.0141	-0.0174	-0.0180	2.0713E-02
	0.40	0.0016	0.0069	0.0011	-0.0100	-0.0119	-0.0117	1.8808E-02
	0.50	0.0021	0.0104	0.0027	-0.0067	-0.0080	-0.0080	1.8391E-02
	Δ	3.2211E-03	1.4702E-02	1.4148E-02	1.1128E-02	1.6318E-02	2.0781E-02	Max-Min

Table I-14: Mean Square Error

MSE

		Non-dimensional Amplitude						
		0.05	0.10	0.20	0.30	0.40	0.50	Δ
Non Dim Frequency	0.05	5.99E-14	5.51E-13	6.59E-12	4.12E-11	1.88E-10	6.80E-10	6.7976E-10
	0.10	3.15E-13	1.07E-11	4.64E-10	5.05E-09	2.26E-08	5.92E-08	5.9210E-08
	0.20	3.48E-12	4.70E-10	2.97E-08	2.27E-07	5.75E-07	9.75E-07	9.7466E-07
	0.30	1.74E-11	2.11E-09	2.17E-07	1.03E-06	2.17E-06	3.71E-06	3.7101E-06
	0.40	4.74E-11	5.43E-09	6.36E-07	2.68E-06	5.59E-06	9.56E-06	9.5635E-06
	0.50	1.08E-10	4.18E-09	1.55E-06	6.64E-06	1.32E-05	2.09E-05	2.0925E-05
	Δ	1.0749E-10	5.4331E-09	1.5490E-06	6.6350E-06	1.3182E-05	2.0925E-05	Max-Min

Table I-15: Coefficient of Determination

R^2

		Non-dimensional Amplitude						
		0.05	0.10	0.20	0.30	0.40	0.50	Δ
Non Dim Frequency	0.05	1.0000	0.9999	0.9999	0.9997	0.9993	0.9986	1.3945E-03
	0.10	1.0000	0.9999	0.9987	0.9952	0.9915	0.9903	9.6760E-03
	0.20	1.0000	0.9994	0.9918	0.9825	0.9849	0.9891	1.7508E-02
	0.30	1.0000	0.9994	0.9856	0.9831	0.9879	0.9910	1.6883E-02
	0.40	1.0000	0.9994	0.9860	0.9857	0.9895	0.9920	1.4250E-02
	0.50	1.0000	0.9998	0.9862	0.9854	0.9894	0.9922	1.4625E-02
	Δ	6.2876E-06	5.9575E-04	1.4286E-02	1.7183E-02	1.4385E-02	9.4618E-03	Max-Min